UNIVERSIDADE FEDERAL DE PERNAMBUCO
CENTRO DE CIÊNCIAS EXATAS E DA NATUREZA
PROGRAMA DE PÓS-GRADUAÇÃO EM FÍSICA

IGOR MACÊDO GONÇALVES

NONLINEAR PHOTONICS IN CdSe-BASED NANOPLATELETS AND RELATED COLLOIDAL NANOMATERIALS

Recife
2025

IGOR MACÊDO GONÇALVES

NONLINEAR PHOTONICS IN CdSe-BASED NANOPLATELETS AND RELATED COLLOIDAL NANOMATERIALS

Thesis submitted to the Graduate Program in Physics of the Federal University of Pernambuco as a partial requirement for obtaining the doctoral degree in Physics.

Concentration area: Optics.

Supervisor: Prof. Dr. Anderson Stevens Leônidas Gomes

Recife

2025

.Catalogação de Publicação na Fonte. UFPE - Biblioteca Central

Gonçalves, Igor Macêdo.
Nonlinear photonics in CdSe-based nanoplatelets and related colloidal nanomaterials / Igor Macedo Goncalves. - Recife, 2025.
183f.: il.

Tese (Doutorado) - Universidade Federal de Pernambuco, Centro de Ciências Exatas e da Natureza, Programa de Pós-Graduação em Física, 2025.
Orientação: Anderson Stevens Leônidas Gomes.
Inclui referências e apêndices.

1. CdSe nanoplatelets; 2. CdSe/CdS core/shell 2D nanostructures; 3. Halide perovskites; 4. Z-scan technique; 5. Optical Kerr Gate (OKG); 6. Nonlinear optical characterization. I. Gomes, Anderson Stevens Leonidas. II. Título.

UFPE-Biblioteca Central

IGOR MACÊDO GONÇALVES

NONLINEAR PHOTONICS IN CdSe-BASED NANOPLATELETS AND RELATED COLLOIDAL NANOMATERIALS

Thesis submitted to the Graduate Program in Physics of the Federal University of Pernambuco as a partial requirement for obtaining the doctoral degree in Physics.

Concentration area: Optics

Date of approval: 27/06/2025.

EXAMINATION COMMITTEE

_____

Prof. Dr. Anderson Stevens Leônidas Gomes
Orientador
Universidade Federal de Pernambuco

_____

Prof. Dr. Cid Bartolomeu de Araújo
Examinador Interno
Universidade Federal de Pernambuco

_____

Prof. Dr. Antonio Azevedo da Costa
Examinador Interno
Universidade Federal de Pernambuco

_____

Prof. Dr. Amitava Patra
Examinador Externo
Indian Association for the Cultivation of Science

_____

Prof. Dr. José Joatan Rodrigues Júnior
Examinador Externo
Universidade Federal de Sergipe

_____

Prof. Dr. Leonardo de Boni
Examinador Externo
Universidade de São Paulo

I dedicate this work to my beloved wife, Débora; my parents, Daniela and Ivonaldo; my brother, Ítalo; and my cherished grandmother, Maria de Lourdes.

ACKNOWLEDGMENTS

I am grateful to my beloved wife, Débora, for all the support throughout my academic career. She has always supported my decisions with love, respect, and patience. I would like to thank my parents, Ivonaldo and Daniela, who have always believed in me and supported my endeavors. I am also thankful to my brother, Ítalo, who is a scientist, and I like to think that I have inspired him in some way to pursue this career. Additionally, I want to acknowledge my dear friends, Allamys, Filipe, and Adanny – who are also scientists – for being there with me throughout this academic and life journey. I am also grateful to my extended family, including my uncles, aunts, cousins, and others, who have always believed in and supported me, especially my grandmother, Maria de Lourdes, who has always been by my side.

I would like to express my sincere gratitude to my supervisor, Prof. Anderson Gomes, for the opportunity to work under his guidance. His trust allowed me to collaborate with many inspiring colleagues and friends, with whom I shared not only scientific discussions but also conversations about life and future aspirations. I am especially grateful to Rosana, who kept the lab running smoothly; Cecília, a close collaborator and dear friend (and a passionate football fan – "Vamos Náutico!"); Jessica (or Jessi!), a supportive friend and project partner; Arthur, always encouraging; and Alyson, who worked closely with me and became a great friend. I also extend my thanks to Emanuel, Edwin, and many others I met along the way in the Physics Department at UFPE, Brazil.

I would also like to acknowledge Prof. Leonardo de Souza Menezes, who served as my co-supervisor during my time at the Nanoinstitut of Ludwig-Maximilians-Universität (LMU) in Munich, Germany, as part of my one-year CNPq sandwich doctorate program. In addition, I would like to acknowledge my esteemed friend Pablo Pincheira, who worked with me for three months at the Nanoinstitut of LMU. I would also like to acknowledge Professor A. Patra's group for providing the CdSe samples used in this study.

I would like to express my gratitude to the Coordination for the Improvement of Higher Education Personnel (CAPES), the National Council for Scientific and Technological Development (CNPq), and the Foundation for Science and Technology Support of Pernambuco (FACEPE). These Brazilian funding agencies have provided vital support for my academic career and have made this work possible.

Finally, I want to extend my thanks to everyone who has contributed, either directly or indirectly, to the development of this work.

“If I have seen further, it is by standing on the shoulders of giants.”

Sir Isaac Newton (Letter to Robert Hooke, 1676)

“Look deep into nature, and then you will understand everything better.”

Albert Einstein (source unknown).

RESUMO

As propriedades ópticas não lineares (NLO) de nanomateriais semicondutores têm despertado interesse crescente devido à sua relevância em fotônica ultrarrápida e aplicações optoeletrônicas. Nesta tese, investigamos as respostas NLO de terceira ordem e de ordens superiores de nanoplaquetas coloidais de seleneto de cádmio (CdSe) e de estruturas núcleo/casca CdSe/CdS em tolueno, utilizando as técnicas de varredura-Z com pulsos de femtossegundos e efeito Kerr ótico (OKG). Nossos resultados revelam uma forte concordância entre ambos os métodos e demonstram um comportamento complexo dependente da intensidade, incluindo inversão de sinal na refração não linear e evidências de absorção efetiva de três fótons. Medidas resolvidas no tempo mostram dinâmicas orientacionais ultrarrápidas, com respostas em escala sub-picosegundo moduladas pelo design das nanoestruturas. Sob excitação ressonante, foram observados efeitos de absorção saturável e autofocalização intensificada, especialmente nas nanoplaquetas de CdSe. As estruturas núcleo/casca de CdSe/CdS exibem características de absorção mais amplas e limiares de saturação mais elevados, indicativos de alargamento inhomogêneo. Comparativamente, pontos quânticos de perovskita haleto $CsPbBr_3$ mostram forte não linearidade do tipo Kerr em baixas intensidades, que satura sob excitação mais intensa devido ao preenchimento dos estados excitônicos e forte efeito não-linear do solvente. Esses achados destacam o papel crucial do confinamento quântico e da engenharia estrutural na otimização do comportamento óptico não linear, oferecendo subsídios para o desenvolvimento de materiais fotônicos avançados.

Palavras-chave: Nanoplaquetas de CdSe; nanoestruturas 2D núcleo/casca; perovskitas; técnica Z-scan; efeito Kerr ótico (OKG); caracterização óptica não linear.

ABSTRACT

The nonlinear optical (NLO) properties of semiconductor nanomaterials are of growing interest due to their relevance in ultrafast photonics and optoelectronic applications. In this work, we investigate the third-order and higher-order NLO responses of colloidal cadmium selenide (CdSe) nanoplatelets (NPLs) and core/shell CdSe/CdS structures in toluene using femtosecond Z-scan and optical Kerr gate (OKG) techniques. Our results reveal strong agreement between both methods and demonstrate complex intensity-dependent behavior, including sign reversal in nonlinear refraction and evidence of effective three-photon absorption. Time-resolved measurements show ultrafast orientational dynamics, with sub-picosecond responses modulated by nanostructure design. Under resonant excitation, both saturable absorption and enhanced self-focusing effects were observed, particularly in CdSe NPLs. The CdSe/CdS core/shell structures exhibit broader absorption features and higher saturation thresholds, indicative of inhomogeneous broadening. Comparatively, $CsPbBr_3$ halide perovskite quantum dots show strong Kerr-type nonlinearities at low intensities, which saturate under stronger excitation due to excitonic state filling and strong nonlinear solvent contribution. These findings highlight the crucial role of quantum confinement and structural engineering in optimizing nonlinear optical behavior, providing insights for the development of advanced photonic materials.

Keywords: CdSe nanoplatelets; CdSe/CdS core/shell 2D nanostructures; halide perovskites; Z-scan technique; Optical Kerr gate (OKG); nonlinear optical characterization.

FIGURES LIST

TABLE LIST

LIST OF ABBREVIATIONS AND ACRONYMS

2D – two-dimensional

2PA – two-photon absorption

3PA – three-photon absorption

BAM – Brewster's angle microscopy

$BaTiO_3$ – Barium titanate

CA Z-scan – Closed aperture Z-scan

CdS – Cadmium sulfide

CdSe – Cadmium selenide

CS – Core/shell

DFG – Difference frequency generation

DoS – Density of states

EM – Electromagnetic

EUV – Extreme ultraviolet

FHG – Fifth harmonic generation

FWM – Four wave mixing

GaAs – Gallium arsenide

GD – Gaussian decomposition

HH – Heavy hole

HHG – High harmonic generation

HRS – Hyper-Rayleigh scattering

IR – Infrared

KTP – Potassium titanyl phosphate

LEDs – Light emitting diodes

LH – Light hole

LiDAR – Light detection and ranging

$LiNbO_3$ – Lithium niobate

MEs – Maxwell's equations

Mid-IR – Mid-infrared

NLA – Nonlinear absorption

NLO – Nonlinear optical

NLR – Nonlinear refraction

NPLs – Nanoplatelets

OA Z-scan – Open aperture Z-scan

OKG – Optical Kerr gate

OR – Optical rectification

PAZ-scan – Photoacoustic Z-scan

PPLN – periodically loped lithium

PRZS – Polarized resolved Z-scan

PZT – Lead zirconate titanate

QDs – Quantum dots

SA – Saturable absorption

SFG – Sum frequency generation

SHG – second harmonic generation

SPM – Self-phase modulation

SSPM – Spatial self-phase modulation

STD – Standard deviation

SVEA –slowly varying envelope approximation

TEM – Transmission electron microscopy

THG – Third harmonic generation

TIR – Total internal reflection

TPA – two-photon absorption

TPEF – two-photon excited fluorescence

XPM – Cross-phase modulation

XRD – X-ray diffraction

β –BBO – Beta-barium borate

SUMMARY

1 INTRODUCTION

In recent years, the exploration of nonlinear optical (NLO) phenomena in semiconductor nanomaterials has garnered considerable attention due to their promising applications in ultrafast photonics, optical switching, telecommunications, and quantum information technologies. Among these materials, two-dimensional (2D) semiconductor nanoplatelets (NPLs), such as those based on cadmium selenide (CdSe), represent an exciting frontier due to their quantum confinement in the thickness direction, high oscillator strengths, and narrow emission spectra. These properties contribute to enhanced light-matter interactions, making them ideal candidates for studying third and higher-order nonlinear effects.

Layered CdSe NPLs are particularly appealing for NLO investigations owing to their discrete energy levels, strong excitonic transitions, and tunable nonlinear susceptibilities. Their well-defined geometry and monodispersity lead to reduced inhomogeneous broadening and consistent optical responses. Moreover, by engineering core/shell (CS) heterostructures, such as CdSe/CdS NPLs, one can manipulate the carrier dynamics and confine excitons more effectively, tailoring the balance between absorptive and refractive nonlinearities. The addition of a shell can enhance photostability, increase excitonic lifetime, and modify the relative contributions of electronic versus orientational nonlinear responses, offering additional control over the material's optical behavior.

Studying the NLO properties of these materials under both resonant and non-resonant excitation conditions is essential for understanding the underlying physical mechanisms. Techniques such as Z-scan and optical Kerr gate (OKG) allow for the precise characterization of third-order susceptibilities ($\chi^{(3)}$), nonlinear absorption (NLA), refractive nonlinearities and their time response (limited by the laser pulse duration). These measurements enable a comprehensive understanding of the interplay between real and virtual transitions, higher-order photon absorption processes, and carrier dynamics, which are crucial for developing nonlinear devices operating under femtosecond excitation regimes.

In parallel, halide perovskites – particularly quantum-confined structures like $CsPbBr_3$ quantum dots (QDs) – have emerged as strong contenders in the NLO field. Their high defect tolerance, strong excitonic effects, and broadband optical responses enable them to exhibit pronounced Kerr-type nonlinearities and saturable absorption, even under relatively low excitation intensities. The presence of discrete energy states and efficient light-matter coupling

make them highly suitable for applications in tunable photonics and all-optical signal processing.

In this work, we investigated the third and higher-order NLO properties of colloidal CdSe and CdSe/CdS CS NPLs in toluene using femtosecond Z-scan and OKG techniques. Our key findings include:

- Agreement between methods: Both Z-scan and OKG measurements showed excellent agreement in determining $\chi_R^{(3)}$ values, indicating no dependence on optical intensity depending on the regime and validating the robustness of our analysis.
- Sign reversal in NLO response: CdSe NPLs displayed a sign reversal in third-order nonlinear refraction (NLR) response upon solvent subtraction, while CdSe/CdS CS NPLs showed a negative response, suggesting the influence of a fifth-order process due to effective three-photon absorption (3PA), which involves an intermediate two-photon process followed by free carrier absorption.
- Time-resolved nonlinear dynamics: OKG results demonstrated ultrafast orientational nonlinearities, with response times of 0.7 ps and 1.0 ps for CdSe and CdSe/CdS CS NPLs, respectively. These were faster than those of pure solvents, highlighting the impact of nanostructure engineering on ultrafast NLO dynamics.
- Resonant excitation effects: Under resonant excitation at 505 nm and 665 nm, pronounced saturable absorption (SA) and positive nonlinear refraction (self-focusing) were observed. CdSe NPLs exhibited a two-order magnitude increase in NLR coefficients compared to the non-resonant case, underscoring the significant role of real-state excitations.
- Inhomogeneous broadening: CdSe/CdS CS NPLs demonstrated higher saturation thresholds and broader absorption features, consistent with an inhomogeneously broadened medium due to extended excitonic lifetimes.
- Halide perovskite comparison: $CsPbBr_3$ QDs dispersed in toluene exhibited strong Kerr-type nonlinearities at low excitation intensities, which saturated at higher intensities – likely due to excitonic state-filling effects and the increasing dominance of the solvent's nonlinear contribution. Under 800 nm excitation, the observed three-

photon absorption (3PA) was weaker than in pure toluene, consistent with the expected saturation behavior of the QDs' discrete energy states.

These results collectively emphasize the critical influence of nanostructure design, excitation regime, and quantum confinement on the NLO behavior of semiconductor materials. The comparative insights from CdSe-based NPLs and halide perovskite QDs offer valuable guidance for tailoring next-generation photonic and optoelectronic devices.

Research on the femtosecond third-order nonlinearities of two-dimensional layered transition metal dichalcogenides (2D-LTMDs) has been conducted; however, it falls outside the scope of this thesis, which focuses on nanostructured semiconductors. Nonetheless, we have dedicated a chapter to briefly discuss the findings from this research. The results from this study, along with the observations of nonlinearities in CdSe samples, have contributed to the publications listed in APPENDICES I to III. Additionally, research on perovskite nanostructures is currently in progress, with the aim of producing original publications.

Before presenting the results of this study, we begin by discussing the fundamental nonlinear optical techniques used to characterize the nonlinearities in all the materials investigated. The following chapter introduces the underlying concepts and mathematical foundations of two well-established methods: the **Z-scan** and the **Optical Kerr Gate (OKG)** techniques.

2 NONLINEAR OPTICS AND THIRD-ORDER TECHNIQUES

Nonlinear optics is the branch of optics that studies how intense electromagnetic fields interact with matter in a regime where the material response becomes nonlinear – that is, the induced polarization is no longer proportional to the applied electric field. This nonlinear interaction leads to a variety of phenomena that are absent in the linear regime and only become significant at high light intensities, such as those produced by pulsed or focused laser sources.

In linear optics, well-known effects such as absorption, refraction, and dispersion dominate. Absorption describes the attenuation of light as it propagates through a medium, while refraction refers to the bending of light due to spatial variations in the refractive index. Dispersion, in turn, accounts for the wavelength dependence of the refractive index, explaining phenomena like the separation of white light by a prism. Total internal reflection occurs when light is confined within a medium of higher refractive index and strikes a boundary at an angle greater than the critical angle, resulting in complete reflection. These effects, however, do not depend on the intensity of light. A detailed discussion of the linear regime of light-matter interaction is presented in APPENDIX A, section A.1.

When the intensity of the incident light is sufficiently high, the linear approximation breaks down, and nonlinear optical (NLO) effects emerge. Among the most important are second-order nonlinear effects, which arise from the second-order susceptibility tensor ($\chi^{(2)}$) of the material. These include second-harmonic generation (SHG), sum- and difference-frequency generation (SFG/DFG), optical rectification, and nonlinear scattering. Second-order processes are only allowed in non-centrosymmetric media and are extensively used in laser frequency conversion, generation of entangled photons, and electro-optic modulators. Due to their high efficiency and ultrafast response, second-order effects are foundational to modern photonics.

In materials that possess inversion symmetry, however, the second-order susceptibility vanishes, and third-order nonlinear effects – governed by the $\chi^{(3)}$ tensor – become dominant. These include third-harmonic generation (THG), self-focusing, self-phase modulation, two-photon absorption, nonlinear refraction, and the optical Kerr effect. Third-order processes are crucial for applications such as optical switching, all-optical signal processing, and ultrafast spectroscopy.

To experimentally probe third-order nonlinearities, techniques such as the **Z-scan** and the **Optical Kerr Gate (OKG)** are widely employed. The Z-scan technique provides detailed

information on both the sign and magnitude of nonlinear absorption and refractive index changes, while the OKG technique enables the observation of ultrafast birefringence dynamics induced by intense light pulses, essential for time-resolved optical gating and pulse characterization.

At even higher light intensities or in more exotic material systems, higher-order nonlinearities – such as those arising from $\chi^{(4)}$, $\chi^{(5)}$, and beyond – can become relevant. These contribute to phenomena like five-wave mixing, high-order harmonic generation, and extremely nonlinear propagation regimes, although they typically require very high field strengths or engineered materials like plasmonic nanostructures or metamaterials.

For a detailed discussion of second-, third-, and higher-order nonlinear effects – including their mathematical descriptions and selection rules – please refer to the APPENDIX A, section A.2 , at the end of this document.

The study of third-order NLO effects is fundamental for understanding light-matter interactions in various materials and has significant applications in photonics, optical signal processing, and ultrafast spectroscopy. Among the widely used experimental techniques to measure third-order nonlinearities, the Z-scan and OKG techniques stand out due to their sensitivity and versatility. The Z-scan technique, is a single-beam method that provides direct measurements of both the nonlinear refractive index (n_2) and nonlinear absorption coefficient (α_2) [1]. By translating a sample through the focal region of a Gaussian beam and recording the transmitted intensity, this method distinguishes between self-focusing and self-defocusing behaviors of materials, making it a crucial tool for characterizing nonlinear optical mediums [2]. On the other hand, the OKG technique exploits the ultrafast Kerr effect (see section A.2.3), where an intense pump beam induces birefringence in a medium, allowing a probe beam to be modulated based on the nonlinear response time. This method, widely used in ultrafast spectroscopy, enables the study of femtosecond nonlinear optical phenomena, particularly in transparent and semiconductor materials [3].

This chapter builds on the discussion of third-order NLO effects by introducing these two key experimental techniques: Z-Scan and OKG. Widely applied to semiconductors, polymers, and nanostructures [4], these methods are essential tools in photonics, ultrafast spectroscopy, and the development of NLO devices [5, 6], offering a comprehensive approach to characterizing third-order nonlinearities.

2.1 Z-scan Technique

The Z-scan technique is a highly sensitive and widely used experimental method for characterizing the NLO properties of materials, particularly their nonlinear refractive index and nonlinear absorption coefficients. Introduced by Sheik-Bahae et al. in 1990, this technique relies on translating a sample through the focal plane of a tightly focused Gaussian laser beam and monitoring changes in the beam's intensity profile [1]. By analyzing the transmittance of the sample as a function of its position (z) relative to the focal point, the Z-scan technique can simultaneously determine both the magnitude and sign of the material's NLO response. Its simplicity, versatility, and high sensitivity make it a crucial in the study of third-order NLO effects in a wide range of materials, including semiconductors [5], polymers [4], and nanomaterials [7]. Furthermore, the Z-scan technique has found extensive applications in photonics [6], ultrafast spectroscopy [8], and the development of nonlinear optical devices [9], making it an indispensable tool in modern optical research.

The next subsection will focus on the theoretical development of the Z-scan technique following the Sheik-Bahae fundamental approach. It will clearly outline the relationships between the transmission curves and the NLO refraction and absorption coefficients of the materials. These relationships are the primary objectives of the investigation using the Z-scan technique. Furthermore, a general standard Z-scan experimental setup configuration will also be presented.

2.1.1 The Standard Z-scan Technique

The mathematical theory of the Z-scan technique can be divided into two configurations: **closed-aperture (CA) Z-scan** and **open-aperture (OA) Z-scan**. The experimental setup consists of a Gaussian laser beam focused onto the sample, which is translated along the beam propagation axis (z-axis) using a motorized stage. A detector records the transmitted intensity, either with an aperture (CA) or without (OA), to isolate different nonlinear optical effects. Figure 2.1 shows the basic experimental apparatus to perform a Z-scan measurement in the CA configuration in which the ratio PD_1/PD_2 is recorded as a function of the sample position z.

In the CA Z-scan, where a finite aperture is placed in front of the detector (Figure 2.1), the experiment primarily probes nonlinear refraction (NLR**)**. As the sample moves through the focal region, a self-induced lensing effect modifies the beam divergence, leading to

characteristic peak-valley or valley-peak transmittance variations, depending on whether the material exhibits **self-focusing (positive n_2)** or **self-defocusing (negative n_2)** behavior [2]. In the other hand, in OA Z-scan, no aperture is used, and the transmission directly reflects nonlinear absorption (NLA) effects. For a material exhibiting **two-photon absorption** ($\alpha_2 > 0$), transmission decreases symmetrically around the focus due to increased absorption at higher intensities. Conversely, for **saturable absorption** ($\alpha_2 < 0$), transmission increases near focus as absorption saturates [10].

To compute the transmission expressions for both CA and OA Z-scan configurations, we systematically analyze the interaction of the Gaussian laser beam with the nonlinear material. In this discussion, we present a derivation of these expressions, closely following the methodology outlined in the foundational work by Sheik-Bahae et al. [1].

Figure 2.1 – Standard Z-scan experimental setup. Removing the aperture the system is an OA configuration and can be used to measure NLA. In this setup, PD_1 serves as the transmittance signal photodetector, while PD_2 acts as the reference photodetector to correct pulse-to-pulse fluctuations during the scan. The motorized stage that moves the sample through the focal plane is not shown in the picture.

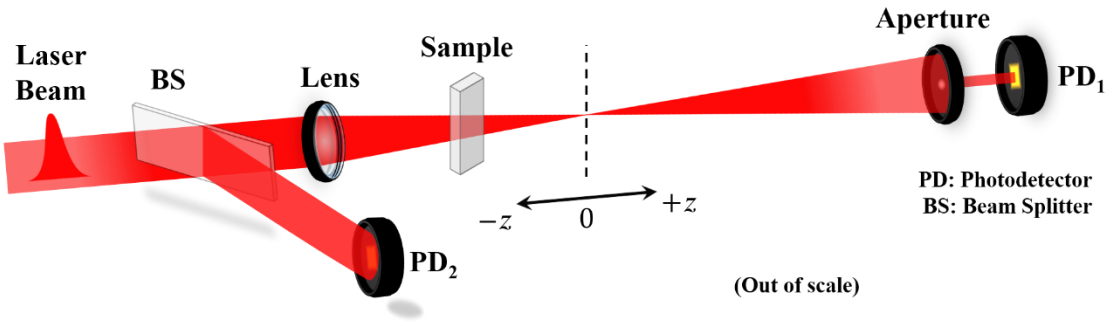

Source: The author (2025).

The Gaussian beam description is the starting point for analyzing the beam's interaction with the nonlinear material. The electric field of a Gaussian beam propagating along the z-axis is given by:

$$E(z,r,t) = E_0 \frac{w_0}{w(z)} \exp\left(-\frac{r^2}{w^2(z)}\right) \exp\left(-i\left(kz - \omega t + \frac{kr^2}{2R(z)}\right)\right) \quad , \tag{2.1}$$

where E_0 is the electrical field amplitude at the focus and contains the temporal envelope of the laser pulse, $w(z) = w_0\left(1 + (z/z_0)^2\right)^{1/2}$ is the beam radius at the position z, and $z_0 = \pi w_0^2/\lambda$ is the Rayleigh range – the distance over which the beam remains sufficiently focused. At $z = \pm z_0$ the beam intensity drops half of that at the focus [5]. $R(z) = z\left(1 + (z_0/z)^2\right)$ is the radius

of curvature of the wave front, $k = 2\pi/\lambda$ is the wave number, λ is the wavelength of the laser beam, and r is the radial distance from the beam axis [1, 5].

Considering a third-order nonlinear process the intensity-dependent refractive index $n(I)$ and absorption coefficient $\alpha(I)$ are given by the following expressions [5]:

$$n(I) = n_0 + n_2 I, \tag{2.2}$$

$$\alpha(I) = \alpha_0 + \alpha_2 I, \tag{2.3}$$

where, n_0 is the linear refractive index, n_2 is the third-order nonlinear refractive index, α_0 is the linear absorption coefficient, α_2 is the third-order nonlinear absorption coefficient, mostly related to 2PA process, and I is the laser beam intensity [5, 11]. These expressions describe the material's nonlinear response to the intense laser beam and are crucial to the Z-scan technique development. For a sample of thickness L and considered thin (that means, $L < z_0$), in the SEVA approximation (see section A.2.3) the wave equation evolution inside the material can be analyzed from a pair of phase and intensity equations as:

$$\frac{d\Delta\Phi}{dz'} = \Delta n(I)k, \tag{2.4}$$

$$\frac{dI}{dz'} = -\alpha(I)I, \tag{2.5}$$

where z' is the wave propagation depth in the sample, $\Delta n(I) = n_2 I$ (from equation (2.2)), and $\alpha(I)$ is given in equation (2.3). Note that z' should not be confused with the sample position z, and I is the on-axis intensity neglecting Fresnel reflections losses [1]. For a medium with weak NLA, equations (2.4) and (2.5) are solved to give the phase shift $\Delta\Phi$ at the exit surface of the sample, which simply follows the radial variation of the incident field at a given position of the sample z [1]:

$$\Delta\Phi(z, r) = \Delta\Phi_0(z)\exp\left(-\frac{r^2}{w^2(z)}\right). \tag{2.6}$$

Where $\Delta\Phi_0$ is the on-axis phase shift induced by the sample and is defined as:

$$\Delta\Phi_0(z) = \frac{2\pi}{\lambda} \cdot n_2 I(z) L_{eff}, \tag{2.7}$$

where $I(z) = I_0/\left(1 + (z/z_0)^2\right)$ is the intensity at the position z, I_0 is the peak intensity at focus ($z = 0$), $L_{eff} = \left(1 - \exp(-\alpha_0 L)\right)/\alpha_0$ is the effective sample length, and L is the physical length of the sample [2]. L_{eff} represents the optically active portion of the sample that effectively contributes to the NLO process. If $\alpha_0 L \ll 1$, then $L_{eff} \approx L$, meaning that the entire sample contributes for the NLO effect. The phase shift given in equation (2.6) arises due to the nonlinear intensity-dependent refractive index $n(I)$ [1].

The nonlinear phase shift $\Delta\Phi$ distorts the beam's wave front, leading to a change in the far-field intensity distribution. The distorted complex electric field at the exit plane of the sample now contains the nonlinear phase distortion [1, 2]:

$$E_{out}(z,r,t) = E(z,r,t)\exp\left(-\frac{\alpha_0 L}{2}\right)\exp(i\Delta\Phi(r,z)), \tag{2.8}$$

where $E(z,r,t)$ is the incident electric field given by equation (2.1). By means of the Huygen's principle one can obtain the far-field patter of the beam at the aperture plane through a zeroth-order Hankel transformation [12]. However, according to Sheik-Bahae et al. [1], a more convenient approach is applicable to Gaussian input beams, the so-called Gaussian decomposition (GD) method given by Weaire et al. [13]. Basically, the GD method decompose the complex electric field at the exit plane of the sample (equation (2.8)) into a summation of Gaussian beams through a Taylor series expansion of the nonlinear phase term $\exp(i\Delta\Phi(r,z))$. The GD method is useful because for the small phase changes detected by the Z-scan approach only a few terms in the Taylor expansion are relevant [1]. Furthermore, the GD method can be easily extended to higher order nonlinearities terms. For further details on the GD method procedure, please refer to reference [13].

Thus, according to Sheik-Bahae et al. [1], the normalized transmittance through the aperture for each sample position z is given by the following equation:

$$T(z) = \left(\int_{-\infty}^{+\infty} P_T\left(\Delta\Phi_0(t)\right)dt\right) \Bigg/ \left(S\int_{-\infty}^{+\infty} P_i(t)dt\right). \tag{2.9}$$

$P_T(\Delta\Phi_0(t))$ is the transmitted power through the aperture and is obtained by spatially integrating the far-field electric field at the aperture plane, $E_a(r,t)$, up to the aperture radius r_a. $E_a(r,t)$ depends on the output field in the exit plane of the sample propagated in the free space through a distance d, the distance from the sample to the aperture plane. For an explicit expression of $E_a(r,t)$ and extra details, the reader can consult references [1] and [2]. Furthermore, in equation (2.9), $S = 1 - \exp\left(-2r_a^2/w_a^2\right)$ is the aperture linear transmittance, and w_a denotes the beam radius at the aperture plane in the linear regime (without nonlinear sample) [1]. $P_i(t) = \pi w_0^2 I_0(t)/2$ is the instantaneous input power within the sample [1].

If $d \gg z_0$ (the far-field condition), and a small aperture is applied ($S \approx 0$) together with the small nonlinear phase change limit, that is,$|\Delta\Phi_0| \ll 1$, one can deduce an analytical expression for the transmittance given in equation (2.9). This is possible because at these conditions only two terms in the Taylor expansion of the nonlinear phase term $\exp(i\Delta\Phi(r,z))$

are remaining to compute $E_a(r,t)$ at the aperture plane. Thus, the normalized transmittance for a third-order nonlinearity in the CA Z-scan configuration can be written as [1, 2]:

$$T(z) \cong 1 + \frac{4\Delta\phi_0(z/z_0)}{\left(1+(z/z_0)^2\right)\left(9+(z/z_0)^2\right)}, \tag{2.10}$$

$\Delta\phi_0 = kn_2 I_0 L_{eff}$ is the on-axis phase shift at the focal region. Figure 2.2 (a) shows the CA theoretical curves for $\Delta\phi_0 = \pm 0.25$. As expected, for a self-focusing effect ($n_2 > 0$) a valley-peak pattern is achieved and for a self-defocusing effect ($n_2 < 0$) a peak-valley pattern is observed. For a given $\Delta\phi_0$ the magnitude and shape of $T(z)$ remains independent on wavelength or geometry, since the far-field condition for the aperture plane ($d \gg z_0$) is satisfied.

Figure 2.2 – Z-scan theoretical curves for a third-order nonlinearity. (a) CA Z-scan and (b) OA Z-scan. The horizontal dotted lines are baselines accounting for the linear regime. The parameters used were: $\lambda = 532$ nm, $w_0 = 20$ µm, $z_0 = 2.35$ µm, $L = 1.0$ mm, $\alpha_0 = 1.0$ m^{-1}, $L_{eff} \approx L$, and $I_0 = 100$ GW/m^2.

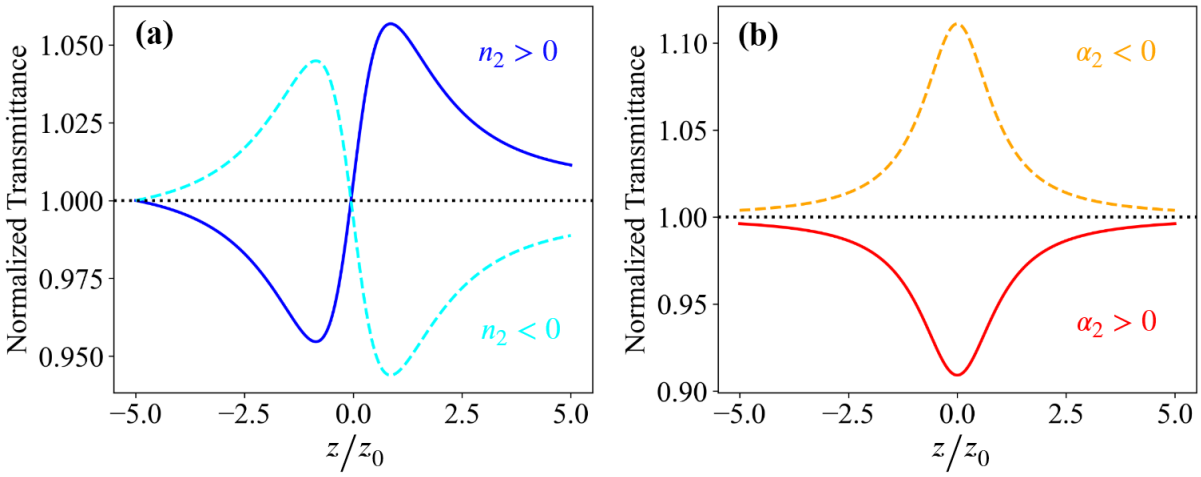

Source: The author (2025).

The aperture size S is a crucial parameter, as a larger aperture minimizes variation in $T(z)$, particularly at the peak where beam narrowing occurs, leading to a peak transmittance that cannot exceed $1 - S$ [1]. Then, for very large apertures or no aperture ($S = 1$), the effect vanishes and $T(z) = 1$ for all z and $\Delta\phi_0$. For small phase changes, the peak and valley occur at the same distances from the focus. For third-order nonlinearity, this distance is calculated as [1]:

$$\Delta z_{p-v} \cong 0.86 z_0, \tag{2.11}$$

where z_0 is the Rayleigh range distance. For larger phase distortions ($\Delta\phi_0 > 1$), the peak-valley symmetry no longer applies and both, peak and valley move toward $\pm z$ according to the sign

of the nonlinearity ($\pm\Delta\phi_0$). Their separation remains nearly constant, defined by the relation [1]:

$$\Delta z_{p-v} \cong 1.7 z_0. \tag{2.12}$$

Using equations (2.11) and (2.12), a CA Z-scan allows for the experimental measurement of the Rayleigh range of the system, enabling the estimation of the beam diameter at the focal point. Furthermore, it is possible to define an easily measurable quantity,ΔT_{p-v}, as the difference between the normalized peak transmittance (T_p) and valley transmittance (T_v): $\Delta T_{p-v} = T_p - T_v$. These curves exhibit several useful features. First, for a given order of nonlinearity, they can be considered universal. In other words, they are independent of the laser wavelength, geometry (as long as the far-field condition is met), and the sign of nonlinearity. Second, for all aperture sizes, the variation of ΔT_{p-v} is found to be almost linearly dependent on $|\Delta\phi_0|$. For cases of small phase distortion and small aperture ($S \approx 0$), we have [1, 2]:

$$\Delta T_{p-v} = 0.406|\Delta\phi_0|. \tag{2.13}$$

Numerical calculations show that this relation is accurate to within 0.5% for $|\Delta\phi_0| \leq \pi$ [85]. This condition ensures that the induced nonlinear phase shift remains within a single optical cycle, thus preventing complex self-interference effects that could lead to distortions in the Z-scan profile and complicate the extraction of the nonlinear refractive index n_2 [2].

The relationship between ΔT_{p-v} and $\Delta\phi_0$, as described in equation (2.13), is highly sensitive to changes in the aperture size S. Through numerical fitting, Sheik-Bahae et al. [1] derived a more precise relationship that takes into account the variations in S as follows:

$$\Delta T_{p-v} \cong 0.406(1-S)^{0.25}|\Delta\phi_0|. \tag{2.14}$$

This relation is valid for $|\Delta\phi_0| \leq \pi$ within an accuracy of $\pm 2\%$. The implications of equations (2.13) and (2.14) are quite promising, as they can be used to accurately estimate the nonlinear refractive index (n_2) after performing a Z-scan. What is particularly intriguing about these expressions is that they highlight the highly sensitive nature of the Z-scan technique. For instance, if our experimental apparatus and data acquisition systems can detect transmittance changes of ΔT_{p-v} of $\approx 1\%$, we will be able to measure phase changes corresponding to less than $\lambda/250$ in wave front distortion [1]. However, achieving such sensitivity requires relatively high optical quality of the sample being studied [2].

Equations (2.13) and (2.14) were derived based on a cubic nonlinearity, specifically a $\chi^{(3)}$ effect. A similar approach can be used to analyze higher-order nonlinearities, such as a fifth-order response (a $\chi^{(5)}$ effect). Regardless of the order of nonlinearity, the Z-scan analysis

is expected to show the same qualitative characteristics. In the following paragraphs, we will continue to utilize the Sheik-Bahae approach to derive information about nonlinear absorption from the OA Z-scan curve. We will also present an analytical expression for the transmittance resulting from an absorptive third-order nonlinearity, particularly for 2PA process.

Some materials exhibit both NLR and NLA effects simultaneously. Large refractive nonlinearities in materials are often associated with resonant transitions, which can occur through either single-photon or multiphoton processes. The NLA in these materials – whether caused by direct multiphoton absorption, saturation of single-photon absorption, or dynamic free-carrier absorption – significantly affects measurements of NLR when using the Z-scan technique [1]. In the presence of NLA, a Z-scan conducted with a fully open aperture ($S = 1$) remains insensitive to NLR under the thin-sample approximation. Z-scan traces obtained without an aperture are expected to be symmetric around the focal point ($z = 0$). In these traces, a minimum transmittance is observed in the case of multiphoton absorption, while a maximum transmittance occurs due to absorption saturation [2]. It is important to note that the nonlinear absorption coefficients can be directly extracted from these transmittance curves. For reference, see Figure 2.2 (b).

To compute the NLA caused by a 2PA process, we have to reexamine equations (2.4) and (2.5) considering the intensity-dependent NLA coefficient given by equation (2.3). For a low excitation regime, where it is possible to ignore free-carrier effects [2], the intensity distribution and phase shift of the beam at the exit surface of the nonlinear sample can be given by the following expressions [1]:

$$I_e(z, r, t) = \frac{I(z, r, t)e^{-\alpha_0 L}}{1 + q(z, r, t)} \tag{2.15}$$

and,

$$\Delta\Phi(z, r, t) = k\left(\frac{n_2}{\alpha_2}\right)\ln[1 + q(z, r, t)], \tag{2.16}$$

where, $q(z, r, t) = \alpha_2 I(z, r, t)L_{eff}$, $k = 2\pi/\lambda$ is the wave number of the incident laser beam, and z is the sample position as usual. Thus, equations (2.15) and (2.16) are combined to compute the complex electric field at the exit surface of the samples as [14]:

$$E_e(z, r, t) = E(z, r, t)e^{-\alpha_0 L/2}(1 + q)^{(ik(n_2/\alpha_2)-1/2)}. \tag{2.17}$$

Equation (2.17) simplifies to equation (2.8) when 2PA is negligible. Generally, applying a zeroth-order Hankel transform to equation (2.17) yields the field distribution at the aperture [12]. This distribution can then be used in equation (2.9) to calculate the transmittance.

However, for $|q| < 1$, by employing a binomial series expansion in powers of q, equation (2.17) can be expressed as an infinite sum of Gaussian beams, similar to the scenario described for purely refractive conditions [1]. For more details on the mathematical procedures, the reader can refer to references [1] and [2].

The variations in the Z-scan transmittance can be calculated using the same procedure described earlier. As indicated in equations (2.16) and (2.17), the contributions from absorption and refraction to the far-field beam profile and Z-scan transmittance are interconnected. However, when the aperture is removed, the Z-scan transmittance becomes independent of beam distortion and relies solely on the nonlinear absorption effect. In this scenario, with $S = 1$, the total transmitted fluency can be determined by spatially integrating equation (2.15) without needing to include the free-space propagation process. By integrating equation (2.15) at the variable z over the radial variable r, we can derive the transmitted power $P(z,t)$ as follows:

$$P(z,t) = P_i(t)e^{-\alpha_0 L}\frac{\ln\left[1+q_0(z,t)\right]}{q_0(z,t)}, \tag{2.18}$$

where $P_i(t)$ is the instantaneous power as defined in (2.9), $q_0(z,t) = q_0(t)/\left(1+(z/z_0)^2\right)$, and $q_0(t) \equiv \alpha_2 I_0(t) L_{eff}$ [1]. For temporally Gaussian pulse, equation (2.18) can be time integrated and it is possible to compute the normalized energy transmittance [1, 2]:

$$T(z, S=1) = \frac{1}{(\pi)^{1/2} q_0(z)} \int_{-\infty}^{+\infty} \ln\ 1 + q_0(z)e^{-\tau^2}\ d\tau\,, \tag{2.19}$$

where, $q_0(z) = q_0/\left(1+(z/z_0)^2\right)$, with $q_0 \equiv \alpha_2 I_0 L_{eff}$ and I_0 is the excitation peak intensity at the lens focal region. For weak NLA, that means, $|q_0| < 1$, this transmittance can be expressed in terms of the peak intensity I_0 in a summation form more suitable numerical and analytical evaluation as [1]:

$$T(z, S=1) = \sum_{m=0}^{\infty} \frac{\left[-q_0(z)\right]^m}{(m+1)^{3/2}}, \quad \text{for} \quad |q_0| < 1. \tag{2.20}$$

For a weak 2PA effect only the first two terms of the sum are significant, then it is possible to explicit express the normalized transmittance as follows:

$$T(z) \cong 1 - \frac{q_0}{2^{3/2}(1+(z/z_0)^2)}. \tag{2.21}$$

$q_0 = \alpha_2 I_0 L_{eff}$ is an important parameter and by fitting the OA Z-scan data using equation (2.21) is possible to compute the NLA coefficient α_2 of a material. Figure 2.2 (b), shows the

theoretical OA Z-scan curves for $q_0 = \pm 0.30$. The red continuum curve represents a 2PA process, indicating that $\alpha_2 > 0$, while the yellow dashed curve indicates a saturation effect, where $\alpha_2 < 0$. Additionally, when an OA Z-scan is performed ($S = 1$), the NLA coefficient α_2 can be determined unambiguously. Once α_2 is known, the CA Z-scan configuration ($S < 1$) can be utilized to extract the remaining unknown NLR coefficient, namely n_2.

Figure 2.2 (a) and (b) illustrate the theoretical Z-scan curves for the CA and OA configurations, displaying the pure NLR and NLA effects. This approach highlights the fundamental aspects of both effects, demonstrating that it is possible to separately characterize the third-order NLO refractive and absorptive coefficients in such scenarios. However, for materials that exhibit both NLR and relevant 2PA, the CA Z-scan transmittance is influenced by both phase distortion and intensity-dependent absorption, making it difficult to isolate the refractive contribution. In this case, the CA Z-scan transmittance curve ($S < 1$) will display an asymmetry around the peak-valley or valley-peak pattern due to the contribution from NLA. To accurately extract the nonlinear refractive index (n_2) while mitigating the influence of NLA, an effective strategy is to normalize the CA Z-scan data with the OA Z-scan data. Figure 2.3 presents the theoretical Z-scan curves for a self-focusing and two-photon absorber material.

Figure 2.3 – Theoretical Z-scan curves. The T_{CA}/T_{OA} transmittance curve is the CA Z-scan (T_{CA}) normalized with the OA Z-scan (T_{OA}). This curve was building considering equations (2.10) and (2.21). The horizontal dotted line is a baseline accounting for the linear regime, while the gray vertical line emphasize the focal point for symmetry considerations. The parameters are the same as for Figure 2.2.

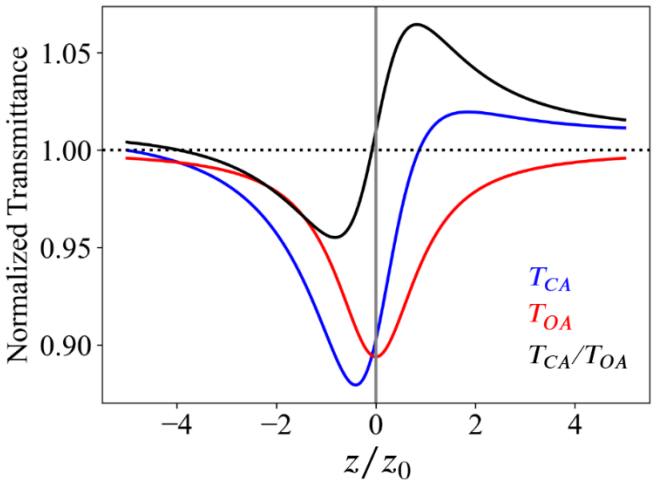

Source: The author (2025).

By dividing the CA transmittance by the OA transmittance, one effectively removes the absorption-induced variations, allowing the pure refractive nonlinear phase shift to be analyzed

[1], as one can see in the black curve in Figure 2.3. This approach is particularly important in semiconductors, where free-carrier effects or excited-state absorption can further complicate the interpretation of CA Z-scan results [15]. The normalization method has become a standard in nonlinear optical characterization and is widely used for determining third-order nonlinear susceptibilities and higher-order effects in various materials [16].

While the standard Z-scan technique is widely used to characterize third-order nonlinearities, it is important to consider the influence of thermal effects under certain excitation conditions. In Z-scan experiments, thermal effects can significantly distort the measured nonlinear optical response, especially in materials with notable linear absorption. High-intensity laser irradiation can cause localized heating, leading to thermal lensing and refractive index changes that introduce additional phase distortions. These effects are particularly pronounced under continuous-wave (CW), quasi-CW (high repetition rate), and long-pulse excitation, where insufficient time for thermal relaxation between pulses results in heat accumulation. Since thermal effects can mimic or mask intrinsic electronic nonlinearities, distinguishing between them is crucial for accurate material characterization. APPENDIX B provides a detailed discussion of the origins of thermal effects in Z-scan measurements and strategies to minimize their influence.

Building on the standard and thermally influenced Z-scan approaches, several alternative techniques have been developed to extend the method's capabilities and adapt it to specific experimental needs. Variants such as eclipse Z-scan**,** time-resolved Z-scan**,** polarization-resolved Z-scan, and photoacoustic Z-scan offer enhanced sensitivity, temporal resolution, or the ability to isolate specific nonlinear contributions. These methods enable the investigation of fast dynamics, anisotropic responses, and nonlinear absorption in samples where conventional Z-scan techniques may face limitations. A detailed overview of these advanced Z-scan variants and their applications is provided in APPENDIX C.

In this section, we presented the theoretical fundamentals of the Z-scan technique, as developed by Sheik-Bahae et al. [1]. The Z-scan method is a fundamental tool for characterizing optical nonlinearities with high sensitivity and simplicity. This method has been widely applied in diverse fields, including the characterization of ultrafast optical materials for all-optical switching [17], the study of two-photon absorption in semiconductors [15], and the development of optical limiters for laser protection [18]. Additionally, it has been employed in biological imaging to assess nonlinear properties of biomolecules and nanostructures [19]. The

robustness and versatility of the Z-scan technique continue to make it a standard in nonlinear optics, contributing to the advancement of photonic technologies. For a deeper understanding and more details on the theoretical framework presented, readers can consult the review by E. V. Stryland and M. Sheik-Bahae [16], which discusses the Z-scan method and other techniques used to measure the nonlinear optical properties of materials.

The next section focuses on another powerful technique for probing third-order nonlinearities: the **Optical Kerr Gate (OKG)**. Unlike standard Z-scan, which provides spatially resolved measurements of nonlinear refraction and absorption, OKG offers ultrafast temporal resolution, making it especially suited for investigating the dynamics of the optical Kerr effect and fast nonlinear responses. The upcoming section will detail the principles, experimental setup, and applications of the OKG technique in characterizing third-order nonlinear optical materials.

2.2 Pump and Probe Techniques

Pump-probe techniques are fundamental tools for characterizing the NLO properties of materials by measuring the changes induced in a sample by an intense pump pulse, which are subsequently probed by a weaker pulse. Pump-probe techniques are essential for studying ultrafast NLO properties, particularly when time-resolved measurements are required. They can be used to investigate carrier dynamics in semiconductors [20], NLA mechanisms like two-photon and excited-state absorption [5, 20], and intensity-dependent refractive index changes [5]. Moreover, they can help to analyze coherent phenomena such as wave mixing and photon echoes [21], characterize materials for ultrafast optical switching [22], and explore strong field interactions like multiphoton ionization [23]. These techniques provide high temporal resolution, making them indispensable for understanding transient optical processes beyond steady-state methods like the standard Z-scan.

Among the widely used pump-probe methods, degenerate and non-degenerate pump-probe spectroscopy provide insights into ultrafast carrier dynamics, excited-state absorption, and refractive index changes, depending on the temporal resolution and spectral properties of the pulses used [5]. In transient absorption spectroscopy, variations in probe transmission as a function of pump-probe delay time reveal nonlinear absorption mechanisms, such as two-photon absorption and excited-state absorption [5, 20]. Similarly, time-resolved reflectivity techniques monitor dynamic changes in the refractive index and reflectivity, offering insights into NLR effects [20]. Furthermore, frequency-domain pump-probe methods, such as four-wave mixing, enable the study of coherent nonlinear interactions, including optical Kerr effects and third-order susceptibilities [21]. These techniques complement time-resolved Z-scan methods, previously introduced, by providing a broader understanding of nonlinear responses in different temporal and spectral regimes.

Particularly, the **Optical Kerr Gate (OKG)** or Optical Shutter technique is based on the intensity-dependent refractive index change induced by a strong pump beam in a nonlinear medium, which modulates the transmission of a weaker probe beam. When the pump beam is present, it induces birefringence in the material through the optical Kerr effect, allowing the probe beam – polarized at 45° relative to the pump – to pass through a crossed polarizer. In the absence of the pump, the probe remains blocked, effectively acting as an ultrafast optical shutter [5]. This technique is particularly useful for ultrafast time-resolved spectroscopy, as it provides a high temporal resolution limited only by the response time of the Kerr medium, typically in

the femtosecond range [24]. It is widely applied in fluorescence up-conversion measurements and time-gated imaging, enabling the study of fast relaxation dynamics in complex molecular and semiconductor systems [25].

In the next subsection, we develop the theoretical framework of the OKG technique and highlight its advantages for resolving ultrafast time dynamics in third-order nonlinear materials.

2.2.1 Optical Kerr Gate Technique

The OKG technique is a powerful ultrafast optical switching mechanism based on the third-order NLO effect known as the Kerr effect (see equation (A.69)). This phenomenon allows for the temporal gating of light transmission through a nonlinear medium by inducing birefringence that is proportional to the intensity of an applied optical pump pulse. OKG is commonly used in ultrafast spectroscopy, optical signal processing, and time-resolved imaging [26, 27].

The induced birefringence in the medium modifies the polarization state of a probe pulse. If an analyzer is placed orthogonal to the initial polarization, transmission occurs only when the pump pulse induces sufficient birefringence. The intensity of the OKG transmitted probe signal is expressed as [28]:

$$I_{OKG} = I_{probe}\sin^2(2\theta)\sin^2(\Delta\phi/2), \tag{2.22}$$

where, I_{probe} is the initial probe beam intensity, θ is the intersecting angle between polarization of the probe and pump beams, and $\Delta\phi = kL_{eff}n_2I_{pump}$ is the phase shift caused by the birefringence from the third-order self-induced nonlinearity [28]. $k = 2\pi/\lambda$, where λ is the probe beam's wavelength, L_{eff} is the sample's effective length, and n_2 is the NLR coefficient.

Positioning the pump and probe beams at a 45° angle optimizes Kerr-induced birefringence modulation, which enhances signal contrast and improves gating efficiency in the OKG process [5]. Therefore, for small phase changes ($\Delta\phi \ll 1$), the I_{OKG} signal described in equation (2.22)) can be reformulated as follows:

$$I_{OKG} \approx I_{probe}\left(\frac{kL_{eff}n_2I_{pump}}{2}\right)^2. \tag{2.23}$$

The I_{OKG} signal described by equation (2.23) is sensitive to variations in the intensity of the probe beam. This sensitivity indicates that the signal can detect the magnitude of the nonlinear response ($|n_2|$), however it does not provide information about its phase, consequently, the signal of the nonlinearity. This behavior is characteristic of a homodyne detection system,

which is commonly employed to analyze the temporal dynamics of the Kerr effect in materials. This method allows for the direct extraction of relaxation times from the decay profile of the OKG signal [5]. Figure 2.4 illustrates a simplified scheme of an OKG setup, along with examples of decay profiles for various nonlinear materials.

Figure 2.4 illustrates the fundamental concept of an OKG setup, where both the pump and probe beams are linearly polarized, with their polarizations rotated 45° with respect to each other. PBS_2 functions as an analyzer positioned just before the photodetector, and it is set to transmit light that has crossed polarization (90°) relative to the probe beam. In some OKG systems, even without the presence of the pump beam, a portion of the probe can leak through the analyzer due to linear birefringence or the limited extinction ratio of the PBS. The quarter-wave plate ($\lambda/4$) depicted in Figure 2.4 can help adjust this leakage prior to reaching the analyzer.

Figure 2.4 – Scheme of an optical Kerr gate (OKG) setup. Inset: OKG signals for acetonitrile (ACN), carbon disulfide (CS_2), and niobium disulfide (NbS_2) two-dimensional (2D) nanoflakes suspended in ACN [29]. Respectively, black crosses, green open circles, and red stars.

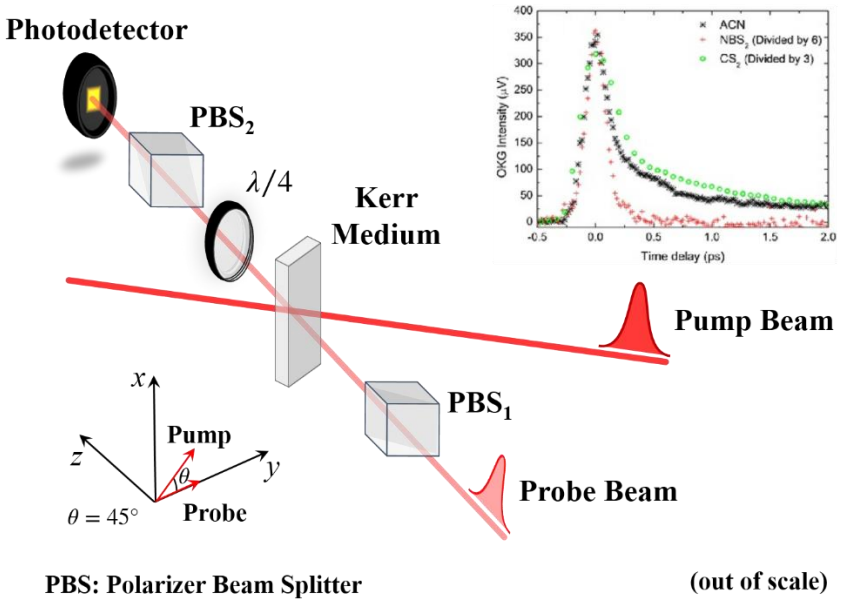

Source: The author (2025).

The insert in Figure 2.4 shows the OKG responses of three different nonlinear materials: ACN, SC_2, and 2D NbS_2 nanoflakes suspended in ACN. The OGK signals from ACN and CS_2 display a rapid decay followed by a slower tail response, as illustrated by the black and green curves in Figure 2.4. This behavior is typical in some solvents and is attributed to an orientational nonlinear response resulting from the inertia of the solvent molecules [29]. In

contrast, NbS_2 exhibits only a third-order ultrafast electronic response, which is limited by the laser pulse duration, measured at approximately 180 femtoseconds in this study [29].

In summary, the OKG technique is a powerful tool for ultrafast optical switching and time-resolved spectroscopy, by utilizing the intensity-dependent refractive index change in nonlinear media. Its ability to achieve high temporal resolution and selective gating makes it particularly useful in diverse applications and nonlinear optical studies. Despite challenges related to phase distortions and material limitations, ongoing advancements in Kerr media and optical configurations continue to enhance the technique's efficiency and applicability. As research progresses, the OKG remains a valuable method for probing ultrafast dynamics in various scientific and technological domains.

This subsection concludes Chapter 2, which examined the fundamentals and practical applications of the Z-scan and OKG techniques. Key references were also provided for readers interested in exploring these nonlinear optical methods in greater depth

In the next chapter, we will begin discussing the initial results of this thesis, specifically the nonlinear optical properties of two-dimensional cadmium selenide (CdSe) nanoplatelets (NPLs) suspended in solution, which show promise for all-optical and photonic applications.

3 NONLINEAR OPTICAL PROPERTIES OF CdSe NANOPLATELETS

Cadmium selenide (CdSe) nanoplatelets (NPLs) have attracted significant attention in recent years due to their exceptional optical properties, which stem from their unique quantum confinement effects and atomically controlled thickness. These two-dimensional (2D) semiconductor nanostructures exhibit sharp excitonic transitions, high photoluminescence quantum yields, and tunable bandgaps, making them ideal candidates for optoelectronic and photonic applications [30]. Among the various configurations, monolayer and core-shell CdSe NPLs offer distinct advantages in tailoring the optical response, particularly in the context of nonlinear optical (NLO) properties, which are critical for applications in optical switching, frequency conversion, and ultrafast photonics [31].

Their strong excitonic effects and enhanced light-matter interactions primarily govern the NLO properties of CdSe NPLs. These materials exhibit significant third-order nonlinearities, including two-photon absorption (TPA) and nonlinear refractive index modulation, which are essential for their application in laser technology and optical modulation devices [32]. The presence of a core-shell architecture, where a shell material such as CdS or ZnS encapsulates a CdSe core, further enhances the NLO response by reducing non-radiative recombination and improving charge carrier dynamics [33]. This structural modification not only extends their stability but also enhances their nonlinear absorption and refraction characteristics, thereby making them more suitable for high-power optical applications.

Given their superior NLO responses, CdSe NPLs in monolayer and core-shell configurations are increasingly being explored for their potential in photonic and optoelectronic technologies. Their ability to manipulate light at the nanoscale opens avenues for applications in ultrafast photonics, all-optical signal processing, and advanced photodetectors [30]. This discussion delves into the underlying mechanisms of the NLO properties of CdSe NPLs, the impact of structural modifications, and their potential integration into next-generation optical devices.

In this chapter, we begin by discussing the fundamental NLO phenomena in nanostructured semiconductors to provide the reader with a foundational understanding of these effects. Next, we will explore the optical characteristics of all-inorganic CdSe NPLs, highlighting their potential as promising materials for nanophotonics. Our focus will then shift to layered CdSe NPLs and core-shell structures, particularly CdSe/CdS core-shell NPLs, where we will examine their specific characteristics and efficient synthesis protocols. We will also

investigate the NLO properties of these nanostructures, focusing specifically on the third-order response. This will be done through sub-bandgap excitonic measurements using the Z-scan technique, as well as time-resolved results obtained through the OKG method. Finally, we will present results and discussions regarding measurements conducted in the resonant excitonic femtosecond regime.

3.1 Nonlinear Optics in Nanostructured Semiconductors

Nonlinear optical (NLO) properties of semiconductors have garnered significant interest due to their fundamental role in modern photonics and optoelectronic applications. Unlike linear optical phenomena, NLO effects arise from the intensity-dependent response of a material to an incident electromagnetic field, leading to processes such as second- and third-harmonic generation, two-photon absorption (TPA), and self-phase modulation [5]. These effects are particularly pronounced in semiconductor nanostructures, where quantum confinement enhances excitonic interactions and increases the nonlinear susceptibility [34, 35]. Materials such as cadmium selenide (CdSe), gallium arsenide (GaAs), and silicon exhibit strong third-order nonlinearities, making them suitable for applications in optical switching, ultrafast signal processing, and high-resolution imaging [5, 22]. The design of semiconductor heterostructures, including core-shell nanoparticles, quantum wells, and 2D nanomaterials, further allows for tailoring of nonlinear optical responses to meet specific technological demands [36]. Understanding the mechanisms underlying these NLO effects is crucial for optimizing semiconductor-based devices for the next-generation photonic technologies.

NLO phenomena in semiconductors arise due to the anharmonic responses of electrons to intense optical fields, leading to effects such as third-order nonlinearities ($\chi^{(3)}$) and nonlinear cascade process [37]. The quantum confinement of excitons (electron-hole pairs) in semiconductor nanostructures (e.g., quantum dots, nanowires, and 2D materials) dramatically enhances their NLO response, particularly $\chi^{(3)}$effects. In bulk semiconductors, excitons are typically weakly bound due to the screening effect. The material's high dielectric constant reduces the Coulomb interaction between electrons and holes, leading to a lower exciton binding energy. As a result, the exciton radius becomes larger, often spanning several nanometers. This behavior is commonly observed in inorganic semiconductors such as gallium arsenide (GaAs) and cadmium sulfide (CdS) [38]. However, in nanostructures, such as CdSe quantum dots and GaAs quantum wells, quantum confinement can result in higher exciton binding energies. This occurs due to a reduced dielectric screening effect, which discretizes energy levels and enhances the oscillator strength. As a result, the exciton Bohr radius is reduced, leading to stronger Coulomb interactions [34]. Figure 3.1 shows the exciton binding energy versus the quantum confinement for different systems dimensionalities. In the case of 2D nanomaterials, such as CdSe-based NPLs, the exciton binding energies are significantly

higher than in bulk materials, reaching values around 300 meV, similar to those observed in monolayer WS_2 [39].

Figure 3.1 – Exciton binding energy versus quantum confinement. The references for the exciton binding energy values for bulk, quantum well, quantum wire, and quantum dot are [38], [40], and [41], respectively.

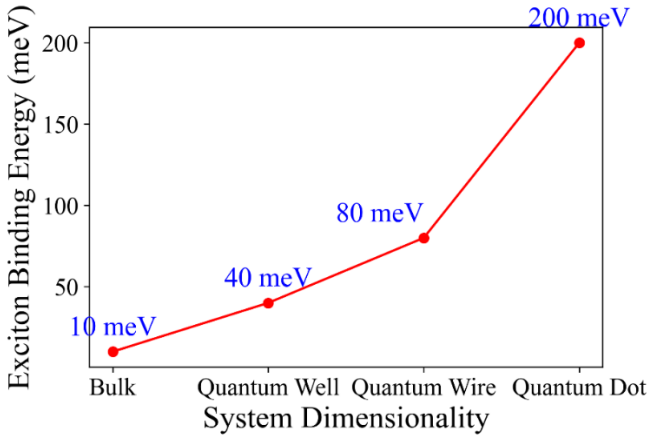

Source: The author (2025).

This strong exciton binding in nanostructured semiconductors significantly enhances resonant NLO effects such as two-photon absorption (TPA) and third-harmonic generation (THG). The enhanced excitonic transitions increase the probability of TPA, wherein two low-energy photons promote an electron to a higher-energy state, thereby boosting the third-order susceptibility [5, 22]. It is important to note that, in such cases, the third-order nonlinear response may include both instantaneous electronic contributions and population-related effects. In particular, under resonant or near-resonant excitation, real-state population mechanisms – such as excited-state absorption – can contribute significantly, indicating that the observed nonlinearity is not purely of an electronic Kerr-type origin. Moreover, the presence of these strongly bound excitons amplifies the nonlinear polarization response, leading to larger THG signals in semiconductor nanostructures, particularly in 2D materials, compared to bulk [42]. Furthermore, the increased Coulomb interaction in 2D systems enhances exciton-exciton interactions, leading to stronger four-wave mixing (FWM) processes, a key mechanism in optical signal processing [39, 41]. Table 3.1 exhibits the enhancement of the third-order susceptibility for some semiconductors systems due to the quantum confinement effect.

Another critical factor contributing to the increased $\chi^{(3)}$ in nanostructured materials is the appearance of discrete energy levels due to the quantum confinement effect. In bulk materials, the conduction and valence bands form a continuum of states, leading to smooth transitions. However, in nanostructures as 2D systems, the electronic states become quantized,

forming well-defined excitonic resonances [45]. This quantization effect significantly enhances NLO responses through density of states (DoS) and an increase in nonlinear coefficients at excitonic resonances (see Table 3.1). Unlike bulk materials with a $E^{1/2}$ DoS rule, 2D materials as quantum wells exhibits constant DoS within each sub-band (step-like), enhancing light-matter interaction [46]. Furthermore, well-defined excitonic states in 2D materials lead to strong optical nonlinearities, peaking near excitonic resonances [38]. Figure 3.2, shows a simplified representation of DoS for different systems dimensionality.

Table 3.1 – Third-order susceptibility enhancement for different nanostructured semiconductors systems.

System	Exciton Binding Energy	$\chi^{(3)}$ Enhancement	References
CdSe QDs (3 nm)	~50 meV	$10^3 \times$ bulk	[35]
GaAs Quantum Wells	~10 meV	$10^2 \times$ bulk	[43]
MoS_2 Monolayers	~500 meV	$10^4 \times$ bulk	[44]

Source: The author (2025).

Figure 3.2 – Different systems dimensionality, quantum confinements, and DoS diagrams.

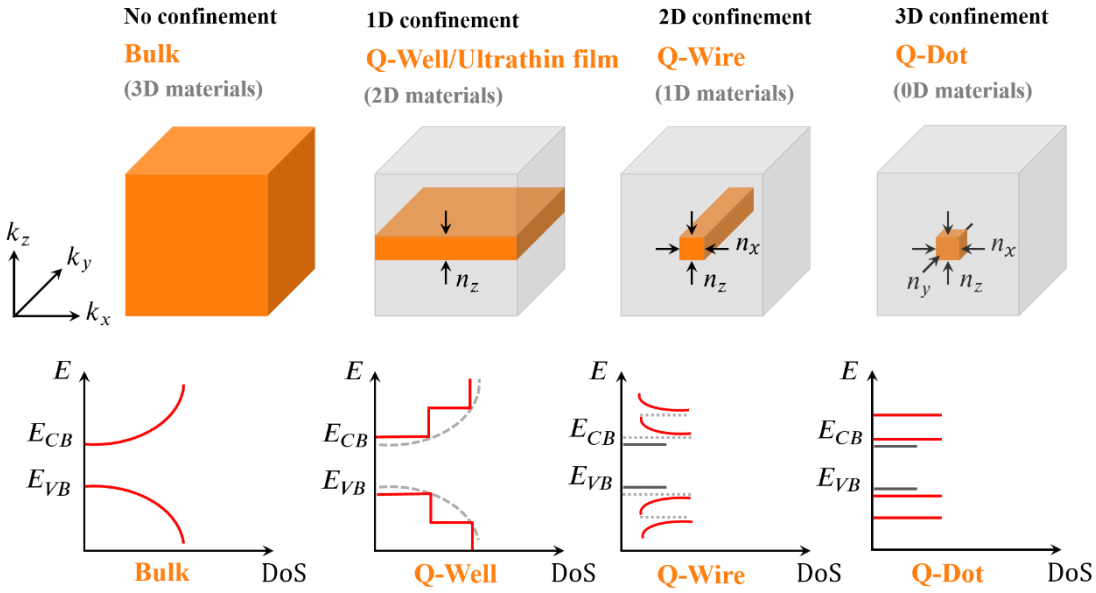

Source: The author (2025).

The previously discussed high exciton binding energies and discrete electronic states in nanostructured semiconductor systems play a vital role in enhancing third-order NLO effects. These characteristics lead to increased optical susceptibility, stronger multi-photon absorption,

and improved NLO conversion efficiencies. Consequently, nanostructured semiconductors are promising candidates for next-generation optoelectronic and photonic applications, such as ultrafast optical switches, nonlinear frequency converters, and all-optical signal processing devices.

In the next section, we will discuss the properties of 2D CdSe-based nanoplatelets (NPLs), which are promising photonic nanomaterials for the next generation of all-photonic devices. The unique properties of these materials make them suitable for use nonlinear optics, as laser emitters, and in quantum optics. These properties are particularly enhanced for fill-layer structures and core-shell NPLs.

3.2 CdSe Nanoplatelets as a Promising Photonic Nanomaterial

Colloidal CdSe-based nanoplatelets (NPLs) have emerged as highly promising materials for photonic applications due to their unique electronic and optical properties. Unlike conventional quantum dots (QDs), which are quasi-zero-dimensional structures, CdSe NPLs are quasi-two-dimensional (2D) systems that exhibit strong quantum confinement in the thickness direction while maintaining free carrier motion in the lateral dimensions. This distinctive structure results in several advantageous photonic properties, making them highly suitable for applications in light-emitting diodes (LEDs), lasers, nonlinear optics, and quantum optics.

CdSe NPLs exhibit strong quantum confinement, which leads to the discretization of their energy levels. They have atomically controlled thicknesses, typically ranging from two to six monolayers. This results in a strong confinement effect and the formation of distinct excitonic transitions. Consequently, CdSe NPLs demonstrate narrow emission line widths and efficient optical gain [47]. Furthermore, their emission energy can be precisely tuned by simply adjusting the number of monolayers, due to the thickness-dependent bandgap [48, 49]. Moreover, because of their 2D-like nature and reduced dielectric screening, CdSe NPLs exhibit large exciton binding energies (typically 100–200 meV), enabling stable excitonic emission even at room temperature [50, 51]. The high exciton binding energy contributes to high photoluminescence quantum yields (near unity) and stable emission properties [52]. Besides that, CdSe NPLs exhibit exceptionally large oscillator strengths and high absorption cross-sections due to the coherence of electronic wave functions across the plane of the platelets [47]. This coherence results in ultra-fast radiative lifetimes on the sub-nanosecond scale and significantly enhanced absorption cross-sections [53]. These outstanding properties make CdSe NPLs excellent candidates for applications in nonlinear optics and high-speed light modulation. In addition, due to the in-plane orientation of the transition dipole moment, CdSe NPLs emit strongly polarized light, with the emission predominantly confined to the platelet plane [54]. This makes them ideal for integration in planar photonic devices where polarized emission is advantageous.

CdSe NPLs demonstrate enhanced NLO properties, including strong two-photon absorption and efficient third-harmonic generation. These effects arise from their large oscillator strength and high exciton binding energy. As a result, these materials have been investigated for various applications, such as ultrafast optical switching and frequency

conversion [55]. Due to their impressive optical characteristics, CdSe NPLs show significant promise in photonic devices. They have been utilized in light-emitting diodes (LEDs) with high external quantum efficiencies and excellent color purity [49]. Additionally, they are being explored for low-threshold optically pumped lasers [56], nonlinear optical limiters [57], Kerr-based switching devices [55], and single-photon emission sources for quantum optics [58].

In a brief discussion, the potential of CdSe NPLs as the next generation of photonic nanomaterials was highlighted. These materials have applications ranging from ultrafast photonic devices to quantum optics photon sources. The following section will outline the typical synthesis protocols for colloidal CdSe NPLs, with a specific focus on the methods used to synthesize 4-monolayer (4 ML) CdSe NPLs and CdSe/CdS core/shell (CS) NPLs. Additionally, the section will discuss and present the results and techniques used for characterization.

3.3 Synthesis Protocols and Materials Characterization

The synthesis of CdSe NPLs typically follows colloidal methods, where precise control over precursor concentrations, reaction temperature, and ligand environment dictates the final morphology and optical properties of the nanostructures. Commonly, a hot-injection technique is employed, involving the rapid injection of cadmium and selenium precursors into a high-temperature solvent containing coordinating ligands [47, 48]. The synthesis of CS NPLs involves an additional epitaxial growth step, where a secondary semiconductor material is deposited onto the core structure to fine-tune electronic and optical interactions [49].

In the following subsection, we will describe the synthesis protocols used to create the 4 ML and CS CdSe NPLs structures studied in this thesis. We will emphasize the optical properties of these materials, which are fundamental to investigating their NLO properties. Additionally, we will present some results regarding their morphological characterization.

3.3.1 Layered and Core/Shell CdSe NPLs Structures

Professor Amitava Patra and his team synthesized the CdSe structures analyzed in this study. Professor Patra is a member of the Indian Association for the Cultivation of Science, where he works in the Department of Materials Science. He is also affiliated and Director (2020-2024) with the Indian Institute of Nano Science and Technology. His group's research focuses on ultrafast excited-state dynamics, energy transfer, and electron transfer in multidimensional quantum dots, gold nanoparticles, gold clusters, carbon dots, semiconducting polymers, graphene, porphyrin-based luminescent nanoparticles, and both up- and down-converted luminescent materials for photonic applications. Among their efforts, they also investigate efficient synthesis protocols for generating colloidal CdSe-based NPLs for photonic applications.

The CdSe nanostructures studied here are part of Dr. Ansuri Medda's doctoral thesis and have been detailed in several publications regarding synthesis methods and material characterization. This section aims to provide the reader with a fundamental understanding of the synthesis method, focusing particularly on the morphological and optical properties of the 4 ML and CS CdSe NPLs utilized in this research.

The synthesis protocol for growing CdSe NPLs was optimized by using cadmium $(\text{myristate})_2$ and selenium powder as the cationic and anionic precursors, respectively [59]. These precursors were dispersed in 1-octadecene, and anisotropic growth along the z-axis was

controlled by introducing cadmium acetate dihydrate as a short-chain ligand at 195 °C. The reaction proceeded at 240 °C for 12 minutes under an inert atmosphere. The resulting CdSe NPLs were purified using a size-selective precipitation method.

CdSe/CdS CS NPLs were synthesized via high-temperature colloidal epitaxy by depositing CdS layers onto the preformed CdSe cores [60]. In this process, the CdSe NPLs were mixed with cadmium oleate in 1-octadecene, and 1-octanethiol was added dropwise at 300 °C. Oleylamine was introduced as a capping ligand, and the reaction was maintained for 30 minutes.

Structural characterization via X-ray diffraction (XRD) and transmission electron microscopy (TEM) revealed that CdSe NPLs predominantly exhibit a zinc blende crystal phase, whereas the CdSe/CdS NPLs show a mixture of zinc blende and wurtzite phases. TEM images confirmed the rectangular shape of the CdSe NPLs with an average thickness of ~1.25 nm, and a significantly increased thickness of ~3.8 nm for the CS structures. Figure 3.3 shows the XRD patterns and TEM images for 3 ML, 4 ML, and 5 ML CdSe NPLs, while Figure 3.4 and Figure 3.5 exhibits these results for the CdSe/CdS CS structure.

Figure 3.3 – (A) XRD patterns of (a) 3 ML, (b) 4 ML, and (c) 5 ML CdSe NPLs. TEM images of (B) 3 ML, (C) 4 ML, and (D) 5 ML CdSe NPLs (inset: HRTEM).

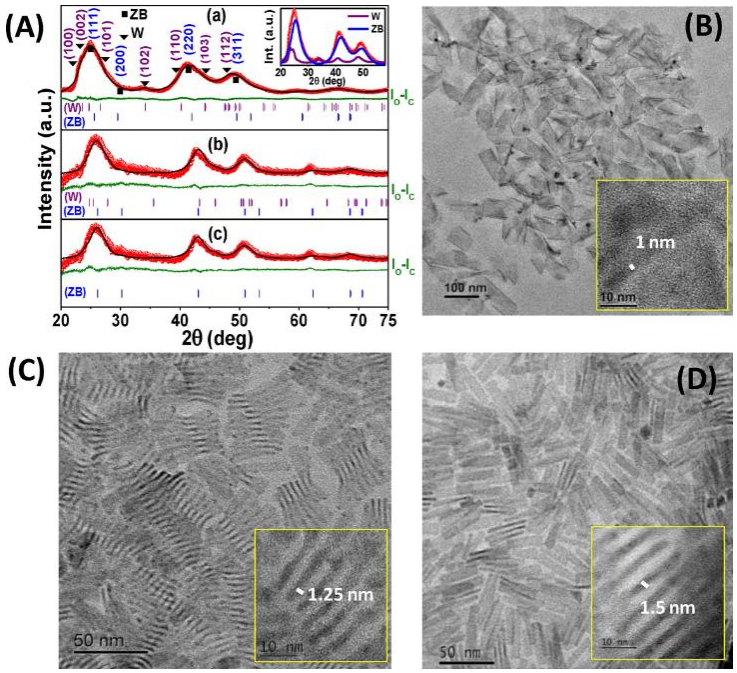

Source: A. Dutta *et al*. (2020). Ref. [59].

The lateral dimensions and thicknesses of the NPLs are different for 3, 4, and 5 ML NPLs. The measured lateral areas are ~ 260 ± 30 , 200 ± 30, and 220 ± 30 nm^2, for 3, 4, and 5 ML CdSe NPLs, respectively [59]. The average thickness is found from the high-

resolution TEM (HRTEM) (inset in Figure 3.3) and is estimated to be ~ 1, ~ 1.25, and ~ 1.5 nm for 3, 4, and 5 ML CdSe NPLs, respectively. The crystal structure and morphology of the CdSe/CdS CS NPLs are also investigated under HRTEM images. A representative top view of the images (Figure 3.5 (a, b)) confirms that the CS NPLs are well-dispersed and mostly rectangular in shape. Lateral dimensions of CS NPLs are obtained by measuring the statistical distribution of length (L) and width (W) of the NPLs. The mean length and width of the basal plane facets are found to be 25 and 15 nm, respectively [60]. The side-view image shown in Figure 3.5 (e) with a CdSe/CdS CS NPL "standing up" clearly reveals the total thickness of 3.8 nm, corresponding to a total shell thickness of ~ 2.6 nm around core CdSe NPLs of ~ 1.2 nm thickness. Moreover, the almost uniform thickness of the NPL suggests a consistent growth of the CdS shell around the CdSe core [60].

Figure 3.4 – (a) Archetypal simulated XRD pattern of CS CdSe/CdS NPLs. The red points and black and olive-green solid lines represent the observed (Io), calculated (Ic), and residual ($Io - Ic$) intensities, respectively. The vertical markers indicate the peak positions of WZ and ZB CdS phases. (b) Profiles of WZ (marked in blue color) and ZB (marked in dark-yellow color) CdS phases over the entire 2θ range of the XRD pattern. The significant reflections from both the phases are marked and indexed using the Miller indices of the corresponding planes in their bulk counterpart as a reference. (c) Mismatch in intensity between Io and Ic (highlighted using circles) in the absence of a CdSe phase. The goodness-of-fit (GoF) values indicate the quality of refinement.

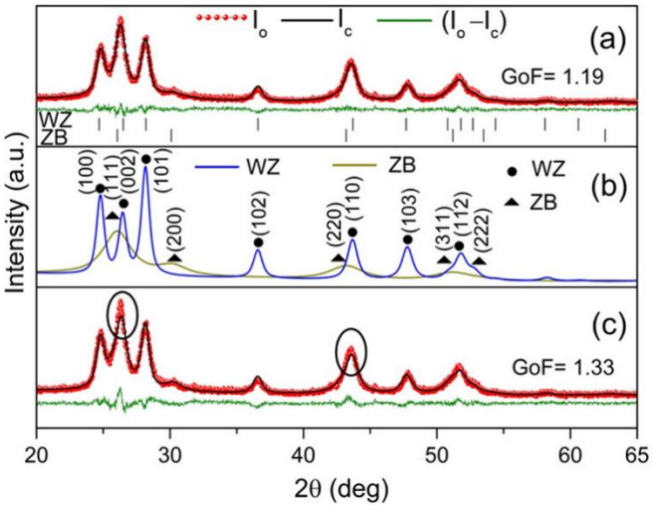

Source: A. Dutta *et al.* (2022). Ref. [60].

The optical properties were examined using UV-Vis absorption spectroscopy. CdSe NPLs displayed distinct heavy-hole (HH) and light-hole (LH) excitonic transitions at 505 nm and 477 nm, respectively. Upon CdS shell deposition, these transitions in the CS structures are red-shifted to approximately 665 nm and 600 nm, respectively, and the spectrum broadened due to shell growth [60]. Figure 3.6 shows the UV-Visible absorbance spectra for the 4 ML CdSe

and CdSe/CdS CS NPLs in toluene suspension. The absorbance of the 4 ML CdSe NPLs at 400 nm corresponds to 40% of that of the CS sample under identical measurement conditions. Assuming similar optical path lengths and extinction coefficients, this suggests a relative concentration of approximately 0.4.

Figure 3.5 – (a, b) Bright-field HRTEM images (top view) of the CdSe/CdS CS NPLs at different magnifications. Statistical distributions (histogram plots) shown in the inset of (b) indicating the mean length (L) and width (W) of the basal plane facets of the NPLs. (c) HRTEM image at a higher magnification. The fast Fourier transform (FFT) image along the [010] zone axis from the marked region (yellow square) is shown (inset). (d) Processed HRTEM image showing clear lattice planes from the marked region of (c). (d) HRTEM and (e) HRTEM showing the side view of a NPL and (f) processed HRTEM images showing lattice planes from both WZ and ZB phases inclined on either side of a boundary.

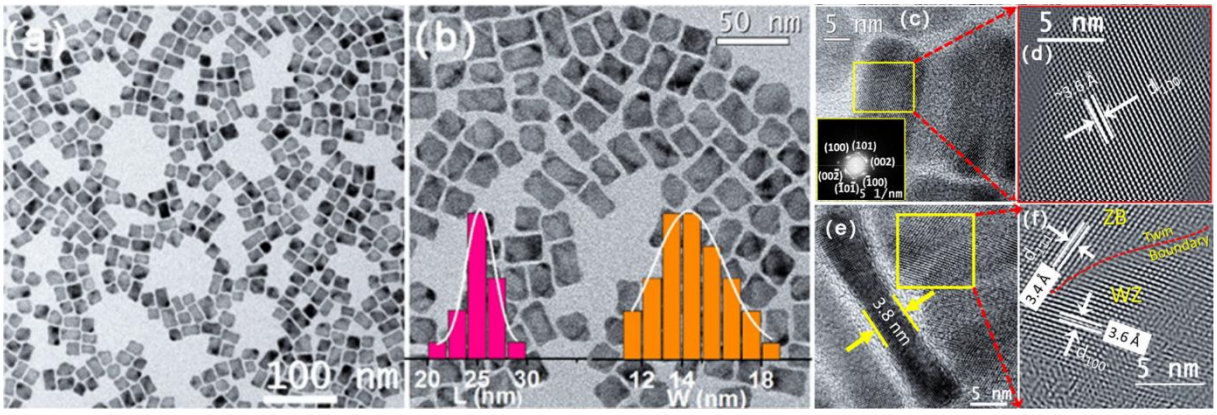

Source: A. Dutta *et al.* (2022). Adapted from ref. [60].

Figure 3.6 – Normalized UV-Visible absorbance spectra. (a) 4 ML CdSe NPLs, and (b) CdSe/CdS CS NPLs. Insets: samples' digital photographs. For the CdSe/CdS CS NPLs, zero absorbance occurs in the near-infrared region.

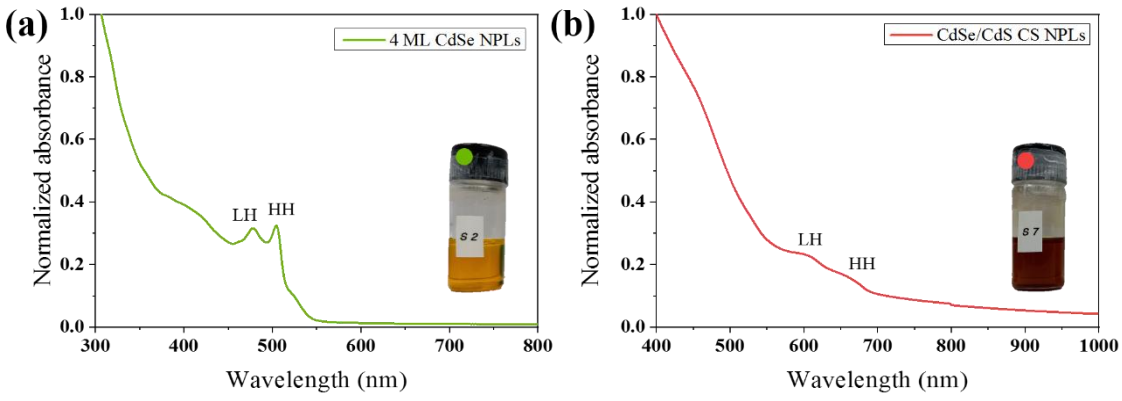

Source: The author (2025).

In the next section, we will present the results of our investigation into the NLO properties of the colloidal 4 ML and CS CdSe NPLs when excited by femtosecond laser pulses in a sub-bandgap excitation regime, which is a form of non-resonant excitation. We will discuss

the results related to the NLR and NLA responses of both samples using the Z-scan technique. Additionally, by applying the OKG method, we will analyze the time responses of these materials, as well as the magnitude of the refractive nonlinearity.

3.4 Measurements in the Non-Resonant Excitation Regime

In this section, we present the results of our investigation into the NLO properties of two-dimensional (2D) 4 ML CdSe and CdSe/CdS CS NPLs suspended in toluene. We utilized femtosecond Z-scan and nonlinear OKG techniques with an 800 nm excitation wavelength, which is far from any one-photon excitonic resonances. The Z-scan measurements allowed us to determine the coefficients for NLR and NLA. Meanwhile, the OKG technique provided insights into the time response of the nonlinearity and confirmed the third-order NLO coefficient obtained from the Z-scan results. We discuss the observed nonlinearities in relation to the electronic band structure of the materials.

3.4.1 Nonlinear Refraction and Nonlinear Absorption Responses

The effect of intensity-induced wave front distortion was investigated using the standard Z-scan technique to measure the sign and magnitude of the NLR and NLA coefficients for suspended CdSe NPLs samples. In the following subsections, we will provide details on the experimental setup, present the results, and discuss the findings.

3.4.1.1 Experimental Setup

The Z-scan experiment utilized an 800 nm amplified Ti:Sapphire laser (Coherent LIBRA, 120 fs pulses, 1 kHz repetition rate) as the light source. Departing from the standard Z-scan setup (Section 2.1.1), simultaneous open and closed aperture measurements were achieved by incorporating a beam splitter (BS) before the aperture (Figure 3.7). A reference arm adjusts for intensity fluctuations from pulse to pulse by normalizing the transmittance signals measured in both the open and closed aperture arms (see Figure 3.7). Samples are placed in a 1 mm transparent quartz cuvette and are scanned along the Z-direction around the focal point of a 150 mm lens. In this configuration, the beam waist at the focal point is approximately 21.3 μm, and the Rayleigh range is about 1.8 mm. It is important to note that maintaining a repetition rate of 1 kHz helps prevent thermal loading on the samples during scans, which ensures that only pure electronic nonlinearities are measured.

In the next subsection, we will present the results of the NLR and NLA coefficients obtained from the Z-scan experimental curves for all materials: pure toluene, 4 ML CdSe, and CdSe/CdS CS NPLs in suspension.

Figure 3.7 – Schematic Z-scan setup. Energy control is achieved using a half-wave plate (HWP) and a polarized beam splitter (PBS). Ten percent of the laser beam is directed to the reference detector, while the remaining ninety percent is sent to the Z-scan arms. Please note that the figure is not drawn to scale.

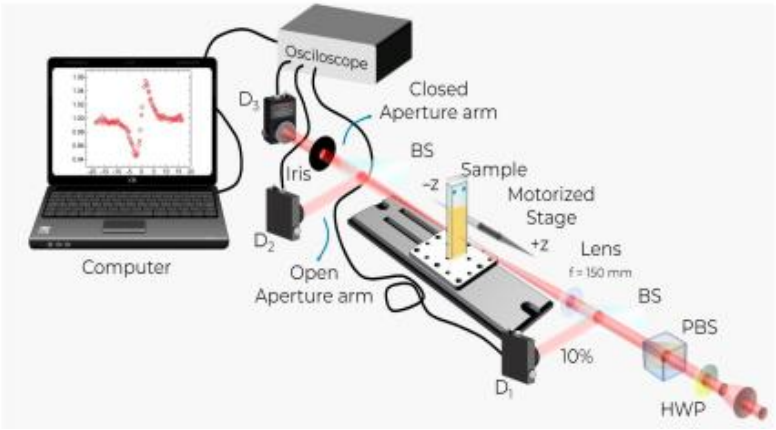

Source: Campos *et al*. (2024). Ref. [61].

3.4.1.2 Results

We begin by presenting the closed aperture (CA) Z-scan curves for the samples. Figure 3.8 displays the representative experimental CA Z-scan curves along with their respective theoretical fits for the CdSe-based NPLs in solution, as well as the results for the pure solvent. The peak intensity at the focus (I_0) for the measurements in Figure 3.8 was $I_0 = 244$ GW/cm². The red line is a fitting according equation (2.10) from which the value of the third-order NLR coefficient, n_2, is obtained. The calculated n_2 value for the pure toluene from the fit in Figure 3.8 (a) is $n_2 = +1.5 \times 10^{-16}$ cm²/W. The NLR coefficients for the CdSe-based NPLs in solution extracted from the theoretical curves in Figure 3.8 (b) and (c) are $n_2 = +1.4 \times 10^{-16}$ cm²/W and $n_2 = +1.2 \times 10^{-16}$ cm²/W, for the 4 ML CdSe and CdSe/CdS CS NPLs, respectively. The range of intensity applied for the NLR characterization was $61 - 610$ GW/cm². For intensities above 610 GW/cm², asymmetries appear in the valley-peak Z-scan patterns due to strong NLA effects resulting from the toluene response. The sign of n_2 is directly determined by observing the CA transmittance from the Z-scan experiments. The Z-scan signatures presented in Figure 3.8, reveal a positive sign due to a self-focusing effect, which holds for the entire range of intensities employed for all the materials.

By varying the intensity, the refractive index n_2 of toluene did not show a dependence on I_0 within the applied range. This indicates that only the third-order nonlinearity contributed to the solvent's response. In the case of the CdSe NPLs solutions, a resultant nonlinear phase shift occurs due to the combined contributions of the toluene and the NPLs. This results in

resultant NLR coefficients, which were extracted directly from Figure 3.8(b) and (c). As the changes in the transmittance patterns in Figure 3.8 (b) and (c) are not so significant this indicates that the refractive nonlinearity of the CdSe NPLs are suppressed by the solvent response. However, the valley-peak transmittance variations (ΔT_{v-p}) decrease for the CdSe NPLs curves as compared with the toluene curve for the same optical intensity (see Figure 3.8). This suggests that the refractive responses of the NPLs may have an opposite sign compared to toluene, then decreasing the total nonlinear phase shifts.

Figure 3.8 – Representative CA Z-scan data and theoretical fits. (a) Pure toluene, (b) 4 ML CdSe NPLs in toluene, and (c) CdSe/CdS CS NPLs in toluene. Data points are represented by spheres, and fits by red curves. Black lines indicate the linear baseline. The NLR index of the pure toluene is $n_2 = 1.5 \times 10^{-16}$ cm²/W. The NLR indexes for the solutions are $n_2 = 1.4 \times 10^{-16}$ cm²/W for 4 ML CdSe NPLs, and $n_2 = 1.2 \times 10^{-16}$ cm²/W for CS NPLs. The optical peak intensity was 244 GW/cm².

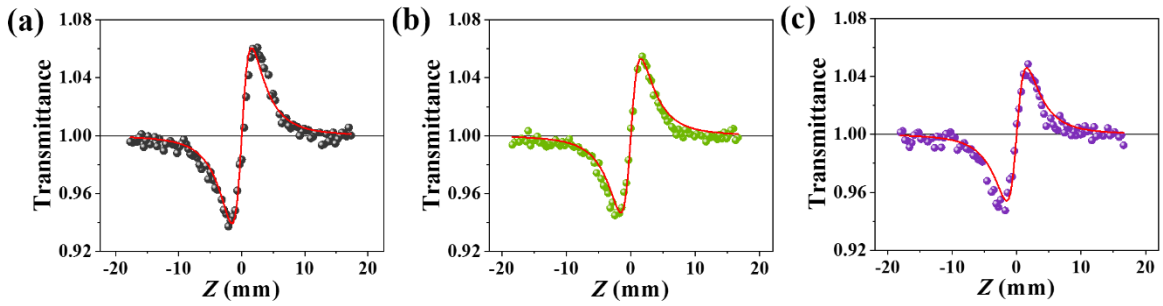

Source: The author (2025).

To assess the contribution of CdSe NPLs to the solution's third-order nonlinearity, we conducted a direct experimental comparison between the solution and the solvent. This was done by subtracting the nonlinear phase shift of toluene from that of the CdSe NPLs solution on a point-by-point basis, allowing the construction of a curve that represents the intrinsic nonlinear refraction response of the CdSe NPLs as a function of intensity. Figure 3.9 shows the comparison of the magnitude and sign of the third-order refractive index between the solvent and the CdSe NPLs in solution as the optical intensity increases. This figure demonstrates that the CdSe NPLs contribute to a reversal of the sign, which is "overshadowed" by the solvent's response, which is one order of magnitude stronger. The implications of these results will be discussed later.

We now turn our attention to the results of NLA extracted from open aperture (OA) Z-scan curves. Figure 3.10 displays the OA Z-scan results for both pure toluene and the CdSe NPLs solutions. The intensity applied at the focus was 732 GW/cm². The blue lines represent theoretical curves that consider only two-photon absorption (2PA), while the red lines, which

show a better fit with the experimental data, take into account pure three-photon absorption (3PA). Further discussion on the equations and additional physical aspects will be addressed later.

Figure 3.9 – n_2 versus I_0. Comparison of the magnitude and sign of the third-order NLR responses and solvent subtraction. (a) Toluene and 4 ML CdSe NPLs in solution, (b) toluene and CdSe/CdS CS NPLs in solution, and (c) pure CdSe NPLs NLR responses.

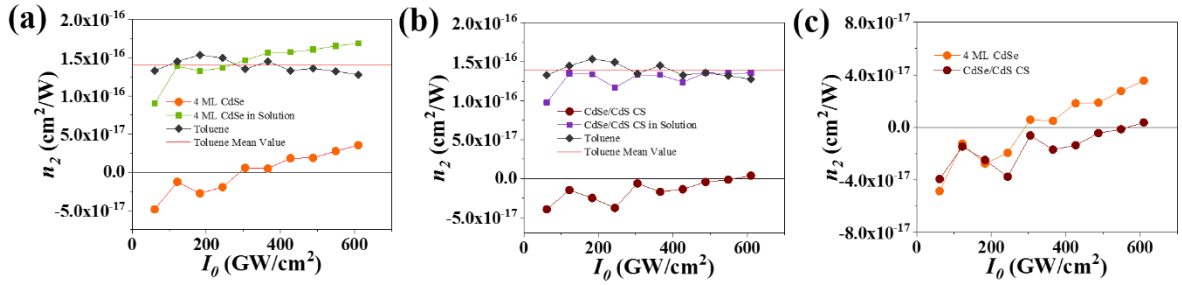

Source: The author (2025).

To describe the optical losses within the samples, we used equation (A.74) with $N = 3$, focusing solely on the two-photon absorption (2PA) effect. Then, we applied the equation again with $N = 5$, which accounts for the three-photon absorption (3PA) process, representing a higher-order effect of fifth order.

Figure 3.10 – Representative OA Z-scan data and theoretical curves. (a) Pure toluene, (b) 4 ML CdSe NPLs in toluene, and (c) CdSe/CdS CS NPLs in toluene. Data points are represented by spheres, while theoretical curves are depicted with red and blue lines. The NLA coefficients for toluene are $\alpha_2 = 6.8 \times 10^{-1}$ cm/GW, and $\alpha_4 = 6.2 \times 10^{-3}$ cm^3/GW^2. The NLA coefficients for the solutions are $\alpha_2 = 7.2 \times 10^{-1}$ cm/GW and $\alpha_4 = 6.8 \times 10^{-3}$ cm^3/GW^2 for the 4 ML sample, and $\alpha_2 = 5.2 \times 10^{-1}$ cm/GW and $\alpha_4 = 5.0 \times 10^{-3}$ cm^3/GW^2 for the CS sample. The optical intensity applied was 732 GW/cm^2.

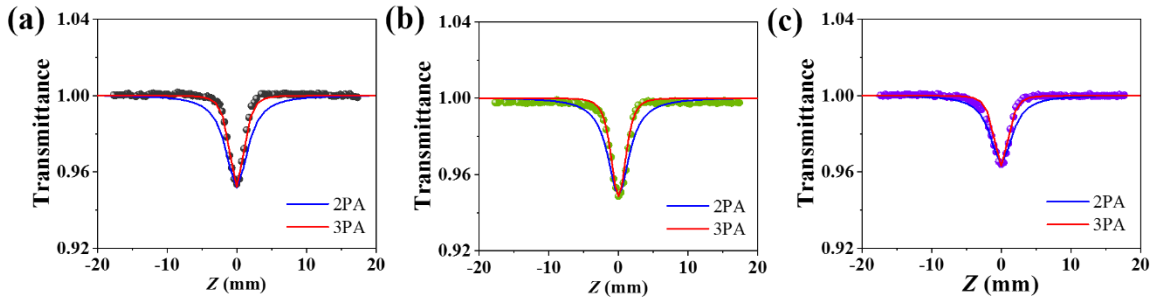

Source: The author (2025).

The values of the third and fifth-order NLA coefficients extracted from the models at 732 GW/cm^2 were $\alpha_2 = 7.2 \times 10^{-1}$ cm/GW and $\alpha_4 = 6.8 \times 10^{-3}$ cm^3/GW^2 for the 4 ML CdSe NPLs, and $\alpha_2 = 5.2 \times 10^{-1}$ cm/GW and $\alpha_4 = 5.0 \times 10^{-3}$ cm^3/GW^2 for the CdSe/CdS CS NPLs.

It is evident from Figure 3.10 (b) and (c) that the 3PA model ($N = 5$, red curves) fits better the experimental absorption data than the 2PA model (blue curves for $N = 3$). Similar behavior is observed for toluene, as shown in Figure 3.10 (a), from where the theoretical curve considering 3PA shows a better agreement with experimental data, resulting in $\alpha_4 = 6.2 \times 10^{-3}$ cm^3/GW^2, which has the same order of magnitude of the fifth-order NLA coefficients of 4 ML CdSe NPLs and CdSe/CdS CS NPLs in suspension. The OA transmittance data indicate that the CS sample is less absorbent compared to both the pure solvent and the 4 ML CdSe NPLs solution (see Figure 3.10). This indicate that the CdSe/CdS CS NPLs seem to decrease the effective two- and three-photon absorption cross-sections, which are directly proportional to the NLA coefficients.

For optical intensities ranging from 183 GW/cm² to 1222 GW/cm², we did not observe any dependence of the NLA coefficients on intensity, whether for the CdSe-based NPLs in suspension or in pure toluene. In this intensity range, toluene exhibits strong NLA responses, making it challenging to determine the specific role of the CdSe-based NPLs in the NLA effects observed in the solutions. To address this challenge and better understand the contributions of the NPLs, we conducted OA Z-scan experiments using lower intensities (30 GW/cm² to 183 GW/cm²), where no NLA response is observed in pure toluene (as the threshold for observing NLA in toluene via Z-scan is 183 GW/cm²). Figure 3.11 display representative OA Z-scan experimental curves along with theoretical fits for the 4 ML CdSe NPLs and CdSe/CdS CS NPLs in solution at 61 GW/cm² and 122 GW/cm², respectively.

The NLA coefficients extracted for 4 ML CdSe NPLs are $\alpha_2 = 4.0 \times 10^{-1}$ cm/GW, and $\alpha_4 = 4.0 \times 10^{-2}$ cm^3/GW^2. For CdSe/CdS CS NPLs, are $\alpha_2 = 1.7 \times 10^{-1}$ cm/GW, and $\alpha_4 = 0.9 \times 10^{-2}$ cm^3/GW^2. The results suggest that 3PA process is likely occurring in these dielectric systems, as the theoretical curves show a better fit. Furthermore, the dip in the OA Z-scan transmittance trace for the CS sample is less pronounced compared to the 4 ML result, even at twice the intensity (see Figure 3.11). This suggests that the CdSe/CdS CS NPLs reduce the fifth-order NLA cross-section of the solution. Additionally, it is important to emphasize that, within the spectro-temporal regime used in this study, the quartz cuvette does not display any nonlinear response.

In the following section, we will discuss in detail the results of the refractive and absorptive nonlinear responses of the CdSe-based NPLs in solution.

Figure 3.11 – Representative OA Z-scan data and theoretical curves below toluene threshold. (a) Solution of 4 ML CdSe NPLs excited at 61 GW/cm², and (b) solution of CdSe/CdS CS NPLs excited at 122 GW/cm². The insets display the toluene OA Z-scan traces corresponding to the intensities shown in (a) and (b). The orange line in the insets indicates the linear baseline where nonlinear absorption is absent.

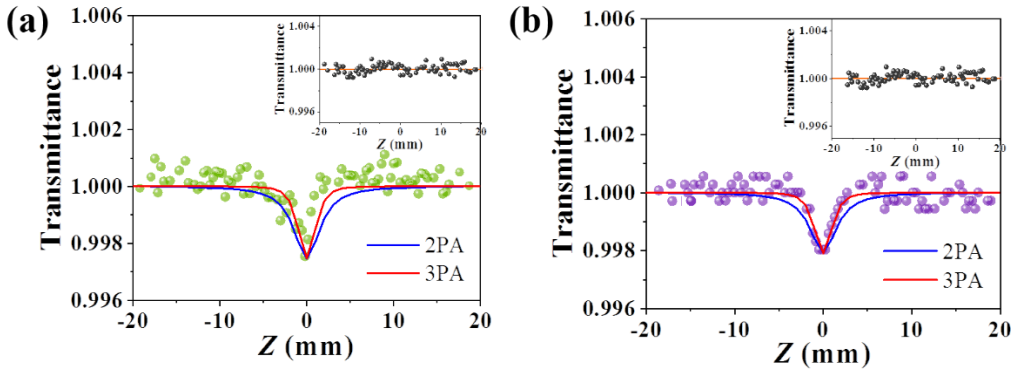

Source: The author (2025).

3.4.1.3 Discussion

Figure 3.9 (a) and (b) demonstrate that the third-order NLR responses of the CdSe NPLs in solution align with the solvent's self-focusing response. There is a slight increase in the n_2 value of the 4 ML CdSe sample beginning at approximately 300 GW/cm². The average value for toluene within the tested intensity range is $n_2 = +1.4 \times 10^{-16}$ cm²/W, as indicated by the red curves in the figures. After subtracting the toluene phase shift from the CA Z-scan data, Figure 3.9 (a) and (b) show the effective n_2 values for the 4 ML CdSe and CdSe/CdS CS NPLs. This subtraction reveals that the CdSe NPLs' contribution causes the sign reversal of the third-order nonlinearity, an effect masked by the toluene response. From Figure 3.9 (a) and (b), it is evident that the CdSe NPLs in suspension transition from a self-defocusing behavior to a self-focusing behavior. The threshold for the sign change in the n_2 of the 4 ML CdSe NPLs is 300 GW/cm². At this threshold, n_2 shifts from -2.8×10^{-17} cm²/W to $+1.9 \times 10^{-17}$ cm²/W. These represent mean values that contribute to the overall response of the solution, causing the NLR index value to deviate from the mean value of toluene after the threshold, as illustrated in Figure 3.9 (a). CdSe/CdS CS NPLs exhibit a threshold of 550 GW/cm^2 and a predominantly negative average n_2 of -1.9×10^{-17} cm^2/W, with the CS sample contributing to the solution's nonlinearity. The NLR response mirrors the solvent response, as shown in Figure 3.9 (b).

Figure 3.9 (c) demonstrates that the CdS core increases the self-focusing threshold by showing the refractive response of CdSe NPLs with intensity. CdSe/CdS NPLs are quasi-type-II semiconductors, where the electron wave function becomes delocalized in the CdS domain

while the hole remains confined in the CdSe region [62]. This spatial separation lessens the strength of local field interactions at lower intensities. Consequently, a higher intensity (meaning more carriers) is required to generate the polarization needed to reverse the sign of the Kerr response. Additionally, CdSe/CdS structures generally exhibit lower exciton binding energies due to reduced confinement, which results in less significant nonlinear refractive contributions from bound excitons [63]. These contributions frequently contribute negatively to the n_2. As a result, higher photon densities are necessary to achieve free carrier nonlinearities, which usually yield positive n_2 [62]. Moreover, electrons can "escape" into the CdS regions, causing the local carrier density to build up more slowly than in pure CdSe. This delay in local carrier density accumulation results in a higher threshold for achieving nonlinear refractive index inversion. Moreover, both materials demonstrate a positive slope in the n_2 versus I_0 curve (Figure 3.9 (c)), indicating that higher-order processes contribute to the nonlinear refractive response [64]. The earlier results from the NLA characterization suggest that the CdSe NPLs in suspension exhibit fifth-order susceptibility effect once the refractive and absorptive responses are connected.

Nawrot and collaborators also conducted Z-scan experiments to investigate the NLO properties of undoped, Cu-doped, and Ag-doped CdSe NPLs across a wide spectral range of 500 to 1500 nm using femtosecond optical pulses [64]. The authors observed a significant increase in NLA in the doped samples compared to the undoped sample. Notably, there were two distinct windows of pronounced NLA: one from 825 nm to 925 nm, which is associated with two-photon absorption, and another between 1100 nm and 1225 nm, related to a three-photon process. In CA Z-scan experiments, the values of the n_2 ranged from -9.95×10^{-17} cm²/W to 3.03×10^{-16} cm²/W [64]. Considering these values, the undoped CdSe NPLs with a thickness of 4.5 ML, suspended in chloroform, exhibited an n_2 of approximately -3.0×10^{-17} cm²/W at a wavelength of 800 nm, with a pulse duration of 130 fs, a repetition rate of 1 kHz, and an optical intensity of about 250 GW/cm² [64]. These conditions closely matched our experimental parameters. Nawrot and co-workers argue that even at the relatively high concentration of NPLs in solution, the NLR response of the samples is primarily influenced by the chloroform response. For the 4 ML CdSe NPLs, the value of n_2 below the threshold of 300 GW/cm² was found to be $n_2 = -2.8 \times 10^{-17}$ cm²/W. This value corresponds to results obtained by Nawrot et al. using the same phase subtraction technique. Table 3.2 summarizes the third-order refractive indices of the CdSe NPLs and the relevant solvents, as measured by the Z-scan technique, highlighting the intensity regime.

Table 3.2 - Nonlinear Refractive Index of CdSe NPLs and Relevant Solvents Based on Z-scan Experiments at 800 nm in the Femtosecond Temporal Regime.

Material	**Intensity range**	n_2 **(cm²/W)**	n_2^{eff} **(cm²/W)**	**Ref.**
4 ML CdSe	$61 - 610$ GW/cm²	$+1.5 \times 10^{-16}$	-2.8 to $+ 1.9 \times 10^{-17}$	This work
4.5 ML CdSe	~ 250 GW/cm²	----------	$\sim -3.0 \times 10^{-17}$	[64]
CdSe/CdS CS	$61 - 610$ GW/cm²	$+1.3 \times 10^{-16}$	-1.9×10^{-17}	This work
Toluene	$61 - 610$ GW/cm²	$+1.4 \times 10^{-16}$	----------	This work

Source: The author (2025).

The results presented in the previous section indicate that toluene activates the multiphoton absorption process only when the intensity reaches approximately 183 GW/cm², which is the threshold for NLA mechanisms in the solvent. Table 3.3 summarizes the NLA coefficients of the samples based on the applied intensity range. From Table 3.3, it is evident that above the toluene threshold, all samples exhibit a 2PA coefficient (α_2) within the same order of magnitude, and the values correspond to the observed dips in transmittance, as shown in Figure 3.10 for toluene and CdSe NPLs in solution, and in Figure 3.11 for the CdSe NPLs in solution below the toluene threshold. However, the width of the experimental OA Z-scan curves did not align with the theoretical 2PA curve, suggesting that a higher-order process is also involved as already discussed.

Table 3.3 presents the 3PA coefficients (α_4) for all samples extracted from the theoretical 3PA curves, which correspond with the dip and width of the experimental OA Z-scan curves. Above the toluene intensity threshold, the values of the 3PA coefficients are of similar order of magnitude, with the coefficient for the CS sample being approximately 1.3 times smaller than that of the toluene and the 4 ML samples. This difference is attributed to the delocalization electron wave function resulting from the presence of CdS in the shell of the NPLs, as previously discussed in the context of the refractive behavior. However, below the toluene intensity threshold, the α_4 coefficients of the CdSe NPLs increase significantly, becoming one order of magnitude higher than their values above the threshold. Notably, the 4 ML CdSe coefficient is around 4 times higher than that of the CS sample. This outcome occurs because we are measuring effective NLA coefficients. The solvent may possess a very weak 3PA coefficient that only becomes measurable at high intensities; it is below the detection threshold in the low intensity regime, but not truly zero. Consequently, at low intensities, the

NPLs dominates, while at high intensities, the NPLs saturates, giving the impression that they match. This scenario is likely if the solvent has electronic transitions near the three-photon resonance, especially during very short pulse durations (femtoseconds), where even small cross-sections can lead to observable effects, as is the case here.

Table 3.3 - Nonlinear Absorptive Coefficients of CdSe NPLs in Toluene Based on Z-scan Experiments at 800 nm in the Femtosecond Temporal Regime over an Intensity Range.

Material	**Intensity range**	α_2**(cm/GW)**	α_4**(cm^3/GW^2)**	**Ref.**
4 ML CdSe	$30 - 183$ GW/cm^2	4.0×10^{-1}	4.0×10^{-2}	This work
	$183 - 1222$ GW/cm^2	7.2×10^{-1}	6.8×10^{-3}	
CdSe/CdS CS	$30 - 183$ GW/cm^2	1.7×10^{-1}	0.9×10^{-2}	This work
	$183 - 1222$ GW/cm^2	5.2×10^{-1}	5.0×10^{-3}	
Toluene	$30 - 183$ GW/cm^2	------	------	This work
	$183 - 1222$ GW/cm^2	6.8×10^{-1}	6.2×10^{-3}	

Source: The author (2025).

Indeed, at the excitation wavelength of 800 nm (1.55 eV), two- and three-photon absorption (2PA and 3PA) processes may be considered for toluene. However, toluene does not exhibit strong two-photon absorption at this wavelength. This is because the combined energy of two 800 nm photons (2×1.55 eV $= 3.1$ eV, approximately 400 nm) is insufficient to reach its electronic transition bands, which are typically located in the range of 4.0 to 4.8 eV [65]. In contrast, the energy of three photons at 800 nm (3×1.55 eV $= 4.65$ eV, ~267 nm) lies within the absorption bands of toluene, particularly near the ^1L_a and ^1L_b transitions around 260 nm [65]. Although three-photon absorption is inherently weaker than two-photon absorption and usually requires very high peak intensities, the intensity range used in our experiments (from GW/cm² up to TW/cm²) is sufficient to enable this higher-order nonlinear process in toluene.

The multiphoton absorption process in the CdSe-based NPLs system can be understood as follows: In a direct band gap material, free excitons occur when the energy of the photon satisfies the relation $E_{photon} \equiv h\nu = E_g - E_b$, where E_g is the band gap energy and E_b is the exciton binding energy [67]. Consequently, the energy required to promote electrons from the valence band to the conduction band is expressed as $E_g = E_{photon} + E_b$. In the case of a 2PA process, this energy can be represented as $E_g = 2E_{photon} + E_b$. The photon energy is calculated

using the formula $E_{photn} = h\nu = hc/\lambda$, where λ is the photon wavelength, h is Planck's constant, and c is the speed of light in a vacuum. The exciton binding energy of 4 ML CdSe NPLs with approximately 1.4 nm in thickness, is $E_b = 270$ meV [68]. Therefore, the energy available in our dielectric system to facilitate 2PA will be approximately 3.35 eV. In their experiments, S. Ithurria *et al*. measured the electron/light-hole (LH) and electron/heavy-hole (HH) energy transitions for 4 ML CdSe NPLs, finding values of 3.347 and 3.167 eV, respectively [69]. Thus, a 2PA process is feasible in our CdSe-based NPLs system for both LH and HH excitonic transitions. For the CdSe/CdS CS NPLs system, the key difference lies in the presence of a redshift in the UV-Vis spectrum, which increases the wavelengths of the LH and HH excitonic transitions (see Figure 3.6). Nevertheless, the multiphoton absorption process can still occur because the condition $\lambda_{abs} < \lambda_{exc} < 2\lambda_{abs}$ is satisfied for both excitonic transitions, with λ_{abs} representing the wavelengths of LH and HH transitions, and λ_{exc} being the laser excitation wavelength.

Furthermore, the observed fifth-order NLA behavior can be attributed not to a genuine $\chi^{(5)}$ intrinsic process, but rather to a cascaded nonlinear mechanism involving free-carrier absorption. In this scenario, a 2PA process first excites electrons from the ground state to a virtual or real intermediate state using two simultaneous 800 nm photons. These excited carriers can then undergo a single-photon absorption from the same excitation beam, leading to an effective 3PA sequence. This stepwise process results in an intensity dependence characteristic of fifth-order absorption, yet it arises from a third-order nonlinear susceptibility ($\chi^{(3)}$) associated with 2PA, followed by a linear absorption ($\chi^{(1)}$) from the excited-state population. Therefore, the data suggest that the observed nonlinear response is best interpreted as a $\chi^{(3)} - \chi^{(1)}$ cascaded effect, rather than a true $\chi^{(5)}$ nonlinearity.

Given that the observed fifth-order behavior likely results from a cascaded $\chi^{(3)} - \chi^{(1)}$ process involving free-carrier absorption, the fifth-order coefficients extracted from the Z-scan fits should be interpreted phenomenologically rather than as true $\chi^{(5)}$ material parameters. These coefficients effectively describe the intensity dependence of the NLA within the experimental conditions but do not correspond directly to an intrinsic fifth-order susceptibility. Instead, they capture the outcome of a composite mechanism, where the intensity-squared dependence of the absorption coefficient mimics a $\chi^{(5)}$-like signature due to the sequential nature of the underlying absorption events. As such, these coefficients are useful for modeling

and comparing experimental results but must be interpreted with caution when inferring fundamental material properties.

To our knowledge, follows a comparison of a few publications addressing the NLA properties of layered CdSe NPLs and CdSe/CdS CS NPLs. Fang and colleagues employed an OA Z-scan technique to investigate the NLA properties of CdSe NPLs dispersed in hexane, using picosecond optical pulses at a wavelength of 532 nm [57]. They examined a non-resonant spectral region for a few-layer CdSe NPLs and a resonant spectral region for the CdSe/CdS CS structure. For the layered CdSe NPLs, an effective 3PA was reported, with optical intensities ranging from 19 GW/cm² to 78 GW/cm². The effective 3PA coefficient was measured at 4.7×10^{-2} cm³/GW² for intensities above 25 GW/cm², very close to our value reported in Table 3.3. Regarding the CdSe/CdS core/shell structure, the authors observed saturable absorption behavior at approximately 3.9 GW/cm², which transitioned to reverse saturable absorption for intensities exceeding 7.8 GW/cm².

In the following section, we will present a time-resolved analysis of the CdSe-based NPLs in suspension using the optical Kerr gate (OKG) technique within the non-resonant ultrafast regime.

3.4.2 Time Resolved Measurements

As we previously discussed, the OKG technique relies on the polarization rotation of a probe beam and involves a third-order nonlinear process. This technique provides insights into the NLR index value of the medium and its response time, giving a clue to the physical processes that lead to nonlinearity. In this section, we will present the results of the OKG measurements conducted on CdSe-based NPLs in suspension, as well as the responses observed from the solvent.

3.4.2.1 Experimental Setup

In the OKG experiment, the beam from a mode-locked Ti:Sapphire laser (Mira, Coherent), which operates at 76 MHz with a pulse duration of 185 femtoseconds at a wavelength of 800 nm, was divided into pump and probe beams. After adjusting the time delay, these beams were recombined at the focal point of a 100 mm lens, where a sample (a 1 mm quartz cuvette containing the suspension) was placed. The polarizations of the pump and probe beams were rotated by 45° degrees to guarantee maximum OKG signal. A polarized beam

splitter (PBS) with crossed polarization (90° degrees) relative to the probe was used as an analyzer. Figure 3.12 shows in details the OKG setup used in the measurements.

Figure 3.12 – Experimental apparatus for the OKG measurements. The figure is out of scale.

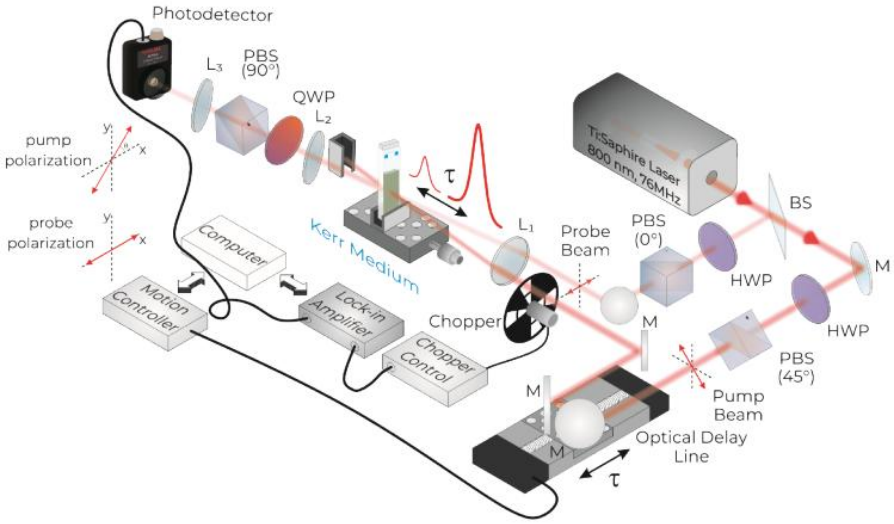

Source: Carvalho *et al*. (2023). Ref. [29].

In the figure, the optical delay line at the pump arm enables time-resolved superposition of the two beams. Half-wave plates (HWPs), along with polarizers in each arm, are used to control the power of both the pump and probe beams. When a Kerr medium is present, the pump beam induces a third-order intensity-dependent change in the medium's refractive index. This change creates a nonlinear birefringence that the probe beam experiences, functioning as an optically gated optical switch. The signal transmitted by the analyzer, known as the OKG signal, is measured using a free-space amplified photodetector (PDA100A, Thorlabs), which is triggered by a chopper and a lock-in amplifier (SR830 DSP, Stanford Research Systems). The system operates in the heterodyne regime, with a portion of the probe intensity leakage controlled by a quarter-wave plate (QWP). The duration of the pulses obtained from the intensity autocorrelation measurement is 180 fs at the sample position.

3.4.2.2 Results

The results for the OKG measurements are presented in Figure 3.13 (a) – (c). The OKG system was calibrated using carbon disulfide (CS_2), a well-characterized NLO material [69]. Figure 3.13 (a) illustrates typical OKG curves, highlighting the response times of Beta Barium Borate (BBO) crystal, CS_2, toluene, 4 ML CdSe, and CdSe/CdS CS NPLs in solution. These curves are normalized to facilitate a clear observation of the decay time. Notably, the laser pulse duration was measured to be 185 fs, determined through intensity autocorrelation of the pulses,

for which we used a BBO crystal for second-harmonic generation. Figure 3.13 (b) and (c) display the evolution of the Kerr response as a function of pump intensity, ranging from 185.1 MW/cm² to 834.4 MW/cm². This intensity range is three orders of magnitude lower than that of the Z-scan measurements. It is important to note that, despite using a high repetition rate excitation source, thermal response does not influence the OKG measurements as it does in other experimental methods, such as Z-scan or spatial self-phase modulation. This is because the OKG experiments focus on polarization rotation.

From the OKG data, the information about the materials' n_2 modulus can be retrieved by comparing their OKG signals with the OKG signal of a standard medium according to the following relation [29]:

$$\frac{n_2^S}{n_2^R} = \frac{I_{OKG}/I_{pump}{}^S}{I_{OKG}/I_{pump}{}^R}\left(\frac{L_{eff}^R}{L_{eff}^S}\right)\sqrt{\frac{T_0{}^R}{T_0{}^S}}\sqrt{\frac{I_{probe,R}}{I_{probe,S}}} \tag{3.1}$$

where the superscript indices S and R refer, respectively, to sample and reference. As the reference nonlinear material, we employed CS_2, for which we considered $n_2^{CS_2} = (3.1 \pm 1.0) \times 10^{-15}$ cm^2/W, as reported by Couris et al. based on the well-established Z-scan technique [69]. It is important to note that our OKG apparatus operates in a heterodyne regime. This means that any linear phase shift caused by probe leakage (T_0 in equation (3.1)) through the PBS analyzer must be considered, as per the method described in equation (3.1). A detailed mathematical development of this method can be found in reference [29].

Figure 3.13 – OKG measurements for four different samples (a) highlighting the time response; (b) by changing the optical intensity for 4 ML CdSe NPLs; and (c) by changing the optical intensity for CdSe/CdS CS NPLs. The NLR values obtained are $n_2 = 2.1 \times 10^{-16}$ cm^2/W for 4 ML CdSe NPLs and $n_2 = 1.1 \times 10^{-16}$ cm^2/W for CdSe/CdS CS NPLs.

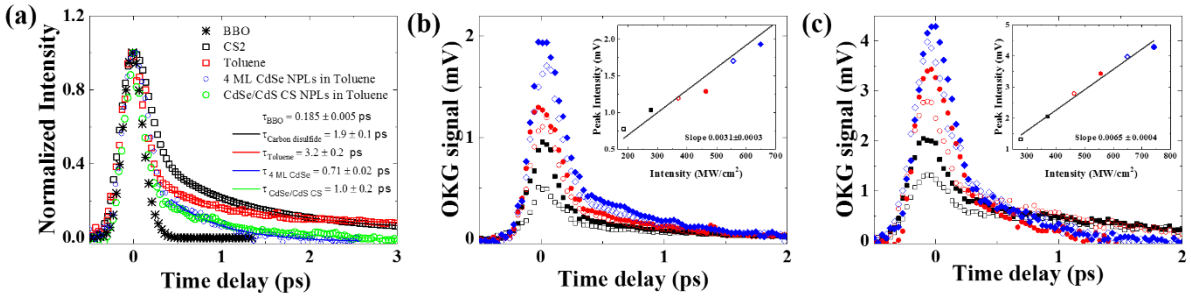

Source: Gonçalves *et al*. (2023).

The time response of the nonlinearity is clearly illustrated in the plots of Figure 3.13. The presence of characteristic tails indicates a slow orientational nonlinearity, which occurs

over a time scale of approximately 2 picoseconds (ps), superimposed on a fast response that follows the femtosecond pulse width of the optical signal. For CS_2, the time decay was measured at 2.0 ps, which aligns well with reported values in the literature [70, 71]. In contrast, toluene exhibited a decay time of 3.2 ps, roughly five times longer than that of the sample containing 4 ML CdSe NPLs. This suggests that the fast response of the NPLs significantly contributes to the overall signal observed in the OKG measurements. Additionally, a shorter response time is noted for the suspension of CdSe/CdS CS structures, which displayed a decay time of 1.0 ps, further affirming that the nanostructures enhance the observed nonlinear effects. However, it is essential to highlight that the presence of tails in the OKG signal from the CdSe-based samples in solution, despite their slower decay time, indicates that the nonlinear properties of the samples are comparable to those of the solvent, as supported by the Z-scan measurements presented in Table 3.4.

In the following section, we will discuss the results of the third-order nonlinear time responses of the CdSe-based NPLs in solution and the relevant solvents.

Table 3.4 – Nonlinear Refractive Index of 4 ML CdSe NPLs, CdSe/CdS CS NPLs, and Relevant Solvents Based on Z-scan Experiments and OKG Technique Around 800 nm, Femtosecond Temporal Regime*.

Material	$n_{2,Z-scan}^{eff}$ **(cm²/W)**	$n_{2,Z-scan}$ **(cm²/W)**	$n_{2,OKG}$ **(cm²/W)**	**Response Time**	**Ref.**
4 ML CdSe	-2.8 to $+1.9 \times 10^{-17}$	$+1.5 \times 10^{-16}$	2.1×10^{-16}	Fast(0.185 ps) slow (0.7 ps)	This work
CdSe/CdS CS	-1.9×10^{-17}	$+1.3 \times 10^{-16}$	1.1×10^{-16}	Fast(0.185ps) slow(1.0 ps)	This work
Toluene	------	$+1.4 \times 10^{-16}$	------	Fast(0.185 ps) slow (3.2 ps)	This work
CS_2	------	$+3.1 \times 10^{-15}$	------	Fast(0.185 ps) slow (1.9 ps)	[71]

* *Response time from the OKG technique is also presented.*

Source: The author (2025).

3.4.2.3 Discussion

In molecular solvents such as CS_2 and toluene, the nonlinear signal is dominated by molecular reorientation under the influence of the optical field. The decay time measured for CS_2 was 2.0 ps, in excellent agreement with values reported in the literature [70, 71], validating

the experimental approach. Toluene exhibited a longer decay time of 3.2 ps, reflecting its comparatively slower molecular reorientation, likely due to higher viscosity and molecular inertia.

Upon introducing CdSe NPLs into toluene, a substantial shift in the nonlinear temporal dynamics was observed. The suspension containing 4 ML CdSe NPLs exhibited a significantly shorter decay time of approximately 0.7 ps. This pronounced acceleration in the nonlinear optical response can be attributed to the strong polarizability anisotropy and rapid field-induced alignment of the quasi-two-dimensional NPLs. Their flat geometry and strong in-plane transition dipole moments contribute to a fast, coherent third-order response that dominates over the slower molecular background of toluene.

Interestingly, the CdSe/CdS CS NPLs displayed a slightly longer decay time of 1.0 ps compared to the bare 4 ML CdSe NPLs. This indicates that the presence of the CdS shell introduces a modest delay in the orientational relaxation. The CdS shell, with its larger bandgap and increased mechanical rigidity, likely enhances the structural stability and modifies the overall dielectric environment of the NPLs [72]. However, it also adds mass and changes the aspect ratio of the nanostructures, which could contribute to slightly slower rotational dynamics under the influence of the optical field.

The presence of characteristic long decay tails in all cases signals a slow orientational contribution superimposed on a rapid electronic response that follows the femtosecond laser pulse envelope. The faster decay times observed in the NPLs suspensions – particularly in the layered CdSe NPLs – demonstrate that these nanostructures provide a strong and ultrafast contribution to the third-order nonlinearity. The slightly slower response of the CS samples highlights the trade-off introduced by structural modifications: while the shell may enhance optical stability and field confinement, it can simultaneously influence the dynamics of orientational relaxation.

It is important to highlight that the decay time extracted from the OKG signal of the NPLs in solution represents a composite response arising from both the nonlinear contribution of the solvent (toluene) and the intrinsic response of the CdSe-based nanostructures. As a result, the measured temporal dynamics do not correspond exclusively to the NPLs but rather to an effective time constant that reflects the superposition of both components. Isolating the pure NPLs response would require either deconvolution approaches or complementary time-resolved techniques, such as transient absorption spectroscopy.

In the following section, we will discuss the results of the nonlinear response of the CdSe-based NPLs in resonance with the heavy-hole (HH) excitonic transitions using the Z-scan approach.

3.5 Measurements in the Resonant Excitation Regime

In this section, we present the NLO refractive and absorptive responses of 4 ML CdSe NPLs and CdSe/CdS CS NPLs suspended in toluene. These were excited at resonance with the heavy-hole (HH) excitonic transitions in the femtosecond regime using the Z-scan method. This study took place during a three-week scientific visit in 2023 at the Physics Institute of São Carlos (IFSC) at the University of São Paulo (USP), Brazil.

The measurements were conducted using the facilities of the IFSC's photonics group (GFo), coordinated by Prof. Dr. Leonardo De Boni, specifically in the nonlinear optics laboratory. This laboratory is equipped with Ti:Sapphire laser amplifier systems (mJ and kHz) that produce femtosecond pulses at 800 nm. Wavelength tunability is achieved by utilizing Optical Parametric Amplifiers that are pumped by the Ti:Sapphire laser.

3.5.1 Experimental Setup

The experimental setup was based on the standard Z-scan apparatus described in Section 2.1. The setup included a femtosecond laser source (PHAROS, Light Conversion), which delivered pulses with a temporal width of 190 fs and a repetition rate of 750 Hz to avoid thermal effects. This was coupled with a collinear optical parametric amplifier (TOPAS, Light Conversion), allowing for tuning of the wavelength from 189 to 2000 nm. The arrangement facilitated both open- and closed-aperture measurements and included a reference arm to correct for pulse-to-pulse fluctuations. The samples were placed in 1 mm transparent quartz cuvette and scanned along the $\pm z$ direction through the focal point of a 150 mm converging lens. The wavelengths chosen for the Z-scans were 505 nm and 665 nm, corresponding to the HH excitonic transitions of the 4 ML CdSe NPLs and CS NPLs, with beam waists at the focal point of approximately 20 μm and 18 μm, respectively. The absorption spectra of the NPLs in toluene are presented in Figure 3.6.

3.5.2 Results

Figure 3.14 (a) displays the closed-aperture (CA) pattern along with the theoretical fit (shown by the red line) for the solvent at an intensity of 17.54 GW/cm². From the experimental and theoretical curves, it is possible to calculate the signal (which is positive, indicating a self-focusing NLR) and the magnitude of the toluene NLR coefficient, given by ${n_2}^{505}\,(toluene) = +1.7 \times 10^{-15}$ cm²/W. The empty 1 mm quartz cuvette does not exhibit any NLR response at this intensity level. Figure 3.14 (b) and (c) present the CA Z-scan signatures at 505 nm of

excitation, along with the fitted curves for the 4 ML CdSe and CS NPLs in solution, respectively. The 505 nm wavelength corresponds to the HH exciton resonance of the 4 ML sample, and the CS sample possess significant linear absorption in this spectral region. Additionally, Figure 3.14 (b) and (c) illustrate the CA Z-scan patterns and theoretical adjustments for the 4 ML CdSe NPLs and CS NPLs at $I_0 = 17.54$ GW/cm². However, the theoretical fits for the CdSe-based NPLs at 505 nm are not well-aligned due to the influence of strong one-photon saturable absorption (SA) at this wavelength. This theoretical approach will be discussed later in the text.

Figure 3.14 – CA Z-scan signatures at 505 nm of excitation. (a) Toluene, (b) 4 ML CdSe NPLs in solution, and (c) CdSe/CdS CS NPLs in solution. The red curves represent theoretical predictions for a third-order refractive nonlinearity, while the horizontal gray lines indicate the linear baseline. The optical intensity applied was $I_0 =$ 17.54 GW/cm². The NLR coefficients extracted from the fits are: $n_2^{505}(toluene) = +1.7 \times 10^{-15}\ cm^2/W$, $n_2^{505}(4\ ML) = +3.2 \times 10^{-14}$ cm²/W, and $n_2^{505}(CS) = +5.9 \times 10^{-15}$ cm²/W.

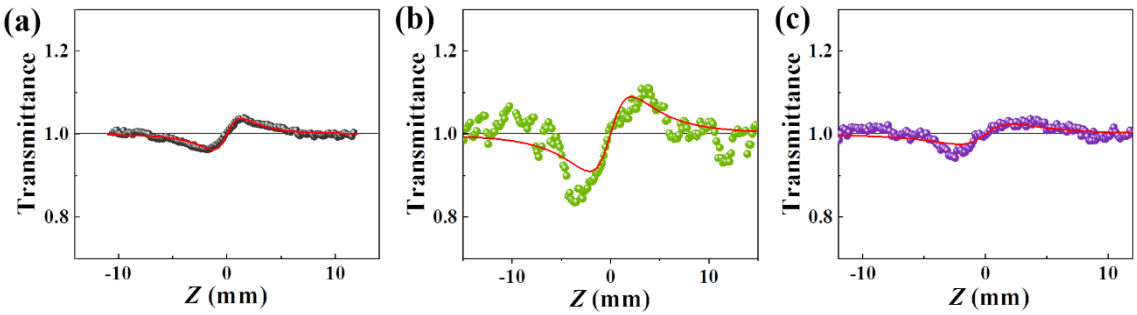

Source: The author (2025).

Figure 3.15 (a) displays the open-aperture (OA) measurement for pure toluene in a 1 mm quartz cuvette, demonstrating that there is no nonlinear optical absorption or saturated absorption observed up to the maximum intensity of 140 GW/cm². Figure 3.15 (b) and (c) present the OA Z-scan signatures along with the theoretical fits for the CdSe-based NPLs, confirming that a one-photon SA process occurs in these dielectric systems. The focused intensity (I_0) applied was 35.07 GW/cm². Based on the OA theoretical fits, we can extract the one-photon saturation intensities (I_S) at 505 nm for the CdSe-based NPLs samples. The system is examined in a non-perturbative regime, requiring a complete intensity-dependent model. In this context, the response cannot be attributed solely to third-order nonlinearity. A discussion of the theoretical treatment will be provided later in the text.

We conducted Z-scan experiments at a wavelength of 665 nm, which corresponds to the HH excitonic transitions of colloidal CS NPLs, as shown in Figure 3.6. For comparison, we

also performed Z-scan experiments on the sample of 4 ML CdSe NPLs at the same wavelength. In this case, we did not observe any SA response, as 665 nm is far from the excitonic transitions of this material (which occur at 505 nm) and exhibits very low absorption in the 600 nm region.

Figure 3.15 – OA Z-scan signatures at 505 nm of excitation. (a) Toluene, (b) 4 ML CdSe NPLs in solution, and (c) CdSe/CdS CS NPLs in solution. The red curves represent theoretical predictions for saturated absorbing mediums, while the horizontal gray lines indicate the linear baseline. In Figures (b) and (c) the optical intensity applied was 35.07 GW/cm^2. The saturation intensities are $I_s = 1.20$ GW/cm^2 for 4 ML CdSe NPLs and $I_s = 1.40$ GW/cm^2 for CS NPLs.

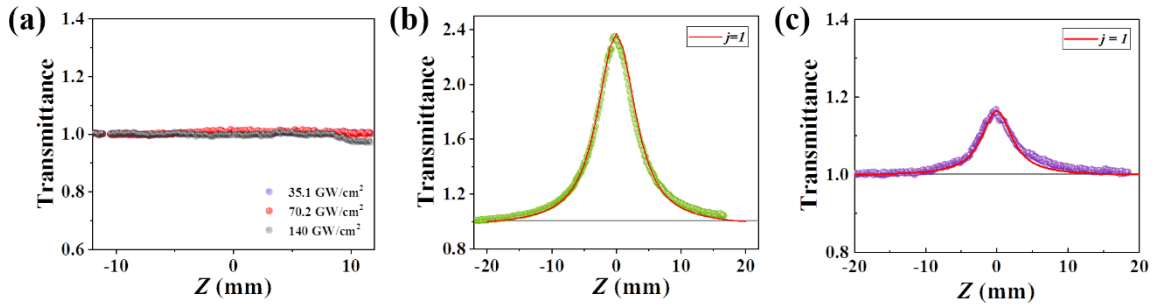

Source: The author (2025).

Figure 3.16 (a) – (c) exhibits the CA Z-scan traces for the excitation at 665 nm for all the samples studied. Figure 3.16 (a) exhibits the pure toluene CA representative signal and its theoretical adjustment (red line). It is possible to compute the solvent NLR contribution at 665 nm of excitation at $I_0 = 216.6$ GW/cm^2, resulting in $n_2^{665}(toluene) = +1.32 \times 10^{-15}$GW/cm^2. Figure 3.16 (b) and (c) are the CA Z-scan signals for the 4 ML and CS CdSe NPLs, respectively. The intensities are $I_0 = 173.3$ GW/cm^2 and $I_0 = 216.6$ GW/cm^2 to achieve the signals showed in the figures. The NLR coefficients for the CdSe-based dielectric systems in suspension are $n_2 = +2.8 \times 10^{-15}$ cm^2/W and $n_2 = +4.9 \times 10^{-15}$ cm^2/W for CS NPLs and 4 ML CdSe NPLs, respectively.

Figure 3.17 (a) shows the OA Z-scan curve for pure toluene, which indicates that no SA or multiphoton signals are observed up to 173.3 GW/cm² for the solvent in a quartz cuvette at an excitation wavelength of 665 nm. The OA Z-scan signatures for the CdSe-based NPLs in toluene are displayed in Figure 3.17 (b) and (c). Figure 3.17 (b) demonstrates that no NLA mechanism occurs for the 4 ML CdSe NPLs. This finding is consistent with the absorption spectrum of this sample (Figure 3.6 (a)), as 665 nm lies far from the excitonic absorption peaks, resulting in negligible linear absorption. In contrast, the OA signal indicates that one-photon SA occurs for the CS NPLs system at 665 nm, as shown in Figure 3.17 (c). This result is expected, given that 665 nm corresponds to the HH excitonic transition of the CS NPLs (refer

to Figure 3.6 (b)). The intensity at focus used in this measurement was $I_0 = 43.32$ GW/cm², which achieved the OA Z-scan amplitude presented in Figure 3.17 (c).

Figure 3.16 – CA Z-scan signatures at 665 nm of excitation. (a) Toluene, (b) 4 ML CdSe NPLs in solution, and (c) CdSe/CdS CS NPLs in solution. The red curves represent theoretical predictions for a third-order refractive nonlinearity, while the horizontal gray lines indicate the linear baseline.

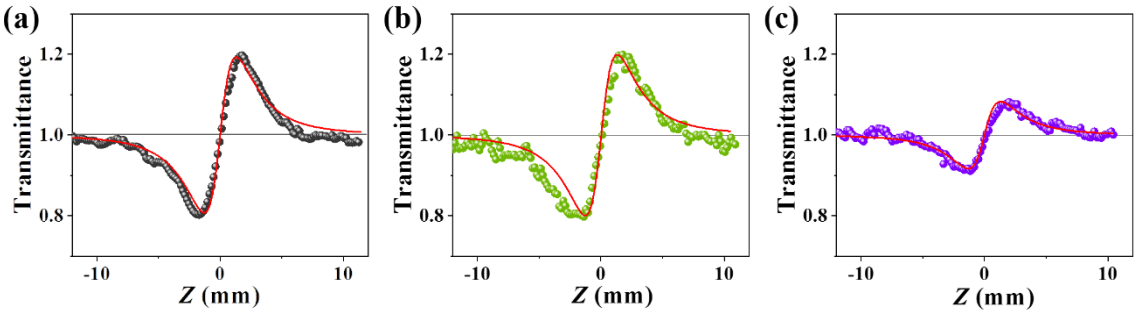

Source: The author (2025).

Figure 3.17 – OA Z-scan signatures at 665 nm of excitation. (a) Toluene, (b) 4 ML CdSe NPLs in solution, and (c) CdSe/CdS CS NPLs in solution. The red curves represent theoretical predictions for a saturated absorbing medium, while the horizontal gray lines indicate the linear baseline. The saturation intensity is $I_s = 3.5$ GW/cm² for CS NPLs.

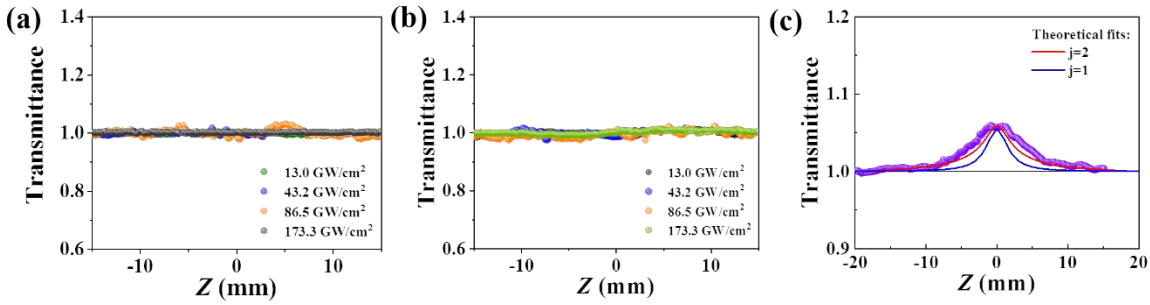

Source: The author (2025).

The following section discusses the presented results, including the extracted nonlinear coefficients for the applied excitation wavelengths. It also compares the resonant nonlinearities with the previously studied non-resonant case.

3.5.3 Discussion

By setting $\Delta\Phi_0^{(3)}$ as a free parameter in equation (2.10), we can generate theoretical normalized transmittance curves that fit the experimental CA Z-scan curves. This approach allows for the indirect measurement of the sample's n_2 value as described in equation (2.10). The CdSe-based NPLs in toluene exhibit a positive n_2, indicated by a valley-peak pattern in the $+z$ direction. This suggests an electronic contribution to the third-order NLR, as shown in

Figure 3.14 (b), (c) and Figure 3.16 (b), (c). Moreover, the solvent displays the same NLR sign signature, as illustrated in Figure 3.14 (a) and Figure 3.16 (a).

For the CA Z-Scan experiments at 505 nm, and in the intensity range of 17.54 to 105.3 GW/cm^2, the average NLR coefficient of pure toluene is $n_2^{505}(toluene) = +1.8 \times 10^{-15}$cm^2/W. For the CA Z-Scan experiments at 665 nm, and in an intensity range of 43.32 to 216.6 GW/cm^2, the average NLR coefficient of pure toluene is $n_2^{665}(toluene) = +1.3 \times 10^{-15}$cm^2/W. The valley-peak pattern for the toluene response is maintained for all intensity values and wavelengths.

CA Z-Scan signatures show the symmetric valley-peak pattern and the theoretical fits are accurately adjusted in Figure 3.16 (b) and (c). The intensity range used to perform the CA Z-Scan at 665 nm was 43.32 to 259.8 GW/cm^2 and the average NLR coefficients of $n_2 = +4.9 \times 10^{-15}$cm^2/W for 4 ML CdSe NPLs and $n_2 = +2.9 \times 10^{-15}$cm^2/W for CS sample. It can be concluded that the n_2 value of the 4 ML CdSe NPLs sample is approximately three times larger than that of the solvent and twice as large as the value for the CdSe/CdS CS sample. Notably, the valley-peak variations (ΔT_{v-p}^{665}) for the solvent and the 4 ML sample are of the same order of magnitude, indicating a positive sign of refractive nonlinearity (see Figure 3.16 (a) and (b)). The decrease in ΔT_{v-p}^{665} for the CS sample, shown in Figure 3.16 (c), is due to the smaller optical intensity applied compared to the other cases in Figure 3.16. Additionally, for the CS sample at 655 nm a SA behavior is also present contributing to the ΔT_{v-p}^{665} decreasing. When comparing the CdSe NPLs, it is expected that the 4 ML CdSe NPLs will exhibit a greater NLO response than the CdSe/CdS CS NPLs sample, attributed to the electron delocalization effect caused by the CdS shell, as previously discussed for the non-resonant case. It is important to note that the refractive effect at 665 nm for both toluene and the 4 ML CdSe NPLs in solution is solely intensity-dependent. This is because neither material exhibits absorptive mechanisms at this excitation wavelength, as illustrated in Figure 3.17 (a) and (b). This observation aligns with the absorbance spectra of these materials, which show no linear absorption around 600 nm. Consequently, the third-order susceptibility is purely refractive (real), as indicated by the relationship $\left|\chi^{(3)}\right|^2 = \left(\chi_R^{(3)}\right)^2 + \left(\chi_I^{(3)}\right)^2$, with $\chi_I^{(3)}$ equal to 0 in this case.

The observed valley-peak asymmetries in Figure 3.14 (b) and (c) for the CA Z-scan experiments at 505 nm can be explained by the results from OA studies shown in Figure 3.15 (b) and (c). These results indicate that the samples exhibit strong SA behavior at this

wavelength. The asymmetry in the CA Z-scan pattern, along with the poor fit quality across varying intensities, is attributed to the robust SA absorption, which dynamically alters the spatial beam profile near the focus. This is further coupled with third-order and possibly higher-order NLR. These factors lead to a breakdown of the standard perturbative Z-scan assumptions, necessitating the use of extended or numerical models to fully capture the NLO behavior.

The asymmetry observed in Figure 3.14 (c) is less pronounced than that in Figure 3.14 (b) because the CS NPLs are excited at wavelengths far from their exciton resonances. This results in fewer bound electron states, leading to weaker SA behavior compared to the case of 4 ML CdSe NPLs (as seen in Figure 3.15 (b) and (c)). The absorption feature near 505 nm in CdSe/CdS CS NPLs is a result of strain-induced modifications to the band structure and electron delocalization into the CdS shell. This phenomenon enables interfacial interactions and higher-energy transitions beyond the core excitonic states [72]. The mean NLR coefficient for 4 ML CdSe NPLs at 505 nm is approximately $n_2^{505}(4\ \boldsymbol{ML}) \approx +3.3 \times 10^{-14}$ cm²/W. However, this value may not be entirely accurate due to the reasons outlined above. Table 3.5 summarizes the NLR coefficients of the samples studied in both resonant and non-resonant regimes under femtosecond excitation at 800 nm. For the non-resonant case, the NLR coefficients obtained were an order of magnitude lower than those in the resonant regime, attributable to the virtual states compared to the real electronic states discussed here.

Table 3.5 – Obtained nonlinear coefficients from the studied materials at 505 nm, 665 nm, and 800 nm*.

Material	Wavelength (nm)					
	505			655		800
	n_2(cm²/W)	I_S(GW/cm²)	σ_S(cm²)	n_2(cm²/W)	I_S(GW/cm²)	n_2(cm²/W)
4 ML	$\sim +3.3 \times 10^{-14}$	1.15 ± 0.30	$\sim 2.3 \times 10^{-11}$	$+4.9 \times 10^{-15}$	---------	$+1.5 \times 10^{-16}$
CS	$\sim +5.9 \times 10^{-15}$	1.60 ± 0.20	---------	$+2.9 \times 10^{-15}$	2.9 ± 0.1	$+1.3 \times 10^{-16}$
Toluene	$+1.8 \times 10^{-15}$	---------	---------	$+1.3 \times 10^{-15}$	---------	$+1.4 \times 10^{-16}$

**NLR values in solution for the CdSe samples (effective values).*

Source: Gonçalves *et al*. (2023). Ref. [73].

As we discussed earlier, in the high-intensity regime, SA exceeds the capabilities of the third-order perturbative model. Therefore, it is necessary to employ an intensity-dependent non-perturbative method to study the SA mechanism observed in CdSe-based NPLs. During the one-photon resonant excitation OA Z-scan experiment, we observe an increase in transmittance

near the lens's focal point. This allows us to quantify the saturation intensity threshold of a material based on the OA Z-scan curves. The optical intensity losses in an SA medium within a thin sample, can be described by the following differential equation [74, 75]:

$$dI/dz' = -\alpha_j(I)I \tag{3.2}$$

where z' and I are the propagation distance and the optical intensity within the SA sample, respectively. $\alpha_j(I)$ is the intensity-dependent absorption coefficient and the index j states for a homogeneous medium ($j = 1$) or for an inhomogeneous broadened system ($j = 2$). The following equations provide for the SA coefficients as defined above [74 – 76]:

$$\alpha_1(I) = \alpha_0/(1 + I/I_S) \tag{3.3}$$

$$\alpha_2(I) = \alpha_0/\left(1 + \sqrt{I/I_S}\right), \tag{3.4}$$

where α_0 is the linear extinction coefficient, I is the excitation intensity, and I_S is the saturation intensity of the medium. I_S relates to the saturation cross-section (σ_S) of the medium by the relation $\sigma_S = \hbar\omega/2\tau I_S$ for a homogenous system; where $\hbar$ is the Planck's reduced constant, ω is the photon angular frequency, and τ is the lifetime of the excited-state population [77]. We can formally integrate equation (3.2) to calculate the output optical intensity, I_j^{out}, in the SA medium as follows [74, 75]:

$$I_j^{out} = I_j^{in} - \int_0^L \alpha_j(I)\, I dz', \tag{3.5}$$

where I_j^{in} is the optical intensity at the entrance face of the SA sample (in our case a 1 mm quartz cuvette containing the CdSe-based NPLs in toluene), L is the sample geometrical length. Based on equations (3.3) or (3.4) and considering the incoming laser pulses traveling in $+z$ direction as being spatially and temporally Gaussian profiles, it is possible to numerically solve equation (3.5). Considering I_S as a free parameter, we can determine the normalized instantaneous transmittance curves to fit the OA Z-scan experimental data as shown in Figure 3.15 (b) and (c), and Figure 3.17 (c).

The macroscopic average saturation intensities (I_S^{ave}) at 505 nm are $I_S^{ave} = 1.15 \pm 0.30$ GW/cm^2 for 4 ML CdSe NPLs and $I_S^{ave} = 1.60 \pm 0.20$ GW/cm^2 for CS NPLs for an intensity range of 17.63 to 140 GW/cm^2, as showed in Table 3.5. The CS sample exhibits a slightly higher I_S^{ave} value compared to the 4 ML CdSe NPLs. This is attributed to the lower linear absorption of CS NPLs at 505 nm (see Figure 3.6), resulting in a higher optical intensity to achieve the SA state as compared to 4 ML CdSe NPLs. In addition, the average excitonic HH state lifetime of our 4 ML CdSe NPLs sample is τ_{CdSe} ~ 1.0 ns [78, 79], which is in agreement with reported results [80, 81]. Therefore, the macroscopic HH excitonic transition cross-section

is $\sigma_S^{ave} \sim 2.3 \times 10^{-11}$ cm^2, which is 1000 greater than the value of individual 4 ML CdSe NPL cross-section [82]. This result is expected because our σ_S^{ave} value takes into account the number N of NPLs excited by the beam at the lens focal region during the scan. It is important to report the σ_S^{ave} values because the CdSe-based NPLs are in solution and a large number of NPLs are excited by the beam cross-section of the femtosecond laser pulse.

The I_S^{ave} values of the CS NPLs at 665 nm retrieved by the fitting curves in an excitation intensity range of 13.0 to 86.5 GW/cm^2 are $I_S^{ave} = 1.6 \pm 0.1$ GW/cm^2 ($j = 1$), and $I_S^{ave} = 2.9 \pm 0.1$ GW/cm^2 ($j = 2$). Figure 3.17 (c) shows that the red curve ($j = 2$) accurately represents the experimental data for the SA behavior of the CS sample, although with some slight deviation. However, the overall result suggests that when excited at one-photon resonance, the CS NPLs suspension exhibits characteristics of an inhomogeneous broadening system, which is consistent with the model described in equation (3.4). In addition, the HH average lifetime of CS NPLs in solution (τ_{CS}) gradually increases as the CdS shell grows on the CdSe NPLs core, resulting in τ_{CS}~13.0 ns [60]. This indicates that the macroscopic SA cross-section of colloidal CS NPLs decreases. As a result, the excitonic transition probability of HH states diminishes, which causes the CS NPLs system to reach the saturated absorptive state more slowly. This behavior is characteristic of inhomogeneously broadened systems [83]. Consequently, the I_S^{ave} value of CS NPLs must be increased to enhance the photon flux to reach a saturated steady state during resonant excitation. Furthermore, in an inhomogeneously broadened system like CS NPLs, not all absorbers resonate with the laser. This lack of resonance can occur due to local strain from the CdS shell over the CdSe core in each NPL, as well as variations in the orientations of the nanostructures within the volume being excited by the laser pulse.

3.6 Conclusion

We measured the NLO coefficients of CdSe and CdSe/CdS CS NPLs suspended in toluene by both Z-scan and OKG methods far from the materials excitonic transitions with femtosecond pulses. We found that the n_2 values for CdSe-based NPLs in suspension from both techniques are in excellent agreement, showing no dependence on the optical intensity. When the solvent contribution is subtracted, it is demonstrated that the CdSe NPLs exhibit a sign reversal in their third-order NLO response. Specifically, the CdSe/CdS CS NPLs show a predominantly negative response within the applied intensity range. This suggests that a higher-order susceptibility term is influencing the behavior of the system. In the non-resonant regime, our results showed that the macroscopic NLA coefficients of CdSe-based NPLs appear to be a nonlinear cascade fifth-order effect related to an effective 3PA, compatible with the refractive result. It means that, in the range of intensities employed, probably an instantaneous 2PA process occurs exciting electrons to the conduction band and, subsequently a third photon is absorbed (free carrier absorption) exciting the system to higher energy levels in the conducting band. Fang et al. have reported similar behavior under different experimental conditions [57]. Additionally, the presence of NPLs in suspension lowers the threshold for observing NLA compared to pure toluene.

The time response of the suspensions measured by OKG shows an orientational nonlinearity characterized by a tail with a picosecond response, following a fast femtosecond response that is limited by the duration of the laser pulse. The orientational dynamics of colloidal suspensions are crucial in determining their third-order NLO responses, as demonstrated by time-resolved OKG measurements. The 4 ML CdSe NPLs exhibit the fastest nonlinear response (0.7 ps), followed by the CdSe/CdS CS structures (1.0 ps), with pure toluene and CS_2 showing much slower decay times (3.2 ps and 2.0 ps, respectively). These findings emphasize the key role of nanostructure design – specifically, the presence and characteristics of a shell – in tuning the balance between electronic and orientational contributions to the ultrafast nonlinear optical response.

Under femtosecond pulse excitation resonant with heavy-hole (HH) excitonic transitions by using the Z-scan technique, both SA and third order NLR were investigated at two key wavelengths – 505 nm and 665 nm – corresponding to excitonic transitions in 4 ML CdSe NPLs and CS NPLs, respectively. The results reveal a pronounced SA behavior and positive NLR coefficients for both materials, indicating self-focusing nonlinearities. Notably,

the NLR coefficient of 4 ML CdSe NPLs at 505 nm reached $+3.3 \times 10^{-14}$ cm²/W, representing a significant enhancement – about two orders of magnitude – compared to non-resonant excitation conditions. This enhancement evidences the impact of resonant excitation near real electronic states, as opposed to virtual transitions observed in the non-resonant regime. It is important to note that the strong SA of 4 ML CdSe NPLs at 505 nm affects the refractive response. This situation requires additional treatment to combine the SA with Kerr-like refraction. Consequently, the Z-scan technique for characterizing the third-order nonlinearity may not provide a clear indication of pure third-order effects, leading to inaccuracies in the value of n_2 derived from this analysis.

The saturation intensities and SA cross-sections extracted from the open-aperture Z-scans further indicate that the CS NPLs system exhibits features of an inhomogeneously broadened medium, likely due to longer excitonic lifetimes induced by the CdS shell. The measured macroscopic excitonic cross-sections and higher saturation thresholds in CS NPLs support this behavior.

Overall, the significant resonant enhancement of third-order optical nonlinearities in these 2D systems confirms their potential for integration into ultrafast optical switching and photonic devices. This work not only enriches the understanding of the NLO behavior of 2D semiconductor NPLs but also provides a foundation for tuning these responses through nanostructure engineering.

In summary, the NLO response and the photophysical properties of CdSe NPLs in solution under non-resonant and resonant excitation regimes with femtosecond pulses have been studied and explained. Based on these results, potential applications of these nanomaterials can be envisioned. These findings resulted in two publications in prestigious peer-reviewed scientific journals, which can be found in APPENDICES I and II, respectively.

Additionally, another study on the femtosecond third-order nonlinear electronic responses of layered 2D $NbSe_2$, also conducted using the Z-scan method and the OKG technique. A briefly discussion about this work can be found in Chapter 5 and the result publication can be found in APPENDIX III.

4 NONLINEAR OPTICAL RESPONSES OF HALIDE PEROVSKITES QUANTUM DOTS: AN INITIAL ANALISES

In this chapter, we present the results on the nonlinear optical (NLO) refractive and absorptive properties of halide perovskite $CsPbBr_3$ cubic quantum dots in solution, particularly focusing on the far exciton resonance in the infrared femtosecond laser excitation regime. In addition to preliminarily investigating the NLR and NLA properties of these structures at a non-resonant wavelength of 800 nm, we utilize the measurements to validate the use of a digital camera for capturing the beam profile as a function of the sample position in a Z-scan setup. While this method is already established in the literature, we employ a novel approach to extract the transmittance curves.

This study was supported by a one-year Doctoral Sandwich Program (SWE) internship funded by the National Council for Scientific and Technological Development (CNPq, Brazil) under public call 14/2023. The internship was conducted at the Nano Institute of the Ludwing-Maximilian-Universität (LMU, Germany) in the Chair in Hybrids Nanosystems – Hybrids Nanophotonics, under the supervision of Prof. Dr. Leonardo de Souza Menezes, head of the ultrafast nanophotonics subgroup, which focuses on single nano-emitters and photon-phonon energy conversion.

The following sections will highlight the NLO properties of halide perovskites. We will then briefly describe the synthesis protocol, morphology, and optical characterization of the perovskite quantum dots (QDs) studied. Subsequently, we will present the simplified Z-scan setup used with a digital camera, detailing the post-processing of data obtained from a single scan capturing beam profiles at each sample position (z). Finally, we will show and discuss the preliminary NLR and NLA properties and mechanisms of the perovskite QDs in solution, concluding with perspectives for future analysis of various halide perovskite quantum-confined nanostructures, such as nanoplatelets.

4.1 Nonlinear Optical Properties and Applications of $CsPbBr_3$ Quantum Dots

All-inorganic cesium lead bromide ($CsPbBr_3$) QDs have rapidly emerged as front-runners among perovskite materials for advanced optoelectronic and photonic technologies. Their outstanding optical characteristics, including tunable bandgaps, high photoluminescence quantum yield, and excellent environmental stability, have made them ideal candidates for a wide range of devices such as light-emitting diodes (LEDs), lasers, and photodetectors. More recently, their NLO properties have attracted substantial interest due to the potential for applications in ultrafast optics, optical switching, and integrated photonic circuits.

$CsPbBr_3$ QDs synthesized via the ligand-assisted reprecipitation (LARP) method exhibit uniform cubical morphology with an average size of approximately 8 to 10 nm, as confirmed by transmission electron microscopy. These QDs possess a crystalline cubic phase and a direct bandgap of approximately 2.36 eV. Photoluminescence (PL) measurements reveal a narrow emission centered at 518 nm with a full-width at half-maximum (FWHM) of 21 nm, indicating a strong and pure green light emission. Their absorption spectrum spans from 400 to 650 nm, with a peak at around 508 nm, positioning them as efficient visible-light absorbers and emitters [84, 85].

Beyond these linear optical properties, $CsPbBr_3$ QDs demonstrate significant NLO behavior. Spectroscopic ellipsometry studies reveal a high refractive index of approximately 1.97 at 521 nm and an extinction coefficient of 0.12 at 510 nm, suggesting robust light–matter interaction and strong third-order nonlinear susceptibility ($\chi^{(3)}$) [84, 86]. The complex dielectric constants ($\varepsilon = \varepsilon_1 + i\varepsilon_2$) derived from ellipsometric data show prominent absorption edges and dispersion peaks in the visible and near-infrared regions. Specifically, the ε_1 values are reported as 3.7, 3.32, and 3.07 at 521 nm, 617 nm, and 973 nm, respectively, while ε_2 values of 0.74, 0.45, and 0.30 are observed at 507 nm, 575 nm, and 861 nm, respectively [84]. These optical constants underscore the capacity of $CsPbBr_3$ QDs to exhibit enhanced nonlinear interactions under high-intensity illumination.

The nonlinear response of these QDs arises from several intrinsic mechanisms. Quantum confinement in nanoscale $CsPbBr_3$ structures enhances exciton localization, thereby increasing oscillator strength and third-order nonlinearities. Their high exciton binding energies and low dielectric screening support the generation of strong multiphoton processes and inter-band transitions. Additionally, surface symmetry breaking and interface effects in nanostructured or layered assemblies can enable second-order processes such as second-

harmonic generation (SHG), which are typically forbidden in centrosymmetric bulk perovskites [87 – 89].

Empirical investigations have reported strong NLO responses in $CsPbBr_3$ under femtosecond laser excitation, including third-harmonic generation (THG), optical Kerr effect, and self-phase modulation, demonstrating ultrafast temporal dynamics suitable for applications in high-speed photonic systems [88]. Furthermore, symmetry engineering in quasi-two-dimensional or interface-structured $CsPbBr_3$ has enabled measurable SHG, opening new directions in nonlinear frequency conversion and electro-optic modulation [90]. These capabilities are supported by other studies that highlight the impact of film smoothness and interface design on enhancing the optical response in perovskite-based devices [87].

The strong NLO properties of $CsPbBr_3$ QDs make them highly promising materials for a broad range of applications. In optical limiting systems, they offer protection to sensors and human eyes by modulating transmission at high light intensities [91]. In all-optical switches and modulators, the intensity-dependent refractive index of $CsPbBr_3$ enables dynamic control of light without the need for electrical gating, which is vital for integrated photonic circuits. Their fast nonlinear response under pulsed excitation also supports their use in ultrafast signal processing devices [92]. Moreover, due to their strong multiphoton absorption and emission properties, $CsPbBr_3$ QDs are suitable for nonlinear bioimaging techniques such as two-photon microscopy, which allows deep-tissue imaging with reduced photodamage [93].

In summary, $CsPbBr_3$ QDs present a compelling combination of strong linear absorption, high refractive indices, and significant NLO susceptibility. These features position them as a versatile platform for next-generation photonic and optoelectronic applications, ranging from tunable lasers and light modulators to ultrafast switches and nonlinear bioimaging tools. The following section briefly describes the synthesis, morphology, and optical characterization of the perovskite QDs studied.

4.2 Synthesis, Optical Characterization, and Morphology

The $CsPbBr_3$ QDs were synthesized by Dr. Anna Abfalterer member of Prof. Alexander Urban's Nanospectroscopy Research group at the Nanoinsitut (LMU, Germany). Prof. Urban's group focuses on developing novel materials for renewable energy and efficient light generation in optoelectronic components. Dr. Abfalterer specializes in the synthesis, characterization, and optical spectroscopy of semiconductor nanocrystals, particularly perovskite nanocrystals.

$CsPbBr_3$ nanocrystals were synthesized following a modified hot-injection method under inert conditions using a Schlenk line. Cesium oleate was prepared by reacting Cs_2CO_3 with oleic acid in 1-octadecene (ODE) at 170 °C. Separately, $PbBr_2$ was dried in ODE at 100 °C under vacuum, followed by injection of dried oleylamine and oleic acid. After dissolution, the mixture was heated to 180 °C, and preheated cesium oleate was swiftly injected. After 15 seconds, the reaction was quenched using an ice-water bath. Nanocrystals were purified by centrifugation and toluene rinsing, then redispersed and combined into a single colloidal suspension. This synthesis procedure is similar as in *ACS Energy Lett.* 2019, 4, 1, 63–74 [94].

To assess the optical properties of $CsPbBr_3$ nanocrystals (labeled as AA111), UV-Vis absorption and photoluminescence (PL) spectra were recorded using a Horiba Fluoromax-Plus photospectrometer. An initial absorption measurement was conducted by diluting 50 µL of AA111 in 2950 µL of toluene. The absorbance at 390 nm was found to be 1.352, exceeding the recommended threshold (~0.1) for reliable optical measurements. To correct this, a second dilution was prepared using 3.7 µL of AA111 in 2996.3 µL of toluene, achieving an appropriate absorbance at 390 nm. Both absorbance and PL spectra were measured for this optimized sample. PL data were normalized to the maximum intensity value for comparative evaluation. Figure 4.1 shows the absorbance and PL spectra of the AA111 sample for a concentration corresponding to ~ 0.1 of absorbance at 390 nm of excitation. The NLO measurements were preformed using this sample in a 1 mm transparent quartz cuvette as in the figure. The insert exhibits the pure toluene spectra as a reference.

The $CsPbBr_3$ nanocrystals morphology and size was evaluated through transmission electron microscopy (TEM). One drop of the sample AA111 was dropcasted onto a TEM grid (Electron Microscopy Sciences, FCF200-Cu-50, Formvar/Carbon 200 Mesh, Copper, Lot 240812) under ambient conditions. The solvent was allowed to dry. TEM images were taken using a JEOL JEM-1011 transmission electron microscope with a tungsten filament operating at 80 kV. Figure 4.2 shows representative TEM images of the $CsPbBr_3$ nanocrystals. The

nanocrystals appear in cubic shape. A particle size analysis of the edge length of the nanocrystals was performed. The edge length of 300 nanocrystals was measured using the scientific image analysis software ImageJ, processing data from 13 TEM images. The average edge length was determined to be 9.2 nm ± 1.1 nm. The standard deviation (STD) was calculated using the formula: $STD = \sqrt{\sum_i (x_i - \bar{x})^2/(n-1)}$, where x_i is the edge length, x the average edge length, and $n = 300$. The smaller, dark dots appearing in the TEM images in Figure 4.2 are expected to be metallic Pb, caused by the electron beam irradiation as previously reported for similar $CsPbBr_3$ nanocrystals [95].

Figure 4.1 – Absorbance and PL spectra of the $CsPbBr_3$ nanocrystals. The PL maximum is at 511 nm, the photoluminescence full-width at half maximum is ~18 nm. Inset shows the toluene absorbance with the maximum near 275 nm.

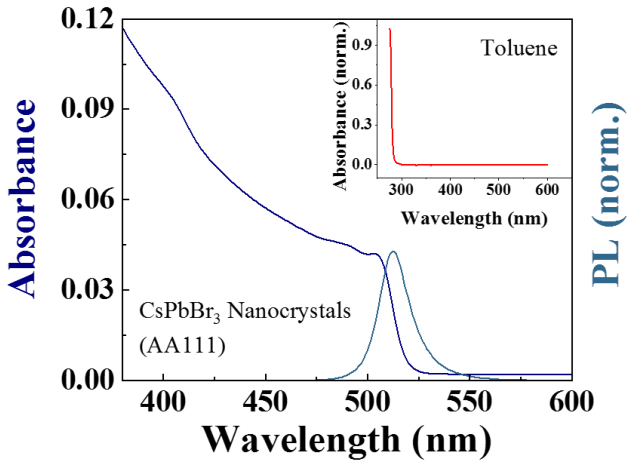

Source: The author (2025).

Figure 4.2 – TEM images of $CsPbBr_3$ nanocrystals for different magnifications.

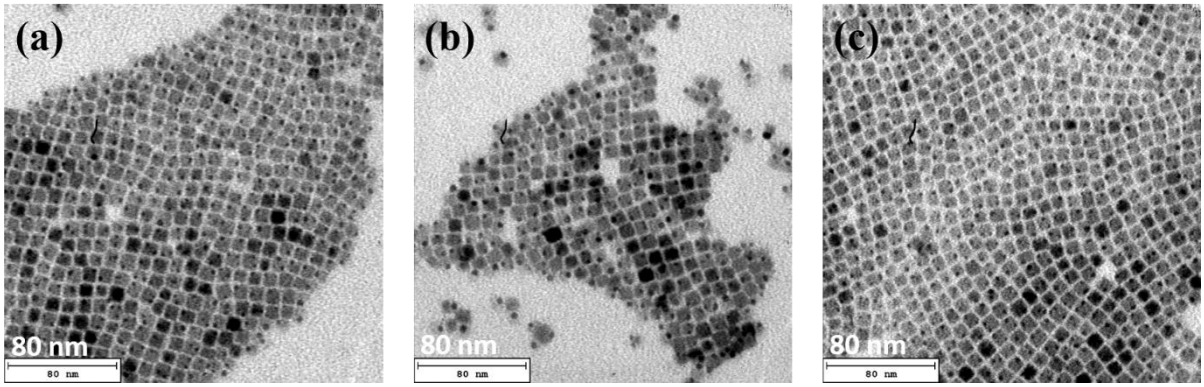

Source: The author (2025).

In the next section, we will describe the digital camera Z-scan setup and the methodology for extracting transmittance data from the beam's transversal images.

4.3 Digital Camera Z-scan Setup and Method

The digital camera Z-scan (DGZ-scan) setup closely resembles the standard Z-scan apparatus described in section 2.1.1. The key difference is the use of a single digital camera instead of photodetectors to capture the light transmitted through the sample during scans. This configuration offers advantages such as reduced physical space requirements and fewer optical components, eliminating the need for photodetectors, mirrors, and beam splitters for reference measurements. The digital camera used in our DGZ-scan was a Zelux 1.6 MP CMOS monochrome camera (Thorlabs, CS165MU(/M)), featuring 1440×1080 active pixels and an imaging area of 4.968×3.726 mm², with a pixel size of 3.45 μm $\times$ 3.45 μm.

In this setup, images of a Gaussian beam distorted by a nonlinear sample are captured by a single-shot CMOS camera as the sample position,*z*, varies. The OA and CA Z-scan normalized transmittance curves are numerically processed from the acquired images. This method allows for the simultaneous measurement of the nonlinear refractive index and the nonlinear absorption coefficient. The CMOS camera records the complete 2D transmitted beam profile at each *z*-position. By extracting both OA and CA data from the same set of images, this approach automatically eliminates the influence of fluctuations in laser pulse energy, removing the necessity for a simultaneous reference beam. Subsequently, the images are processed using a custom Matlab program that implements a 2D Z-scan algorithm to extract spatial and energetic metrics from each frame.

The OA response is computed as the total integrated intensity of each image as:

$$T_{OA}(z) = \sum \sum I(x, y, z)/T_0 \tag{4.1}$$

where, T_0 represents the reference transmission measured far from the focal region, while $I(x, y, z)$ denotes the spatial intensity distribution. The sums are taken over the x and y dimensions. This curve indicates the presence of nonlinear absorption and is utilized to determine the coefficient α_2, for instance. Figure 4.3 (a) illustrates a typical three-dimensional intensity distribution image that is used to compute $T_{OA}(z)$, as shown in equation (4.1).

To simulate an aperture, a centered square region of interest (e.g., 200×200 pixels) is extracted from each image. The intensity within this window is integrated to represent the amount of light passing through a virtual aperture placed at the center of the beam. This method allows retrieval of the CA signal directly from the CMOS data as:

$$T_{CA}(z) = \sum \sum I_{central}\,(x, y, z)/T_0. \tag{4.2}$$

The sums are also taken over the x and y dimension, and $I_{central}(x, y, z)$ is the spatial intensity distribution within the squared region as illustrated by Figure 4.3 (b) that shows the CA intensity distribution to compute $T_{CA}(z)$ as defined in equation (4.2). The ratio of $T_{CA}(z)$ to $T_{OA}(z)$ isolates the effect of nonlinear refraction independently of absorption as usual.

Figure 4.3 – Intensity distribution profiles for open aperture (a) and closed aperture (b) transmittance curves calculation.

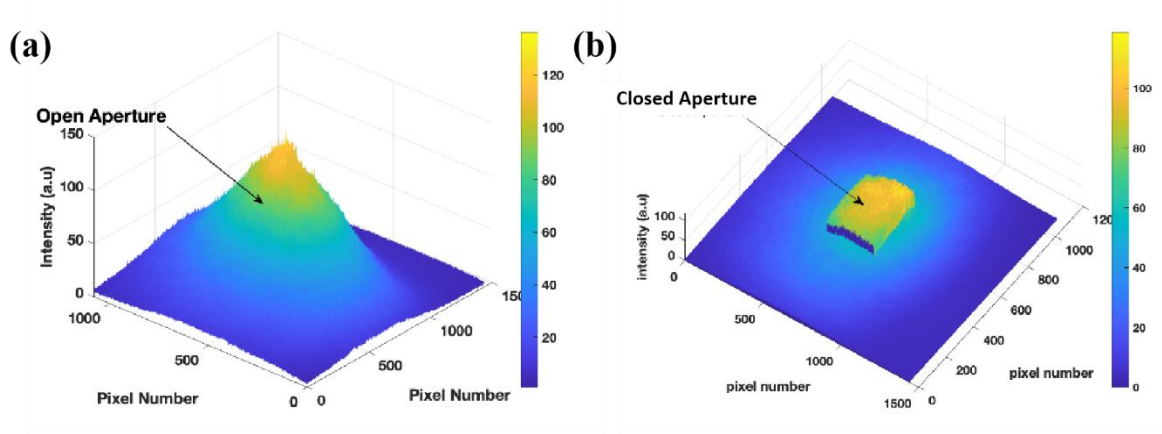

Source: The author (2025).

An additional and innovative quantity extracted from the CMOS data is the **beam width evolution**, calculated via the spatial second moment (variance) of the intensity distribution as:

$$\sigma^2(z) = \frac{\sum\sum((x - \bar{x})^2 + (y - \bar{y})^2) \cdot I(x,y,z)}{\sum\sum I(x,y,z)} \tag{4.3}$$

where $(\bar{x}, \bar{y})$ is the intensity-weighted centroid of the beam. This parameter provides a **direct and model-free measurement** of the beam's spatial expansion or contraction as a function of z. A local minimum in $\sigma(z)$ indicates beam self-focusing due to a positive n_2, while a maximum indicates self-defocusing (negative n_2). The ability to track the beam width in real space across z-positions, without relying on pinholes or scanning detectors, is a significant advantage of this CMOS-based 2D approach. This method also allows for the visualization of beam distortions or asymmetries that scalar OA/CA measurements alone might not capture.

4.4 Sub bandgap Nonlinear Measurements

In this section, we will present preliminary results of the NLR and NLA of $CsPbBr_3$ nanocrystals under 800 nm excitation. This wavelength is far from the one-photon excitation range of the perovskite nanocubes. The linear absorption spectra of both the perovskites and toluene are negligible near 800 nm, indicating that the effective length of interaction (L_{eff}) is approximately equal to the actual length (L) for both materials. The light source used for this experiment was a femtosecond laser source (PHAROS, Light Conversion) coupled with a collinear optical parametric amplifier (ORPHEUS, Light Conversion). The ORPHEUS produces femtosecond pulses that are tunable from ultraviolet (UV) to mid-infrared (MIR) wavelengths, with repetition rates of up to 2 MHz, making it an invaluable tool for ultrafast spectroscopy and nonlinear microscopy. PHAROS generates pulses with a temporal width of 175 fs and a repetition rate set to 1 kHz to prevent thermal buildup. The femtosecond pulses are focused at the focal point of a 15 mm lens, resulting in a beam waist of approximately 30 micrometers.

The choice of 800 nm excitation is significant because it corresponds to double the wavelength of the absorbance maximum near 400 nm (as shown in Figure 4.1), thus enabling multiphoton absorption. The strong absorption observed near 400 nm in $CsPbBr_3$ nanocrystals is primarily due to excitonic transitions at the band edge, which are enhanced by quantum confinement effects that increase both the exciton binding energy and the oscillator strength [84, 96].

4.4.1 Preliminary Results

Figure 4.4 (a) and (b) displays the representative CA transmittance curves for pure toluene in a 1 mm transparent quartz cuvette, illustrating low and high intensity regimes, respectively. Figure 4.4 (c) shows the NLR coefficient (n_2) as a function of peak intensity, ranging from 133 to 830 GW/cm², along with the n_2 mean value for toluene indicated by the red horizontal curve. This figure demonstrates that self-focusing behavior occurs in the solvent, resulting in a positive third-order nonlinearity. The mean NLR for pure toluene is calculated as $n_2 = +2.1 \times 10^{-16}$ cm²/W, following the established procedures. This value aligns with the result reported in Chapter 3 for a similar spectro-temporal regime.

Figure 4.4 – CA Z-scan curves of pure toluene. (a) Low intensity, (b) high, and (c) $n_2 \times I_0$ curve. In (a) and (b) the continuum lines are theoretical curves, while in (c) corresponds for the mean n_2 value.

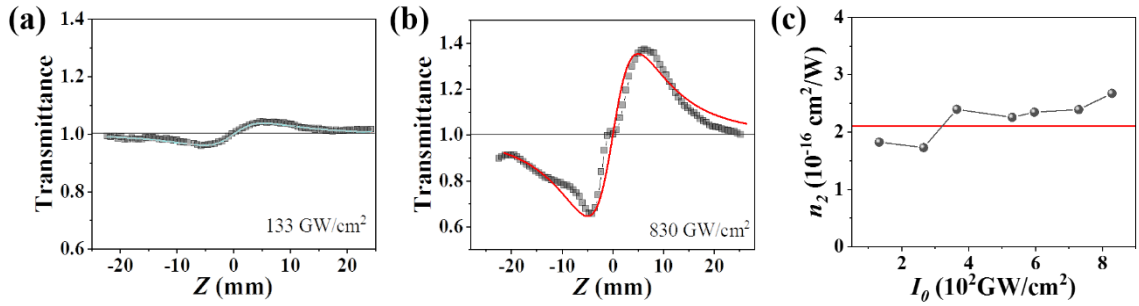

Source: The author (2025).

Figure 4.5 (a) and (b) present the CA Z-scan results for perovskite nanocrystals in solution. Figure 4.5 (c) illustrates the $n_2 \times I_0$ curve over an intensity range of 30 to 800 GW/cm², which is similar to the range used for the solvent. The CA Z-scan curves for the nanocrystals in toluene indicate a positive third-order NLR across the entire intensity range examined. Additionally, it is worth noting that, at approximately the same intensity level, the valley-to-peak separation in the transmittance curve of the nanocrystals in solution is smaller compared to that of the pure solvent (see Figures 4.4(b) and 4.5(b)). This suggests that the third-order nonlinearity of the perovskite nanocubes is likely negative. Another interesting trend can be observed in the results shown in Figure 4.5 (c): at an intensity of approximately 30 GW/cm², the effective nonlinear refractive index (n_2) for the nanocrystals is about six times greater than that of the solvent. As the intensity increases, this value approaches that of the solvent. This behavior will be discussed further later on.

Figure 4.5 - CA Z-scan curves of the $CsPbBr_3$ nanocrystals in solution. (a) Low intensity, (b) high, and (c) $n_2 \times I_0$ curve. In (a) and (b) the continuum lines are theoretical curves, while in (c) corresponds for the toluene mean value $n_2 = +2.1 \times 10^{-16}$ cm²/W.

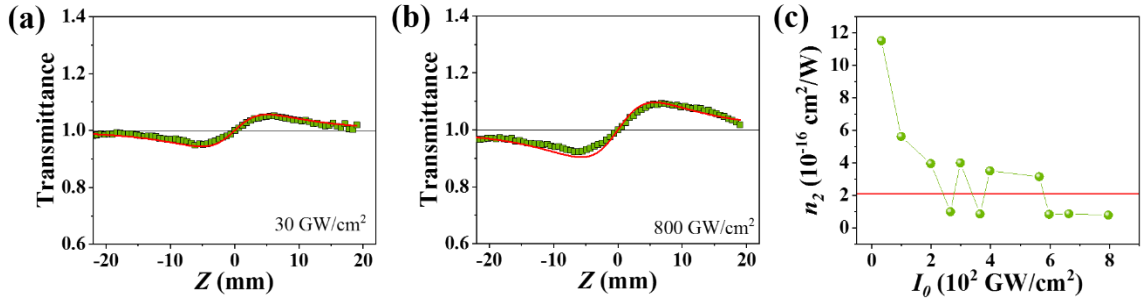

Source: The author (2025).

Figure 4.6 presents the representative open-aperture (OA) Z-scan curves for toluene and the QDs in solution. In Figure 4.6 (a), there is clear evidence of strong three-photon absorption

(3PA) in the solvent's response at very high intensities, suggesting that a fifth-order process is more likely to occur. The multiphoton absorption behavior of toluene was previously discussed in Chapter 3, referring to intensities of up to 1222 GW/cm². In Figure 4.6 (b), the OA curves for the perovskite QD solution demonstrate that a 3PA model fits the experimental data more accurately. The fitting procedure used is detailed in Section 3.4. It is important to note that the transmittance for the QDs in solution is considerably lower than that for the solvent, even at the same intensity levels (see Figure 4.6 (b)). This observation indicates that the 3PA mechanism becomes saturated in the solution due to the strong NLA effect of toluene. This finding aligns with the results from the refractive index investigation. The intensity range applied in the OA Z-scan experiments was 100 – 3000 GW/cm^2.

Figure 4.6 – OA Z-scan curves for toluene (a) and the perovskites QDs in solution (b). The continuum curves are the theoretical curves.

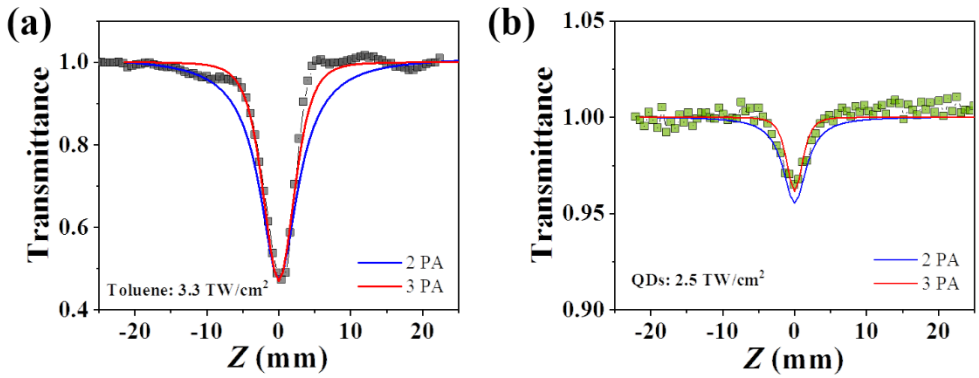

Source: The author (2025).

In the next section, we will discuss this prelaminar results presented here.

4.4.2 Discussion

At the highest intensity the CA transmittance curve for toluene exhibits a twisted bend in the near the focal point indicating that a higher order effect is play a role and no longer the third-order analysis satisfies the experimental CA data resulting in a poor fitting (see Figure 4.4 (b)). The result in Figure 4.4 (c) corroborates this statement once near 700 GW/cm^2 the n_2 values starts to deviates from the mean value and the curve $n_2 \times I_0$ appears to gain a positive slope evidencing that a higher order effect is present. The Z-scan CA experiments with $CsPbBr_3$ quantum dots in toluene reveal a higher n_2 value compared to the pure solvent at low intensities, attributed to strong Kerr-type excitonic effects (see Figure 4.5(c)). As the intensity increases, the overall refractive nonlinearity of the solution begins to resemble that of the solvent. This

behavior is consistent with the known high nonlinear response of toluene above 100 GW/cm², which ultimately dominates the solution's refractive behavior, as shown in Figure 4.5(c).

In our experiments with $CsPbBr_3$ QDs dispersed in toluene, using femtosecond pulses at 800 nm, the OA Z-scan measurements reveal that the 3PA in the QD solution is weaker than in pure toluene at similar intensity levels. While pure toluene exhibits strong, unsaturable 3PA due to nonresonant virtual transitions involving its wide electronic gap, the $CsPbBr_3$ quantum dots show a reduced 3PA response because of their discrete and confined electronic states. Under high excitation intensities, these quantum states undergo rapid state-filling, which limits the availability of transitions for further multiphoton absorption. Consequently, the NLA in the QD solution saturates, leading to a smaller transmittance decrease near the focus compared to pure toluene. Despite this saturation, some residual 3PA still occurs in the quantum dots. This behavior reflects the general trend that, in nanostructured systems with strong quantum confinement, multiphoton nonlinearities can diminish with increasing intensity due to the saturation of accessible energy states, while conventional solvents like toluene maintain a more robust and intensity-independent multiphoton absorption. It is important to note, however, that this represents an initial analysis. At high intensity regimes, other nonlinear optical effects such as strong self-focusing, filamentation, or possible thermal lensing can emerge in toluene, meaning that the observed transmittance curves may deviate from a purely three-photon absorption behavior.

4.5 Conclusion and Perspectives

In conclusion, the Z-scan results demonstrate that at high intensities, toluene exhibits higher-order NLO effects beyond third-order contributions, as evidenced by the twisted bending in the CA transmittance curve and the deviation of n_2 values near 700 GW/cm². For $CsPbBr_3$ QDs dispersed in toluene, a strong Kerr-type excitonic nonlinearity is observed at low intensities, resulting in a significantly higher n_2 compared to the solvent. However, as the excitation intensity increases, excitonic state filling appears to saturate the QDs' nonlinear response, causing the overall n_2 of the solution to converge toward that of pure toluene. This intensity-dependent behavior highlights the transition from exciton-dominated nonlinearities to solvent-dominated responses under strong optical fields, consistent with saturable refractive nonlinearity mechanisms typical in QDs under off-resonant femtosecond excitation.

In $CsPbBr_3$ QD solutions under femtosecond 800 nm excitation, 3PA occurs but is weaker than in pure toluene because the QDs' discrete energy levels saturate quickly at moderate intensities. Pure toluene, lacking saturable states, maintains strong 3PA. As a result, the QD solution exhibits less absorption near focus in OA Z-scan compared to the solvent.

The perspective is to investigate the NLO properties of the cubic QDs with approximately 10 nm edge length at the exciton resonance and at twice the exciton resonance wavelength to explore multiphoton absorption. The measurements were conducted duringthea stay at the Nano-institute (LMU, Germany). Our initial findings reveal saturable absorption at the exciton resonance and 2PA at twice the exciton absorption wavelength. Additionally, we performed similar measurements on QDs with a smaller edge length of around 3 nm, as well as on $CsPbBr_3$ nanoplatelets (NPLs) with three monolayers in toluene. This was done to investigate how the shape of these nanostructures affects their NLO responses. The size of the QDs and the number of layers in the NPLs can be tuned to adjust the exciton resonances of these structures, making them ideal for all-optical devices. The regime of intensity applied was low compared the study presented here to avoid the strong nonlinearities of toluene.

Another experiment is underway in the Physics Department of the Federal University of Pernambuco (UFPE, Brazil) to examine how these different shapes influence third-order polarization rotation nonlinearity using the Optical Kerr Gate (OKG) setup. We aim to assess the time responses under sub-bandgap excitation in the femtosecond domain. It is anticipated that the 3 ML NPLs of perovskites probably will exhibit a slower time response compared to the QD structures, due to the presence of an orientational nonlinearity effect.

5 FEMTOSECOND THIRD-ORDER ELECTRONIC NONLINEARITIES OF EXFOLIATED 2D $NbSe_2$

Although the primary focus of this thesis is on the third-order nonlinear optical properties of nanostructured semiconductors, this chapter presents a complementary study involving a distinct class of materials: two-dimensional metallic layered transition metal dichalcogenides (2D-LTMDs). Specifically, we report on the nonlinear optical characterization of metallic $NbSe_2$ in suspension, carried out using the same experimental techniques employed throughout this thesis – namely, the Z-scan and Optical Kerr Gate (OKG) methods. This work was conducted as part of a collaborative effort with research groups investigating the ultrafast optical responses of 2D materials, in which I participated as a co-investigator. The inclusion of this chapter serves both to document my contributions to this related study and to illustrate the broader applicability of the nonlinear optical techniques discussed in the core chapters of this thesis.

5.1 Two-dimensional layered transition metal dichalcogenides

Two-dimensional layered transition metal dichalcogenides (2D-LTMDs) have emerged as a versatile class of nanomaterials due to their tunable electronic structures and ease of fabrication. Unlike graphene, LTMDs exist in semiconducting, semimetallic, and metallic forms, enabling a wide range of photonic and optoelectronic applications [98]–[105]. Their strong light–matter interaction and atomic-layer thickness allow for enhanced NLO responses. Recent reviews [106]–[110] highlight that both second- and third-order nonlinearities have been observed in various LTMDs, including MoS_2, $MoTe_2$, WTe_2, NbS_2, and $NbSe_2$, using techniques such as second-harmonic generation, Z-scan, and the optical Kerr gate (OKG).

In particular, third-order nonlinearities – associated with the cubic susceptibility $\chi^{(3)}$ – enable functionalities such as self-focusing, two-photon absorption, optical limiting, and ultrafast switching. These properties are especially important for the development of ultrafast photonic devices. Prior studies by our group have characterized the NLO behavior of LTMD suspensions in liquids, showing that their responses span a wide temporal range – from milliseconds in thermally dominated regimes to sub-200 fs in the electronic regime.

The next section provides a comprehensive examination of the structural, electronic, and nonlinear optical characteristics of the metallic $NbSe_2$ nanoflakes explored in this work. These findings are supported by systematic experimental measurements, with additional datasets and methodological details available in published work in APPENDIX III for further reference.

5.2 Two-Dimensional Metallic $NbSe_2$

Among metallic LTMDs, $NbSe_2$ in its 2H trigonal prismatic phase stands out due to its room-temperature metallic behavior and superconductivity below 7 K [111, 112]. The flakes used in this study were obtained via redox exfoliation [111, 112], where polyoxometalates assist in delaminating the bulk structure. The exfoliated $NbSe_2$ flakes had lateral sizes of approximately 210 ± 128 nm and thicknesses of 4.1 ± 0.3 nm, suspended in acetonitrile (ACN).

Extensive morphological and compositional characterizations, including AFM, HRTEM, XPS, Raman, and UV-vis-NIR spectroscopy, confirmed the structure and purity of the suspension [111]. Figure 5.1 shows the absorbance spectra of $NbSe_2$ in ACN. While the spectrum lacks discrete excitonic peaks due to its metallic nature, it exhibits low linear absorption at 790 nm. Nevertheless, thermal nonlinearities may still arise under specific excitation regimes, necessitating careful control and interpretation of measurements [110].

Figure 5.1 – Absorbance spectra of the 2D metallic $NbSe_2$ in ACN suspension (red) and the pure ACN spectra (black). Notice that the pure ACN exhibits a deficient absorption.

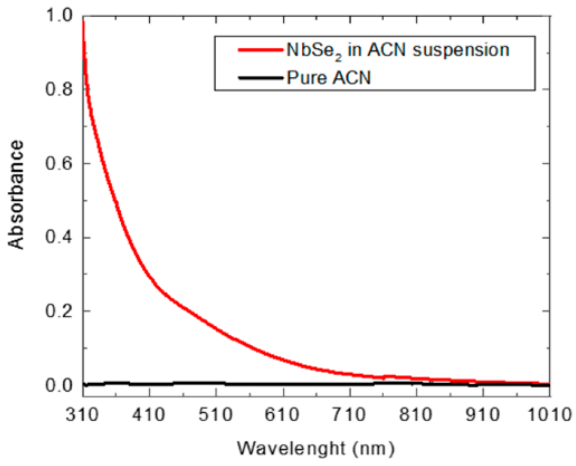

Source: Campos *et al*. (2024). Ref [61].

In the next section, we briefly discuss the experimental setups for the Z-scan and OKG methods – previously detailed in earlier chapters – used to evaluate the nonlinear optical properties of $NbSe_2$ nanoflakes.

5.3 Experiments: Z-scan and OKG

Using femtosecond laser pulses (190 fs, 790 nm, 750 Hz), we performed closed-aperture (CA) Z-scans to determine the nonlinear refractive index (n_2) and open-aperture (OA) Z-scans to measure nonlinear absorption (NLA). According to the apparatus scheme illustrated in Figure 3.7, the sample was translated along the beam's focal axis while monitoring transmittance changes. As discussed previously, low repetition rate pulses prevent cumulative heating, allowing us to probe purely electronic nonlinearities. Theoretical fitting of transmittance curves enabled the extraction of NLR and NLA coefficients, under the assumption of Gaussian spatial and temporal profiles, as ilucidated in prevoius chapters.

The OKG technique, shown in Figure 3.12, complements Z-scan by offering ultrafast temporal resolution. We used a Ti:sapphire mode-locked laser (185 fs, 800 nm, 76 MHz) to perform pump-probe measurements. The Kerr-induced birefringence rotated the polarization of the probe beam, which was detected using a polarization beam splitter and photodiode system. By scanning the pump-probe delay, we captured the temporal evolution of the nonlinear response. Using CS_2 as a reference material, we calibrated the system and calculated the magnitude of n_2 for $NbSe_2$ (see procedure in 3.4.2). As discussed, OKG is insensitive to thermal effects, as it relies on instantaneous polarization rotation rather than integrated thermal effects.

In the following section, we present the findings on the femtosecond electronic response of 2D $NbSe_2$ in CAN suspension, as characterized by Z-scan and OKG measurements.

5.4 Results and Discussion

Figure 5.2 presents CA and OA Z-scan results for intensities up to 300 GW/cm^2. The CA data show a positive peak–valley pattern, indicating a self-focusing nonlinearity. The OA scans reveal symmetric transmittance dips, characteristic of two-photon absorption (2PA). From these, we determined an average nonlinear refractive index of $n_2 = +(1.8 \pm 0.1) \times 10^{-15}$ cm^2/W and an absorption coefficient of $\alpha_2 = +(3.5 \pm 0.2) \times 10^{-2}$ cm/GW (Figure 5.3). Figure 5.4 shows the OKG signal for $NbSe_2$. A linear dependence between the OKG peak and pump intensity was observed, allowing us to retrieve $|n_2| = (4.2 \pm 0.5) \times 10^{-14}$ cm^2/W. The temporal width matched the laser pulse (170 fs), confirming an ultrafast electronic response. This fast behavior contrasts with the slower decay of ACN (1.66 ps) and CS_2 (1.82 ps).

Figure 5.2 – Experimental results (dots) and theoretical fits (red lines) from the Z-Scan method: (a) CA Z-Scan results at 70.2 GW/cm^2; (b) CA Z-Scan results at 210.4 GW/cm^2; (c) OA Z-Scan results at 70.2 GW/cm^2; (d) OA Z-Scan results at 140.3 GW/cm^2. The errors (bars for CA and shadows for OA) are the standard deviation of the mean for four successive transmittance measurements for each pump intensity.

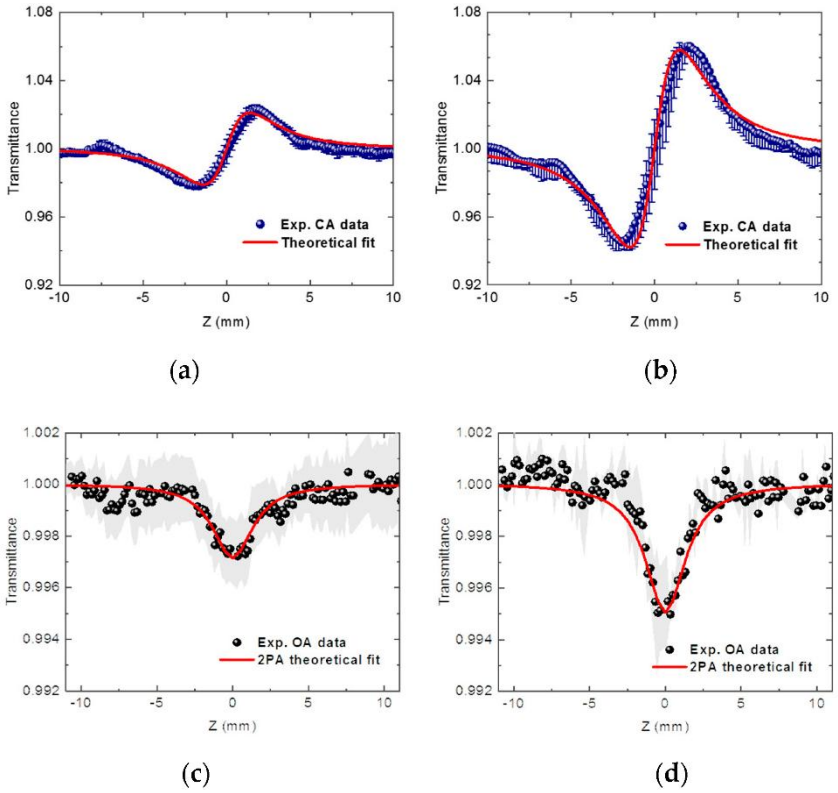

Source: Campos *et al*. (2024). Ref [61].

Comparative analysis (Table 5.1) shows that the $NbSe_2$ coefficients exceed those of the solvent and also surpass those of NbS_2 measured under similar conditions [114, 115]. Unlike NbS_2, no sign reversal or nonlinear scattering was observed, supporting a stable third-order

response. The occurrence of 2PA at high intensities is consistent with DFT-based electronic structure models, which predict transitions near 1.56 eV [116]. Van Hove singularities in the band structure likely contribute to this nonlinear behavior [117].

Figure 5.3 – NLR and NLA coefficients versus peak intensity at focus: (a) $n_2 \times I_0$ plot in the intensity range from ~30 to 270 GW/cm^2, exhibiting the average value (red line) of $n_2 = +(1.8 \pm 0.1) \times 10^{-15}$ cm^2/W; (b) $\alpha_2 \times I_0$ plot in the intensity range from ~50 to 140 GW/cm^2, showing a two-photon NLA coefficient of $\alpha_2 = +(3.5 \pm 0.2) \times 10^{-2}$ cm/GW.

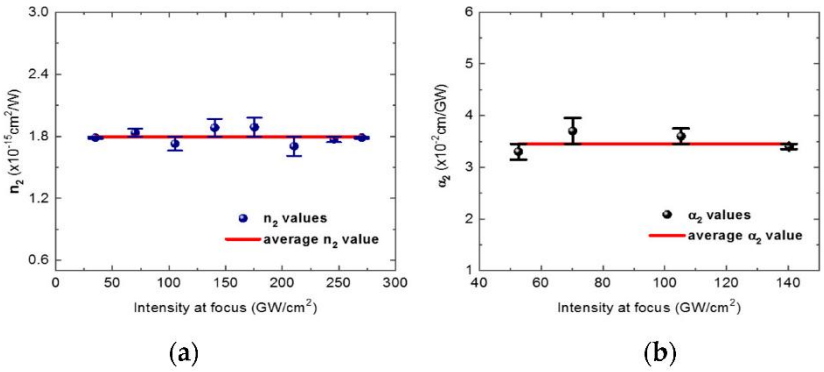

Source: Campos *et al*. (2024). Ref [61].

Figure 5.4 – OKG signal measured for $NbSe_2$ suspended in ACN. The inset is the maximum (peaks) OKG signal versus pump intensity. The error bars are the standard deviations of 10 successive measurements for each pump intensity.

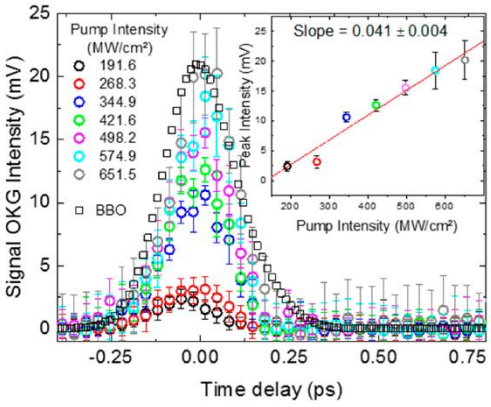

Source: Campos *et al*. (2024). Ref [61].

It is worth noting that the n_2 values extracted from the OKG measurements for $NbSe_2$ are at least one order of magnitude higher than those obtained from the Z-scan experiments. The higher n_2 value measured with OKG arises from its sensitivity to ultrafast Kerr-induced polarization changes under low-intensity, high-repetition-rate conditions, free from propagation distortions or thermal artifacts. In contrast, Z-scan measurements include nonlinear propagation effects and are performed at higher intensities, where saturation or multiphoton absorption

processes can reduce the effective n_2. This highlights the complementary nature of both techniques in capturing distinct aspects of the nonlinear refractive response.

Table 5.1 – Nonlinear optical coefficients for 2D metallic $NbSe_2$ and NbS_2 suspended in ACN obtained in the present work and related literature for similar spectro-temporal regimes.

Material	**Technique**	$\|n_2\|$**(cm²/W)**	α_2**(cm/GW)**	**Ref.**
$NbSe_2$	Z-Scan[a]	$(1.8 \pm 0.1) \times 10^{-15}$	$(3.5 \pm 0.4) \times 10^{-2}$	This work
	OKG[b]	$(4.2 \pm 0.5) \times 10^{-14}$	Not observed	
NbS_2	Z-Scan	$(3.0 \pm 0.2) \times 10^{-16}$	2.1×10^{-1}	[114]
	OKG	$(9.3 \pm 0.5) \times 10^{-15}$	Not observed	[115]
ACN	Z-Scan	1.9×10^{-17}	Negligible	[115]
CS_2	Z-Scan	$(3.1 \pm 1) \times 10^{-15}$	1.0×10^{-2}	[69]

[a]*790 nm, 190 fs, 750 Hz, 30-300 GW/cm²;* [b]*800 nm, 180 fs, 76 MHz, 200-600 MW/cm².*

Source: The author (2025).

5.5 Conclusion

In summary, this study has demonstrated that 2D metallic $NbSe_2$ suspended in acetonitrile exhibits strong and ultrafast third-order nonlinear optical responses under femtosecond excitation. Using both the Z-scan and OKG techniques, we quantified the nonlinear refractive index and two-photon absorption coefficients, revealing values significantly higher than those of the host solvent and even greater than those reported for similar LTMDs such as NbS_2. The nonlinear refractive index measured through OKG further confirmed the material's femtosecond-scale electronic response, underscoring its potential for ultrafast optical modulation.

These findings suggest that $NbSe_2$ is a promising candidate for various electro-optical applications. Its large and fast third-order nonlinearities can be exploited in the development of all-optical switches, ultrafast modulators, optical limiters, and signal processing devices. Additionally, the compatibility of $NbSe_2$ with solution processing makes it attractive for integration into flexible photonic circuits and layered heterostructures. As research into 2D materials continues to expand, metallic $NbSe_2$ stands out as a viable component for next-generation photonic and optoelectronic systems operating in the near-infrared region. For further details on this study, please, refer to APPENDIX III or reference [61].

REFERENCES

[1] M. SHEIK-BAHAE *et al.* Sensitive measurement of optical nonlinearities using a single beam. **IEEE Journal of Quantum Electronics**, 1 abr. 1990. v. 26, n. 4, p. 760–769.

[2] VAN STRYLAND, E. W.; SHEIK-BAHAE, M. "Z-scan measurements of optical nonlinearities," in *Characterization Techniques and Tabulations for Organic Nonlinear Optical Materials*, M. G. Kuzyk and C. W. Dirk, Eds. New York, NY, **USA: Marcel Dekker**, 1998, pp. 655–692.

[3] FRIBERG, S.; SMITH, P. Nonlinear optical glasses for ultrafast optical switches. **IEEE Journal of Quantum Electronics**, 1 dez. 1987. v. 23, n. 12, p. 2089–2094.

[4] PRASAD, P.; WILLIAMS, D. Introduction to Nonlinear Optical Effects in Molecules and Polymers. **Wiley-Interscience**. 1991.

[5] BOYD, R. W. Nonlinear Optics. **Academic Press**. 2020.

[6] AGRAWAL, G. P. Nonlinear absorption and ultrafast carrier dynamics in semiconductors. ***J. Opt. Soc. Am. B***, 1985. vol. 2, no. 3, pp. 480-488.

[7] GANEEV, R. A. Nonlinear optical properties of nanomaterials: Recent advances. **J. Nanophotonics**, 2011. vol. 5, no. 1, pp. 050303.

[8] XIA, T. *et al.* Eclipsing Z-scan measurement of $\lambda/10^4$ wave-front distortion. **Optics Letters**, 1 mar. 1994. v. 19, n. 5, p. 317.

[9] MARCANO, O. A.; MAILLOTTE, D. H.; Martel; ANDRAUD, C. Nonlinear optical properties of organic materials: From molecules to polymers. **J. Opt. Soc. Am. B**, dec. 2008. vol. 25, no. 12, pp. 1972–1982.

[10] VAN, E. W.; MANSOOR SHEIK-BAHAE. Z-scan technique for nonlinear materials characterization. **Proceedings of SPIE, the International Society for Optical Engineering/Proceedings of SPIE**, 30 jun. 1997. v. 10291, p. 102910Q102910Q.

[11] AGRAWAL, G. P. Nonlinear Fiber Optics. **Academic Press**. 2019.

[12] GASKILL, Jack D. Linear systems, Fourier transforms, and optics. Vol. 56. **John Wiley & Sons**, 1978.

[13] D. WEAIRE *et al.* Effect of low-power nonlinear refraction on laser-beam propagation in InSb. **Optics Letters**, 1 out. 1979. v. 4, n. 10, p. 331–331.

[14] HERMANN, J. A. Beam propagation and optical power limiting with nonlinear media. **Journal of the Optical Society of America B**, 1 out. 1984. v. 1, n. 5, p. 729.

[15] VAN STRYLAND, E. W. *et al.* Energy band-gap dependence of two-photon absorption. **Optics Letters**, 1 out. 1985. v. 10, n. 10, p. 490.

[16] VAN STRYLAND, E. W.; SHEIK-BAHAE, M. Z-Scan Technique for Nonlinear Materials Characterization. **CREOL**, The College of Optics and Photonics, University of Central Florida, 1998. [Online]. Available: https://api.creol.ucf.edu/Publications/933.pdf.

[17] GRINBLAT, G. *et al.* Ultrafast sub–30-fs all-optical switching based on gallium phosphide. **Science Advances**, jun. 2019. v. 5, n. 6.

[18] HE, G. S. *et al.* Multiphoton Absorbing Materials: Molecular Designs, Characterizations, and Applications. **Chemical Reviews**, 25 mar. 2008. v. 108, n. 4, p. 1245–1330.

[19] RAY, P. C. Size and Shape Dependent Second Order Nonlinear Optical Properties of Nanomaterials and Their Application in Biological and Chemical Sensing. **Chemical Reviews**, 14 maio. 2010. v. 110, n. 9, p. 5332–5365.

[20] SHAH, J. Ultrafast Spectroscopy of Semiconductors and Semiconductor Nanostructures. 2nd ed. Berlin, Germany: **Springer**, 1999.

[21] TREBINO, R. Frequency-Resolved Optical Gating: The Measurement of Ultrashort Laser Pulses. Boston, MA, USA: **Springer**, 2000.

[22] SHEN, Y. R. The Principles of Nonlinear Optics. **Wiley-Interscience**. 2003.

[23] KOCH, S. W. *et al.* Semiconductor excitons in new light. **Nature Materials**, 1 jul. 2006. v. 5, n. 7, p. 523–531.

[24] SALEH, B. E. A.; TEICH, M. C. Fundamentals of Photonics. **Wiley**. 2007.

[25] HELGE LEMMETYINEN *et al.* Time-resolved fluorescence methods (IUPAC Technical Report). **Pure and Applied Chemistry**, 28 nov. 2014. v. 86, n. 12, p. 1969–1998.

[26] YASUI, T. *et al.* Microscopic time-resolved two-dimensional imaging with a femtosecond amplifying optical Kerr gate. **Applied Optics**, 20 ago. 2002. v. 41, n. 24, p. 5191.

[27] YASUI, T.; MINOSHIMA, K.; MATSUMOTO, H. Three-dimensional shape measurement of a diffusing surface by use of a femtosecond amplifying optical Kerr gate. **Applied Optics**, 1 jan. 2000. v. 39, n. 1, p. 65.

[28] YAN, L. *et al.* Influence of self-diffraction effect on femtosecond pump-probe optical Kerr measurements. **Optics Express**, 28 jul. 2008. v. 16, n. 16, p. 12069.

[29] CARVALHO, A. J. A., *et al.* Near-infrared ultrafast third-order nonlinear optical response of 2D NbS_2, $NbSe_2$, $ZrTe_2$, and MoS_2. **Optics Letters**, 48.9 2023, 2297-2300.

[30] YU, J.; CHEN, R. Optical properties and applications of two-dimensional CdSe nanoplatelets. **InfoMat**, 7 abr. 2020. v. 2, n. 5, p. 905–927.

[31] STOCKMAN, M. I. Nanoplasmonics: The physics behind the applications. **Physics Today**, 1 fev. 2011. v. 64, n. 2, p. 39–44.

[32] GONÇALVES, I. M. *et al.* Nonlinear Optical Properties of 2D CdSe Nanoplatelets in a Nonresonant Regime. **The Journal of Physical Chemistry C**, 10 ago. 2023. v. 127, n. 33, p. 16679–16686.

[33] YASUHIRO SHIRASAKI *et al.* Emergence of colloidal quantum-dot light-emitting technologies. **Nature Photonics**, 27 dez. 2012. v. 7, n. 1, p. 13–23.

[34] EFROS, Al. L.; ROSEN, M. The Electronic Structure of Semiconductor Nanocrystals. **Annual Review of Materials Science**, ago. 2000. v. 30, n. 1, p. 475–521.

[35] HACHE, F.; RICARD, D.; C. FLYTZANIS. Optical nonlinearities of small metal particles: surface-mediated resonance and quantum size effects. **Journal of the Optical Society of America B**, 1 dez. 1986. v. 3, n. 12, p. 1647–1647.

[36] BRISTOW, A. D.; ROTENBERG, N.; DRIEL, H. M. VAN. Two-photon absorption and Kerr coefficients of silicon for 850–2200nm. **Applied Physics Letters**, 7 maio. 2007. v. 90, n. 19.

[37] STEGEMAN, G. I. cascading: nonlinear phase shifts. **Quantum and Semiclassical Optics: Journal of the European Optical Society Part B**, abr. 1997. v. 9, n. 2, p. 139–153.

[38] HAUG, H.; KOCH, S. W. Quantum Theory of the Optical and Electronic Properties of Semiconductors, 5th ed., **World Scientific**, 2009.

[39] CHERNIKOV, A. *et al.* Exciton Binding Energy and Nonhydrogenic Rydberg Series in Monolayer WS_2. **Physical Review Letters**, 13 ago. 2014. v. 113, n. 7.

[40] BASTARD, G. *Wave Mechanics Applied to Semiconductor Heterostructures*, **Les Ulis: Editions de Physique**, 1988.

[41] WOGGON, U. Optical Properties of Semiconductor Quantum Dots, **Springer**, 1997.

[42] MAK, K. F.; SHAN, J. Photonics and optoelectronics of 2D semiconductor transition metal dichalcogenides. **Nature Photonics**, 31 mar. 2016. v. 10, n. 4, p. 216–226.

[43] MILLER, A. Semiconductors. Dordrecht: **Nonlinear Optics in Signal Processing**, 1993. p. 66–99.

[44] WANG, H. *et al.* Synthesis, properties, and optoelectronic applications of two-dimensional MoS_2 and MoS_2-based heterostructures. **Chemical Society Reviews**, 1 jan. 2018. v. 47, n. 16, p. 6101–6127.

[45] MAK, K. F. *et al.* Atomically Thin MoS_2: A New Direct-Gap Semiconductor. **Physical Review Letters**, 24 set. 2010. v. 105, n. 13.

[46] YU, P. Y.; CARDONA, M. Fundamentals of Semiconductors. **SpringerLink**, 2023.

[47] ITHURRIA, S.; DUBERTRET, B. Quasi 2D Colloidal CdSe Platelets with Thicknesses Controlled at the Atomic Level. **Journal of the American Chemical Society**, 14 nov. 2008. v. 130, n. 49, p. 16504–16505.

[48] S. ITHURRIA *et al.* Colloidal nanoplatelets with two-dimensional electronic structure. **Nature Materials**, 23 out. 2011. v. 10, n. 12, p. 936–941.

[49] TESSIER, M. D. *et al.* Spectroscopy of Colloidal Semiconductor Core/Shell Nanoplatelets with High Quantum Yield. **Nano Letters**, 13 jun. 2013. v. 13, n. 7, p. 3321–3328.

[50] BIADALA, L. *et al.* Recombination Dynamics of Band Edge Excitons in Quasi-Two-Dimensional CdSe Nanoplatelets. **Nano Letters**, 21 fev. 2014. v. 14, n. 3, p. 1134–1139.

[51] YELTIK, A. *et al.* Experimental Determination of the Absorption Cross-Section and Molar Extinction Coefficient of Colloidal CdSe Nanoplatelets. **The Journal of Physical Chemistry C**, 16 nov. 2015. v. 119, n. 47, p. 26768–26775.

[52] ACHTSTEIN, A. W. *et al.* Electronic Structure and Exciton–Phonon Interaction in Two-Dimensional Colloidal CdSe Nanosheets. **Nano Letters**, 24 maio. 2012. v. 12, n. 6, p. 3151–3157.

[53] GRIM, J. Q. *et al.* Continuous-wave bi-exciton lasing at room temperature using solution-processed quantum wells. **Nature Nanotechnology**, 5 out. 2014. v. 9, n. 11, p. 891–895.

[54] TESSIER, M. D. *et al.* Efficient Exciton Concentrators Built from Colloidal Core/Crown CdSe/CdS Semiconductor Nanoplatelets. **Nano Letters**, 11 dez. 2013. v. 14, n. 1, p. 207–213.

[55] MAHLER, B. *et al.* Towards non-blinking colloidal quantum dots. **Nature Materials**, 22 jun. 2008. v. 7, n. 8, p. 659–664.

[56] SHE, C. *et al.* Low-Threshold Stimulated Emission Using Colloidal Quantum Wells. **Nano Letters**, 28 abr. 2014. v. 14, n. 5, p. 2772–2777.

[57] FANG, L.-B. *et al.* Nonresonant and Resonant Nonlinear Absorption of CdSe-Based Nanoplatelets. **Chinese Physics Letters**, 1 ago. 2017. v. 34, n. 9, p. 098101–098101.

[58] D'AMATO, M. *et al.* Room-Temperature Efficient Single-Photon Generation from CdSe/ZnS Nanoplatelets. **ACS Nano**, 1 abr. 2025.

[59] DUTTA, A.; MEDDA, A.; BERA, R.; SARKAR, K.; SAIN, S.; KUMAR, P.; PATRA, A. Hybrid Nanostructures of 2D CdSe Nanoplatelets for High-Performance Photodetector Using Charge Transfer Process. **ACS Appl. Nano Mater**. 2020, *3*, 4717–4727.

[60] DUTTA, A.; MEDDA, A.; GHOSH, S.; SAIN, S.; PATRA, A. 2D CdSe/CdS Core–Shell Nanoplatelets for High-Performance Photodetectors. **ACS Appl. Nano Mater**. 2022, *5*, 11679–11688.

[61] CAMPOS, C. L. A. V. *et al.* Femtosecond Third-Order Nonlinear Electronic Responses of 2D Metallic $NbSe_2$. **Photonics**, 30 set. 2024. v. 11, n. 10, p. 930.

[62] TALAPIN, D. V. *et al.* Prospects of Colloidal Nanocrystals for Electronic and Optoelectronic Applications. **Chemical Reviews**, 3 dez. 2009. v. 110, n. 1, p. 389–458.

[63] DNEPROVSKII, V. *et al.* Nonlinear absorption and refraction of CdSe/ZnS quantum dots at two-photon resonant excitation of excitons. **physica status solidi c**, 20 maio. 2008. v. 5, n. 7, p. 2507–2510.

[64] NAWROT, K. C. *et al.* Spectrally Resolved Nonlinear Optical Properties of Doped *Versus* Undoped Quasi-2D Semiconductor Nanocrystals: Copper and Silver Doping Provokes Strong Nonlinearity in Colloidal CdSe Nanoplatelets. **ACS Photonics**, 4 jan. 2022. v. 9, n. 1, p. 256–267.

[65] PLATT, J. R. Classification of Spectra of Cata-Condensed Hydrocarbons. **The Journal of Chemical Physics**, 1 maio. 1949. v. 17, n. 5, p. 484–495.

[66] M. SHEIK-BAHAE *et al.* Dispersion of bound electron nonlinear refraction in solids. **IEEE Journal of Quantum Electronics**, 1 jun. 1991. v. 27, n. 6, p. 1296–1309.

[67] PANKOVE, J. I. Optical Processes in Semiconductors, 2nd ed.; **Dover Publications**: Mineola, NY, 2003, 34−81.

[68] SHORNIKOVA, E. V. *et al.* Exciton Binding Energy in CdSe Nanoplatelets Measured by One- and Two-Photon Absorption. **Nano Letters**, 7 dez. 2021. v. 21, n. 24, p. 10525–10531.

[69] COURIS, S. *et al.* An experimental investigation of the nonlinear refractive index (n_2) of carbon disulfide and toluene by spectral shearing interferometry and z-scan techniques. **Chemical Physics Letters**, fev. 2003. v. 369, n. 3-4, p. 318–324.

[70] IPPEN, E. P.; SHANK, C. V. Picosecond Response of a High−repetition−rate CS_2 Optical Kerr Gate. **Appl. Phys. Lett**. 1975, 26, 92−93.

[71] KALPOUZOS, C.; LOTSHAW, W. T.; Mc MORROW, D.; KENNEY-WALLACE, G. A. Femtosecond Laser-Induced Kerr Responses in Liquid Carbon Disulfide. J. Phys. Chem. A 1987, 91, 2028−2030.

[72] JORDI LLUSAR; JOSEP PLANELLES; CLIMENTE, J. I. Strain in Lattice-Mismatched CdSe-Based Core/Shell Nanoplatelets. **The Journal of Physical Chemistry C**, 5 ago. 2019. v. 123, n. 34, p. 21299–21306.

[73] GONÇALVES, I. M. *et al.* Saturable absorption and third-order nonlinear refraction of 2D CdSe nanoplatelets resonant with heavy-hole excitonic transitions. **Applied Physics Letters**, 18 dez. 2023. v. 123, n. 25.

[74] GU, B. *et al.* Characterization of saturable absorbers using an open-aperture Gaussian-beam Z-scan. **Physical Review A**, 5 jun. 2006. v. 73, n. 6.

[75] GU, B. *et al.* Z-scan theory of two-photon absorption saturation and experimental evidence. **Journal of Applied Physics**, 15 out. 2007. v. 102, n. 8.

[76] SAMOC, M. *et al.* Saturable absorption in poly(indenofluorene): a picket-fence polymer. **Optics Letters**, 15 ago. 1998. v. 23, n. 16, p. 1295.

[77] SWARTZLANDER, G. A.; YIN, H.; KAPLAN, A. E. Continuous-wave self-deflection effect in sodium vapor. **Journal of the Optical Society of America B**, 1 jul. 1989. v. 6, n. 7, p. 1317–1317.

[78] DUTTA, A. *et al.* Hybrid Nanostructures of 2D CdSe Nanoplatelets for High-Performance Photodetector Using Charge Transfer Process. **ACS Applied Nano Materials**, 22 abr. 2020. v. 3, n. 5, p. 4717–4727.

[79] DAS, S. *et al.* Ultrafast carrier dynamics in 2D–2D hybrid structures of functionalized GO and CdSe nanoplatelets. **Physical Chemistry Chemical Physics**, 2019. v. 21, n. 28, p. 15568–15575.

[80] PIETER GEIREGAT *et al.* Localization-limited exciton oscillator strength in colloidal CdSe nanoplatelets revealed by the optically induced stark effect. **Light Science & Applications**, 31 maio. 2021. v. 10, n. 1.

[81] MORGAN, D. P.; KELLEY, D. F. Exciton Localization and Radiative Lifetimes in CdSe Nanoplatelets. **The Journal of Physical Chemistry C**, 9 jul. 2019. v. 123, n. 30, p. 18665–18675.

[82] AYDAN YELTIK *et al.* Experimental Determination of the Absorption Cross-Section and Molar Extinction Coefficient of Colloidal CdSe Nanoplatelets. **The Journal of Physical Chemistry C**, 6 nov. 2015. v. 119, n. 47, p. 26768–26775.

[83] YARIV, A.; YEH, P. Photonics: Optical Electronics in Modern Communications, 6th ed. **Oxford University Press**, 2007.

[84] AHIRWAR, P. *et al.* Structural and optical analysis of all inorganic $CsPbBr_3$ perovskite quantum dot thin film on glass substrate. **Materials Today: Proceedings**, 2023. [Online]. Available: https://doi.org/10.1016/j.matpr.2024.01.041.

[85] PROTESESCU, L. *et al.* Nanocrystals of cesium lead halide perovskites ($CsPbX_3$, X = Cl, Br, and I): novel optoelectronic materials showing bright emission with wide color gamut. **Nano Lett.** 2015. vol. 15, no. 6, pp. 3692–3696.

[86] ZHAO, M. *et al.* Ellipsometric study of the complex optical constants of a $CsPbBr_3$ perovskite thin film. **J. Mater. Chem. C**, 2018, vol. 6, pp. 10450–10455.

[87] ZHANG, T. *et al.* Second harmonic generation in 2D perovskites: symmetry breaking and interface effects. **Adv. Optical Mater.**, 2020, vol. 8, no. 12, p. 2000043.

[88] YAN, W. *et al.* Determination of complex optical constants and photovoltaic device design of all-inorganic $CsPbBr_3$ perovskite thin films. **Opt. Express**, 2020, vol. 28, pp. 15706–15717.

[89] WANG, R. *et al.* Ultrafast nonlinear optical response of all-inorganic perovskite nanocrystals. **ACS Appl. Nano Mater.**, 2020, vol. 3, no. 3, pp. 2867–2875.

[90] LU, H. *et al.* Efficient second-harmonic generation in quasi-2D perovskite nanocrystals. **Nano Lett.**, 2020, vol. 20, no. 6, pp. 4474–4480.

[91] CHEN, X. *et al.* Temperature dependent reflectance and ellipsometry studies on a $CsPbBr_3$ single crystal. **J. Phys. Chem. C**, 2019, vol. 123, pp. 10564–10570.

[92] DEY, K. *et al.* Nonlinear optical limiting behavior of $CsPbBr_3$ nanocrystals under nanosecond excitation. **Opt. Mater.**, 2020, vol. 107, p. 110122.

[93] WANG, Y. *et al.* Ultrafast carrier dynamics and optical nonlinearity in $CsPbBr_3$ nanocrystals. **J. Phys. Chem. Lett.**, 2018, vol. 9, no. 18, pp. 5296–5302.

[94] ZENG, H. *et al.* Multiphoton imaging with perovskite quantum dots. **ACS Nano**, 2017, vol. 11, no. 5, pp. 4533–4542.

[95] KANDADA, A. R. S.; PETROZZA, A. Colloidal $CsPbBr_3$ Perovskite Nanocrystals: Synthesis, Photophysics, and Applications. **ACS Energy Lett.**, 2019, vol. 4, no. 1, pp. 63–74.

[96] DANG, Z. *et al. In Situ.* Transmission Electron Microscopy Study of Electron Beam-Induced Transformations in Colloidal Cesium Lead Halide Perovskite Nanocrystals. **ACS Nano**, 25 jan. 2017. v. 11, n. 2, p. 2124–2132.

[97] ZHANG, D. *et al.* Synthesis of Composition Tunable and Highly Luminescent Cesium Lead Halide Nanowires through Anion-Exchange Reactions. **Journal of the American Chemical Society**, 6 jun. 2016. v. 138, n. 23, p. 7236–7239.

[98] ALAM, S. *et al.* Synthesis of emerging two-dimensional (2D) materials – Advances, challenges and prospects. **FlatChem**, nov. 2021. v. 30, p. 100305.

[99] SONG, L. *et al.* Recent Advances of Preparation and Application of Two-Dimension van der Waals Heterostructure. **Coatings**, 9 ago. 2022. v. 12, n. 8, p. 1152–1152.

[100] LEI, Y. *et al.* Graphene and Beyond: Recent Advances in Two-Dimensional Materials Synthesis, Properties, and Devices. **ACS Nanoscience Au**, 16 set. 2022. v. 2, n. 6, p. 450–485.

[101] HAN, S.A. *et al.* Synthesis, Properties and Potential Applications of 2D TMDs. **Nano Converg**., vol. 2, 2015.

[102] YIN, P. *et al.* 2D Materials for Nonlinear Photonics. **Adv. Mater. Interfaces**, vol. 8, 2021.

[103] JOSEPH, S. *et al.* Review of 2D TMDs and Heterostructures. **Mater. Chem. Phys.**, vol. 297, 2023.

[104] MCCREARY, A. *et al.* 2D Materials Beyond Graphene. **2D Mater.**, vol. 8, 2021.

[105] VERMEULEN, N. *et al.* Post-2000 nonlinear optical materials and measurements: data tables and best practices. **Journal of Physics Photonics**, 1 nov. 2022. v. 5, n. 3, p. 035001–035001.

[106] AUTERE, A. *et al.* Nonlinear Optics with 2D Layered Materials. **Advanced Materials**, 25 mar. 2018. v. 30, n. 24.

[107] HAN, B. *et al.* Deep-Learning-Enabled Fast Optical Identification and Characterization of 2D Materials. **Advanced Materials**, 9 jun. 2020. v. 32, n. 29.

[108] AHMED, S. *et al.* Recent Advances in Nonlinear Photonics of 2D Materials. **Adv. Opt. Mater.**, vol. 9, 2021.

[109] GOMES, A. S. L. *et al.* Intensity-Dependent Optical Response of 2D LTMDs Suspensions: From Thermal to Electronic Nonlinearities. **Nanomaterials**, 7 ago. 2023. v. 13, n. 15, p. 2267.

[110] SILVA-GUILLÉN, J.Á. *et al.* Electronic Structure of $NbSe_2$. **2D Mater.**, vol. 3, 2016.

[111] UGEDA, M. M. *et al.* Characterization of collective ground states in single-layer NbSe2. **Nature Physics**, 2 nov. 2015. v. 12, n. 1, p. 92–97.

[112] JAWAID, A. M.; RITTER, A. J.; VAIA, R. A. Mechanism for Redox Exfoliation of Layered Transition Metal Dichalcogenides. **Chemistry of Materials**, 13 jul. 2020. v. 32, n. 15, p. 6550–6565.

[113] JAWAID, A. M.; RITTER, A. J.; VAIA, R. A. Mechanism for Redox Exfoliation of Layered Transition Metal Dichalcogenides. **Chemistry of Materials**, 13 jul. 2020. v. 32, n. 15, p. 6550–6565.

[114] BAUTISTA, J.E. *et al.* Thermally Induced NLO Response of 2D LTMDs. **ACS Photonics**, vol. 10, 2023.

[115] MALDONADO, M. *et al.* Femtosecond Nonlinear Optical Properties of NbS_2. **J. Phys. Chem. C**, vol. 124, 2020.

[116] SILVA-GUILLÉN, J.Á. *et al.* Electronic Structure of $NbSe_2$ in CDW State. **2D Mater.**, vol. 3, 2016.

[117] VAN LOON, E.G. *et al.* Coulomb and Electron-Phonon Interactions in NbS_2. **Quantum Mater.**, vol. 3, 2018.

APPENDIX A: FUNDAMENTALS OF NONLINEAR OPTICS

In general, the average amount of energy of a propagating electromagnetic field spread in space per unit of time is directly proportional to the intensity of this field, and for nonmagnetic mediums it's directly related to the electric field component magnitude, E. In this way, E determines how strong the intensity of the field is. For example, in the visible electromagnetic spectrum region (typically between 380 to 700 nm of wavelength), E vary widely depending on the light source used and its intensity (power per unit area). As an example, for the sunlight at the Earth's surface the irradiance is about 10^3 W/m^2 [1,2] (considering atmospheric absorption and scattering) corresponding to $E \approx 869$ V/m[1]. Thus, these typical values characterize what is defined as the *linear regime* of light-matter interaction, which is responsible for some phenomena such as dispersion, reflection, refraction, scattering and so on. Moreover, when a high-intensity electromagnetic radiation field (typically of the order of 10^9 W/m^2 or higher) interacts with matter, numerous new phenomena starts to appear. These phenomena depends on the wavelength of the incident radiation, the intensity magnitude, and on the material's geometrical and structural properties. This high-intensity regime characterizes the *nonlinear regime*, leading to effects such as harmonic generation, multiphoton absorption, and self-focusing.

Herein we will discuss the fundamentals of nonlinear optical regime, beginning with an understanding of the linear regime and examining the origins of some fundamental linear phenomena such as reflection, refraction, absorption, transmission, and scattering. By introducing nonlinear terms in the polarization vector of the material, we can develop the theory to explore the multitude of new phenomena that emerge when the incoming electromagnetic radiation has high intensity. We will examine phenomena that depends on the second- and/or third-order nonlinear terms in the material polarization vector, such as, parametric second-order effects and nonlinear absorption and nonlinear refraction.

[1] To estimate E one can use the follow relation: $E = (2I/c\epsilon_0)^{1/2} \approx 869$ V/m, where, I is the average intensity, c ($\approx 3 \times 10^8$m/s) is the speed of light in a vacuum, and ϵ_0 ($\approx 8.85 \times 10^{-12}$F/m) is the electric permittivity of free space.

A.1 Light-Matter Interaction: Linear Regime

In this section we will discuss light-matter interaction in the low intensity regime where the light polarization vector, $\boldsymbol{P}$, varies linearly with the electric field vector component $\boldsymbol{E}$. This dependence gives rise to fundamental phenomena such as reflection, refraction, transmission, absorption, and scattering. To gain a deeper understanding of these phenomena, we will develop the theoretical framework and present detailed phenomenological discussions. We will examine how these interactions govern the behavior of light as it interacts with matter, leading to a comprehensive understanding of the linear optical regime and its implications in various applications.

A.1.1 Liner Polarization

When an external electric field $\boldsymbol{E}$ is applied to a material, the charges within the atoms and molecules shift slightly, leading to the formation of electric dipoles. The polarization vector, $\boldsymbol{P}$, mathematically describes the collective effect of these small dipoles within the material. In the linear regime (i.e., when $\boldsymbol{E}$ is not too strong compared to the internal electric fields binding the charges in atoms and molecules) $\boldsymbol{P}$ is directly proportional to the external electric field applied, and this relation can be expressed by the follow equation:

$$\boldsymbol{P} = \epsilon_0 \chi^{(1)} \boldsymbol{E}, \tag{A.1}$$

where, ϵ_0 is the permittivity of free space and $\chi^{(1)}$ is the *linear* susceptibility of the material. $\chi^{(1)}$ is a dimensionless constant that characterizes the material's response to $\boldsymbol{E}$, depending on its microscopic structure and external conditions like temperature. Moreover, there exists a class of dielectric materials in nature that possess a spontaneous electric polarization even in the absence of an external electric field. These dielectrics are known as *ferroelectric* materials, and their permanent polarization arises from the non-centrosymmetric arrangement of atoms within their crystal lattice [3]. Examples of ferroelectric materials are the Barium Titanate ($BaTiO_3$) [4] and the Lead Zirconate Titanate (PZT), widely used in sensors, actuators and memory devices [5]. In the case when an external electric field $\boldsymbol{E}$ is applied on a ferroelectric material, and its spontaneous polarization contribution $\boldsymbol{P_0}$ has significant magnitude as compared with the material's linear response due to $\chi^{(1)}$, the material total polarization is expressed as:

$$\boldsymbol{P} = \boldsymbol{P_0} + \epsilon_0 \chi^{(1)} \boldsymbol{E}. \tag{A.2}$$

It is worth mentioning that there are other polarization origins that do not depend on an external electric field to appear. In *piezoelectric* materials, an electric polarization response is generated due to a mechanical stress, typically linear concerning the applied mechanical force [5, 6].

In the next section, we will begin the analysis of several fundamental optical phenomena resulting from the linear polarization of a material. Specifically, we will apply equation (A.1) to a monochromatic electromagnetic wave in a low-intensity regime to describe its propagation through the material and at its boundaries. Section A.1.2 will focus on elucidating the theoretical and phenomenological aspects of two key optical phenomena that occur when an electromagnetic wave interacts with the boundary between two media: reflection and refraction.

A.1.2 Reflection and Refraction

Reflection and refraction are fundamental phenomena governed by linear optics. When an electromagnetic (EM) wave meets the boundary of two different dielectric materials, part of the wave is reflected back into the original medium while the rest transmits into the other medium. The properties of the reflected and transmitted EM fields are governed by the boundary conditions in the dielectric's interface. To accurately determine these properties, it is essential to consider the behavior of EM fields within the linear regime (equation (A.1)), and analyzing Maxwell's Equations (MEs) under this framework, as defined below [7]:

$$\begin{aligned} &\text{(i)}\ \ \boldsymbol{\nabla}\cdot\boldsymbol{D}=0, \qquad &&\text{(iii)}\ \ \boldsymbol{\nabla}\times\boldsymbol{E}=-\partial\boldsymbol{B}/\partial t,\\ &\text{(ii)}\ \ \boldsymbol{\nabla}\cdot\boldsymbol{B}=0, \qquad &&\text{(iv)}\ \ \boldsymbol{\nabla}\times\boldsymbol{H}=\partial\boldsymbol{D}/\partial t. \end{aligned} \tag{A.3}$$

$\boldsymbol{D}=\epsilon\boldsymbol{E}$ and $\boldsymbol{H}=\mu^{-1}\boldsymbol{B}$ are the materials constitutive relations, where $\boldsymbol{D}$,$\boldsymbol{H}$ are, respectively, the electric displacement and magnetic fields of the material. ϵ and μ are the material's electric permittivity and magnetic permeability, respectively. If the dielectric is not a magnetic material, then $\mu/\mu_0 \approx 1$, and $\boldsymbol{H}\approx\mu_0^{-1}\boldsymbol{B}$. ϵ it is directly related to $\chi^{(1)}$ (equation (A.1)) by the relation: $\epsilon=\epsilon_0(1+\chi^{(1)})$, from each one can define the ***material's dielectric constant*** as $\epsilon_d \equiv \epsilon/\epsilon_0 = 1+\chi^{(1)}$ [7]. ϵ_d it is a crucial constant because it helps define another important characteristic of a dielectric material, the ***refractive index*** n:

$$n \cong (\epsilon_d)^{1/2}. \tag{A.4}$$

n relates directly to the EM wave phase velocity v in the material by:

$$v = \frac{c}{n} = \frac{c}{(\epsilon_d)^{1/2}}\,. \tag{A.5}$$

Since, ϵ_d is almost greater than 1, then, the EM wave propagates *more slowly* inside the medium.

Due to the MEs' nature and the constitutive relations (equations (A.3)), the boundary conditions applied to the EM fields at the interface between two dielectrics materials, assumed to be free of any free charges or currents, can be written as [7]:

$$\begin{aligned} &\text{(i)}\ \epsilon_1 \boldsymbol{E_1^{\perp}} = \epsilon_2 \boldsymbol{E_2^{\perp}}, \qquad \text{(iii)} \qquad \boldsymbol{E_1^{\parallel}} = \boldsymbol{E_2^{\parallel}}, \\ &\text{(ii)}\quad \boldsymbol{B_1^{\perp}} = \boldsymbol{B_2^{\perp}}, \qquad \text{(iv)}\ \mu_1^{-1} \boldsymbol{B_1^{\parallel}} = \mu_2^{-1} \boldsymbol{B_2^{\parallel}}. \end{aligned} \tag{A.6}$$

Where ϵ_1, μ_1 labels the medium1, while ϵ_2, μ_2 states for the medium 2 in which the EM wave it is transmitted. The symbols $\perp$ and $\parallel$ states for the perpendicular and parallel components of the electric ($\boldsymbol{E}$) and the magnetic induction ($\boldsymbol{B}$) fields, respectively.

Consider now an incident monochromatic plane EM wave as it reaches the interface between these two distinct dielectrics. These materials are characterized by their respective wave vectors $\boldsymbol{k}$ (see Figure A.1with magnitudes defined as:

$$k_i = \omega / v_i = \omega n_i / c, \tag{A.7}$$

where, $i = 1, 2, 3$ and states for the incident wave ($i = 1$), the reflected ($i = 2$), and transmitted ($i = 3$). ω is the EM wave angular frequency. In the case of Figure A.1, n_1 is the refraction index for the incident and reflected EM waves, while n_2 is the refractive index of the transmitted (or *refracted*) EM wave, the appropriate coordinate system is also defined in the figure.

Figure A.1 – Schematic representation of wave vectors for a monochromatic EM wave at the interface of two different media, depicted by the grey and soft yellow regions. The boundary is defined to be the plane xy.

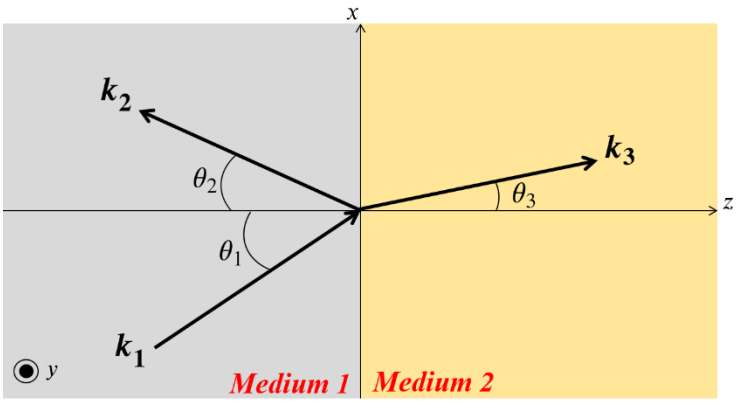

Source: The author (2024).

For a linearly polarized EM plane wave we can write the incident (I), reflected (R), and transmitted (T) fields as follows [8]:

$$\begin{aligned} &\text{(I)}\ \boldsymbol{E_1} = \boldsymbol{E_{01}} e^{i\boldsymbol{k_1}\cdot\boldsymbol{r}-i\omega t}, \quad \text{(R)}\ \boldsymbol{E_2} = \boldsymbol{E_{02}} e^{i\boldsymbol{k_2}\cdot\boldsymbol{r}-i\omega t}, \quad \text{(T)}\ \boldsymbol{E_3} = \boldsymbol{E_{03}} e^{i\boldsymbol{k_3}\cdot\boldsymbol{r}-i\omega t}, \\ &\boldsymbol{B_1} = \frac{1}{\omega}\boldsymbol{k_1}\times\boldsymbol{E_1}, \qquad \boldsymbol{B_2} = \frac{1}{\omega}\boldsymbol{k_2}\times\boldsymbol{E_2}, \qquad \boldsymbol{B_3} = \frac{1}{\omega}\boldsymbol{k_3}\times\boldsymbol{E_3}. \end{aligned} \tag{A.8}$$

$\boldsymbol{E_{01}}$,$\boldsymbol{E_{02}}$, and $\boldsymbol{E_{03}}$ are the electric fields amplitudes, $\boldsymbol{r}$ indicates the position of the wave in space, while i is the imaginary unit as usual. At $z = 0$ the boundary conditions must be satisfied, that means that all the fields' phase factors in equations (A.8) should be the same, mathematically we can state this through the expression:

$$(\boldsymbol{k_1}\cdot\boldsymbol{r})_{z=0} = (\boldsymbol{k_2}\cdot\boldsymbol{r})_{z=0} = (\boldsymbol{k_3}\cdot\boldsymbol{r})_{z=0}. \tag{A.9}$$

This equation is valid independent of the nature of the boundary conditions and the dielectrics.

Immediately, from equation (A.9), one can conclude that all the wave vectors lie in the same plane, known as the plane of incidence, along with the normal vector to the interface surface, in this case, the unitary vector that defines the direction of the z axis, z. Moreover, in the notation of Figure A.1we can rewrite equation (A.9) as:

$$k_1 \sin\theta_1 = k_2 \sin\theta_2 = k_3 \sin\theta_3. \tag{A.10}$$

Since $k_1 = k_2$ (from equation (A.7)), then $\theta_1 = \theta_2$, meaning that the incidence angle is equal to the reflection angle (***reflection law***). Furthermore, from the second equality in equation (A.10), one can conclude that:

$$n_1 \sin\theta_1 = n_3 \sin\theta_3. \tag{A.11}$$

Equation (A.11), known as ***Snell's law***, calculates the degree of light deviation when it passes from one medium to another. These results define the kinetic properties of light propagation between two dielectric media and are a consequence of the wave nature of the phenomenon, as well as the boundary conditions that must be satisfied.

The properties that determine the reflected and transmitted intensities of the radiation, as well as phase changes and polarization, are dynamic in nature and depend entirely on the boundary conditions. By applying, the boundary conditions defined in equation (A.6) to the fields described in equation (A.8) at $z = 0$, we can express the following:

$$\begin{aligned} [\epsilon_1(\boldsymbol{E_{01}} + \boldsymbol{E_{02}}) - \epsilon_2\boldsymbol{E_{03}}]\cdot z = 0, \\ [\boldsymbol{k_1}\times\boldsymbol{E_{01}} + \boldsymbol{k_2}\times\boldsymbol{E_{02}} - \boldsymbol{k_3}\times\boldsymbol{E_{03}}]\cdot z = 0, \\ (\boldsymbol{E_{01}} + \boldsymbol{E_{02}} - \boldsymbol{E_{03}})\times z = \boldsymbol{0}, \\ \frac{1}{\mu_1}(\boldsymbol{k_1}\times\boldsymbol{E_{01}} + \boldsymbol{k_2}\times\boldsymbol{E_{02}}) - \frac{1}{\mu_2}(\boldsymbol{k_3}\times\boldsymbol{E_{03}})\Big]\times z = \boldsymbol{0}. \end{aligned} \tag{A.12}$$

To apply these boundary conditions it is convenient to consider two different situations, one considering the incident EM wave with the polarization vector perpendicular to the plane of

incidence (the plane defined by $\boldsymbol{k}$ and z in Figure A.1), and other in which the polarization vector is parallel to the incidence plane. The general case of arbitrary elliptic polarization can be derived as a suitable linear combination of these two cases [8].

First, let us consider the electric field component perpendicular to the plane of incidence, as shown in the F(a). The orientations of the $\boldsymbol{B}$ vectors were chosen to ensure a positive flow of energy in the direction of the $\boldsymbol{k}$ vectors. Since the $\boldsymbol{E}$ fields are all parallel to the surface interface between the media (xy plane), the first equation in equation (A.12) reduce to zero. The third and fourth boundary conditions in equation (A.12) ensures the linear system:

$$\begin{aligned} E_{01} + E_{02} - E_{03} &= 0, \\ n_1(E_{01} - E_{02})\cos\theta_1 - n_3 E_{03}\cos\theta_3 &= 0. \end{aligned} \tag{A.13}$$

Figure A.2 – Reflection and refraction in the linear regime with polarization perpendicular (a) and parallel (b) to the plane of incidence.

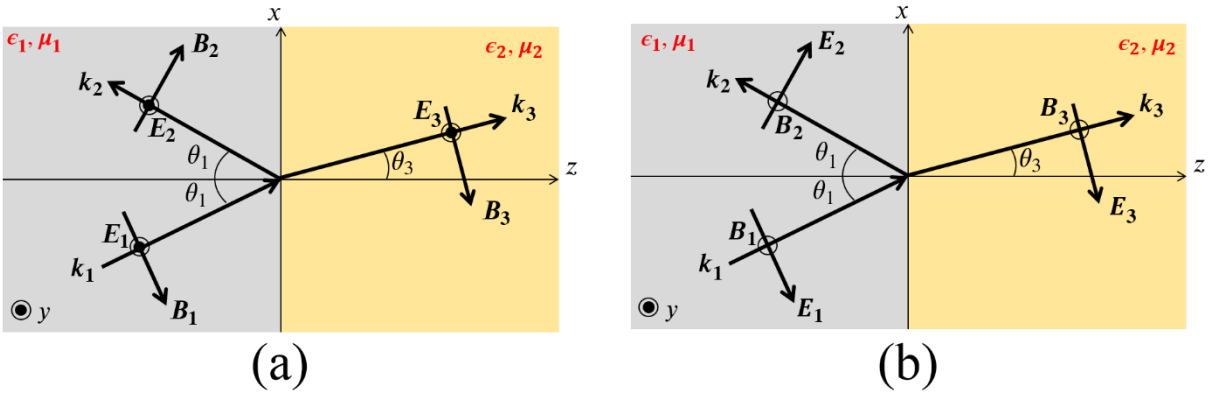

Source: The author (2024).

We use equation (A.7) to express the wave vectors in terms of the media's refractive indexes. Moreover, for optical frequencies (i.e., in nonmagnetic materials), one can assume $\mu_1 \approx \mu_0$ and $\mu_2 \approx \mu_0$. Furthermore, together with the Snell's law (equation (A.11)), the second boundary condition in equation (A.12) also ensures the second equation in equation (A.13). From the linear system in equation (A.13), we can determine the relative amplitudes of the refracted and reflected waves, which are as follows:

$$\begin{aligned} \frac{E_{03}}{E_{01}} &= \frac{2n_1\cos\theta_1}{n_1\cos\theta_1 + \left((n_3)^2 - (n_1\sin\theta_1)^2\right)^{1/2}}, \\ \frac{E_{02}}{E_{01}} &= \frac{n_1\cos\theta_1 - \left((n_3)^2 - (n_1\sin\theta_1)^2\right)^{1/2}}{n_1\cos\theta_1 + \left((n_3)^2 - (n_1\sin\theta_1)^2\right)^{1/2}}. \end{aligned} \tag{A.14}$$

Here, Snell's law was applied to express the relative amplitudes solely in terms of the incident angle and the refractive indexes of the materials. In the case of Figure A.2 (b), where the $\boldsymbol{E}$

vectors are parallel to the incidence plane, the relevant boundary conditions are given by the first, third, and fourth equations in equations (A.12) since the second one guarantees $0 = 0$. Then, from the third and fourth equations, one can obtain the following linear system:

$$\begin{aligned}(E_{01} - E_{02})\cos\theta_1 - E_{03}\cos\theta_3 = 0,\\ n_1(E_{01} + E_{02}) - n_3 E_{03} = 0.\end{aligned} \tag{A.15}$$

The first boundary condition in equation (A.12) together with the Snell's law (equation (A.11)), simply duplicates the second equation in equation (A.15). Thus, resolving this linear system for the amplitudes E_{03} and E_{02}, one can determine the relative amplitudes as:

$$\begin{aligned}\frac{E_{03}}{E_{01}} &= \frac{2n_1 n_3\cos\theta_1}{(n_3)^2\cos\theta_1 + n_1\left((n_3)^2 - (n_1\sin\theta_1)^2\right)^{1/2}},\\ \frac{E_{02}}{E_{01}} &= \frac{(n_3)^2\cos\theta_1 - n_1\left((n_3)^2 - (n_1\sin\theta_1)^2\right)^{1/2}}{(n_3)^2\cos\theta_1 + n_1\left((n_3)^2 - (n_1\sin\theta_1)^2\right)^{1/2}}.\end{aligned} \tag{A.16}$$

For the particular case of normal incidence, i.e., $\theta_1 = 0$, the relative amplitudes in equations (A.14) and (A.16) reduces to the following:

$$\begin{aligned}\frac{E_{03}}{E_{01}} &= \frac{2n_1}{n_3 + n_1},\\ \frac{E_{02}}{E_{01}} &= \frac{n_3 - n_1}{n_1 + n_3}.\end{aligned} \tag{A.17}$$

Notice that for the reflected wave, the sign convention is that for polarization parallel to the plane of incidence (Figure A.2 (b)). This means that if $n_3 > n_1$ there is a phase reversal of the reflected wave.

Two interesting aspects regarding the dynamical relations derived in equations (A.14) and (A.16) on reflection and refraction must be considered. First, for polarization components parallel to the plane of incidence, there is an angle of incidence, called ***Brewster's angle***[2], in each the reflected wave amplitude is zero. This occurs because the reflected light becomes completely polarized perpendicular to the plane of incidence at this angle. In contrast, the refracted light with initial polarization parallel to the plane of incidence is entirely transmitted. This means that there is minimal reflection of the initial parallel-polarized light.

[2] Sir David Brewster (11 December 1781 – 10 February 1868) was a Scottish scientist, inventor, author, and academic administrator, best known for his experimental contributions to physical optics, particularly in the study of light polarization and the discovery of Brewster's angle [9]. His pioneering work on polarization of light by reflection was cited as Ref. [10].

At the Brewster's angle (θ_B), the reflected and refracted light rays are at 90° angle to each other, mathematically one can write:

$$\theta_2 + \theta_3 = 90°, \tag{A.18}$$

where θ_2 is the reflection angle and θ_3 is the refraction angle, as defined previously in Figure A.2 (b). Applying equation (A.18) together with the reflection law ($\theta_1 = \theta_2$) and the Snell's law (equation (A.11)), one can derive the θ_B value as [7]:

$$\theta_B = \tan^{-1}\left(\frac{n_3}{n_1}\right), \tag{A.19}$$

where n_3 and n_1 are the refractive indexes of the dielectric mediums as in Figure A.2. As discussed previously, θ_B is the angle of incidence at which light with a particular polarization is perfectly transmitted through a surface, with no reflection. This phenomenon has various practical applications, including polarizing filters, optical coatings, laser optics, optical sensors, and light-matter interaction studies [11 – 13]. One fascinating application of Brewster's angle is Brewster Angle Microscopy (BAM). BAM is a technique used to study thin films at air-liquid interfaces. By illuminating the surface at the Brewster angle, uniformly flat areas appear dark due to minimal reflection, while regions with different refractive indices reflect light and become visible. This method enables real-time visualization of monolayers and surface phenomena [14].

The second important phenomena that appears because of the dynamical relations (equations (A.14) and (A.16)), is the possibility of ***Total Internal Reflection*** (TIR). TIR occurs when a light wave traveling in a medium with a higher refractive index hits the boundary of a medium with a lower refractive index at an angle greater than the critical angle. Under these conditions, all the light is reflected into the original medium, and none passes into the second medium. Snell's law (equation (A.11)) shows that if, $n_1 > n_3$, then $\theta_3 > \theta_1$, consequently $\theta_3 = \pi/2$, when $\theta_1 \equiv \theta_C$ where

$$\theta_C = \sin^{-1}\left(\frac{n_3}{n_1}\right). \tag{A.20}$$

θ_C is the TIR critical angle and for incident waves at $\theta_1 = \theta_C$, the refracted wave is parallel to the interface surface. Hence, there can be no energy flow through the surface, and then at θ_C there must be *total reflection*. Thus, for TIR occur, the light must travel from a denser medium to a less dense medium ($n_1 > n_3$) and the incidence angle must satisfy the requirement:

$$\theta_1 \geq \theta_C. \tag{A.21}$$

TIR is a fundamental phenomenon that underlies several important applications. One of its primary uses is in optical fibers, where it guides light signals through the fiber core, enabling long-distance communication with minimal signal loss [15]. Another interesting application is the sparkle of diamonds; their high refractive index ($n \approx 2.42$) leads to strong internal reflections, enhancing their brilliance [16]. TIR is also essential in optical instruments such as right-angle prisms, periscopes, and binoculars, where it facilitates light reflection [17]. In the field of medicine, TIR is employed in endoscopes that use optical fibers to transmit light for imaging internal body structures [18]. Furthermore, TIR helps explain natural phenomena like rainbows and mirages by reflecting light within droplets or air layers.

To conclude this section, it is worth introducing an interesting approach to understanding reflection and refraction phenomena: the application of ***Fresnel's coefficients***[3]. These coefficients precisely quantify the intensity of light that is reflected and transmitted at the interface of different dielectric materials. By examining equations (A.14) and (A.16), which detail the amplitude ratios of transmitted and reflected electrical fields for perpendicular (s) and parallel (p) polarizations; we can derive the Fresnel's coefficients as follows:

$$R_s \equiv \left(\frac{E_{02}}{E_{01}}\right)^2 = \left|\frac{n_1\cos\theta_1 - \left((n_3)^2 - (n_1\sin\theta_1)^2\right)^{1/2}}{n_1\cos\theta_1 + \left((n_3)^2 - (n_1\sin\theta_1)^2\right)^{1/2}}\right|^2,$$

and, (A.22)

$$R_p \equiv \left(\frac{E_{02}}{E_{01}}\right)^2 = \left|\frac{(n_3)^2\cos\theta_1 - n_1\left((n_3)^2 - (n_1\sin\theta_1)^2\right)^{1/2}}{(n_3)^2\cos\theta_1 + n_1\left((n_3)^2 - (n_1\sin\theta_1)^2\right)^{1/2}}\right|^2.$$

R_s and R_p quantify the fraction of an EM wave's intensity that is reflected at the interface for s and p polarizations, often referred to as reflectance in some textbooks. Due to the conservation of energy, the transmitted intensity fraction can be determined as the remaining portion of the incident intensity that is not reflected [20]:

$$T_s \equiv 1 - R_s,$$

and, (A.23)

$$T_p \equiv 1 - R_p.$$

As for the reflection coefficients defined in equation (A.22), the transmission coefficients, T_s and T_p, often are referred as transmittance coefficients. Note that equations (A.22) the (A.23) are what would be measured right at each side of an interface and do not account for attenuation

[3] Augustin-Jean Fresnel (May 10, 1788 – July 14, 1827) was a French civil engineer and physicist. His research in optics advanced the understanding that light is a transverse wave and played a significant role in the acceptance of the wave theory of light [19].

of an EM wave in an absorbing medium following transmission or reflection [20]. Considering an interface between glass ($n_1 \approx 1.5$) and air ($n_3 \approx 1.0$), it is possible to graph the reflectance and transmittance coefficients vs. the angle of incidence as exhibited in Figure A.3.

Figure A.3 – Fresnel's coefficients as a function of the angle of incidence for a glass-air interface. The dashed vertical lines indicate the Brewster's angle and the critical angle for TIR.

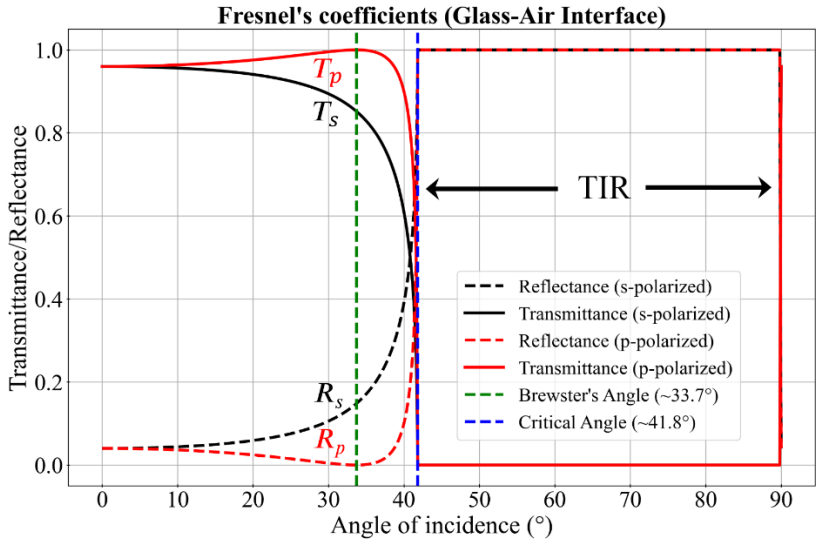

Source: The author (2024).

Observe that when the angle of incidence exceeds the critical angle (θ_C) for TIR, the inverse sine function, $\sin^{-1}$, cannot produce a valid real angle in equation (A.20). This limitation is expected when calculating the transmitted angle for incidence angles that surpass the critical angle. To address this issue, one can filter out invalid values and substitute them with $\pi/2$, which represents the angular region of TIR, as illustrated in Figure A.3.

In this section, we discussed linear reflection and refraction, which appear due to the boundary conditions (equations (A.6)) imposed by the MEs when an EM wave passes through an interface between two dielectric materials. These effects lead to intriguing phenomena such as polarization by reflection at Brewster's angle and TIR. These concepts give rise to numerous technological applications and enhance our understanding of optical phenomena. For further details and applications, see Refs. [7, 8, 21].

In the next section, we will expand the discussion on the linear regime of light-matter interaction by introducing two new concepts: absorption and dispersion.

A.1.3 Absorption and Dispersion

In the linear regime, a medium's response to an EM wave is proportional to the electric field magnitude, as discussed in section A.1.1. Absorption and dispersion are key phenomena that describe the interaction of EM waves with materials, particularly in terms of energy dissipation and wave phase velocity. Furthermore, absorption refers to the loss of energy as an EM wave travels through a medium, transferring energy typically as heat or other forms of energy. This occurs when the wave's frequency matches the natural frequencies of the material's molecules, atoms, or electrons, converting the wave's energy into vibrational, rotational, or electronic excitation within the medium [21 – 23].

Generally, to mathematically represent an absorptive medium and understand its effect on the wave propagation, we need to consider the medium's complex refractive index [20]:

$$n = n_R + in_I. \tag{A.24}$$

The real part, n_R, relates to the phase velocity and reflects the energy-storing capacity of the medium, affecting how strongly is the wave-matter interaction; while the imaginary part, n_I, represents the losses (energy dissipation within the medium) and directly governs absorption. In this way, one can consider a monochromatic plane wave propagating in the z direction within a medium and write the electric field as [20, 24]:

$$\boldsymbol{E}(z,t) = \boldsymbol{E_0} e^{i(kz-\omega t)} = \boldsymbol{E_0} e^{-ik_I z} e^{i(k_R z-\omega t)}, \tag{A.25}$$

where, $k = k_R + ik_I$ is the complex wave number, with $k_R = n_R k_0$ and $k_I = n_I k_0$ in which $k_0 = \omega/c$ is the wave number in free space. Notice that the appearance of the term $e^{-ik_I z}$ in equation (A.25) means that the wave amplitude is attenuated while the wave travels within the material. Moreover, in terms of the EM wave intensity, as $I(z) \propto |\boldsymbol{E}(z,t)|^2$, we have:

$$I(z) = I_0 e^{-\alpha_0 z}, \tag{A.26}$$

where $I_0 = I(0)$; that is I_0 is the intensity at $z = 0$ (in the interface of the material), and $\alpha_0 \equiv 2n_I k_0$ is called the ***absorption*** or ***attenuation coefficient*** of the material. The absorption coefficient can be expressed in terms of the wave frequency as:

$$\alpha_0 = 2n_I \frac{\omega}{c}. \tag{A.27}$$

The distance necessary to reduce the wave amplitude by a factor of $1/e$ (about a third) is known as the ***skin*** or ***penetration depth*** [7]:

$$d \approx \frac{1}{\alpha_0}. \tag{A.28}$$

d measures how far the wave penetrates the material. For a material to be considered transparent, its penetration depth must be large compared to its thickness. The penetration depth for metals, for instance, is exceedingly small. For example, copper at ultraviolet wavelengths ($\lambda \approx 100$ nm) has a miniscule penetration depth about 0.6 nm [20]. Table A.1, exhibits the absorption coefficients and the respective penetration depth for some materials.

Based on the values in Table A.1, it is clear that metals have very high absorption coefficients due to their strong interaction with EM waves, resulting in correspondingly shallow penetration depths. In the case of semiconductors, such as Germanium, absorption is influenced by the wavelength in relation to the material's bandgap energy, with notable absorption occurring in the infrared (IR) range. Water also demonstrates strong absorption in the microwave frequency range, making it an effective medium for energy transfer. Additionally, transparent materials like glass and plexiglass exhibit very low absorption coefficients and high penetration depths in the visible and radiofrequency ranges. Furthermore, seawater allows relatively high penetration at very low frequencies, which is advantageous for submarine communication, for example [27].

The understanding of linear absorptive responses in various materials is crucial due to its wide range of technological applications. For example, in solar cells, materials such as silicon and perovskites are specifically engineered for optimal absorption within the solar spectrum [30, 31]. Linear absorption in dyes and coatings is useful to create optical filters that selectively transmit certain wavelengths while absorbing others [21]. In medical imaging and diagnostics, the absorption properties of tissues are essential for techniques such as X-rays and near-infrared spectroscopy. Contrast agents like iodine and barium sulfate enhance absorption, resulting in clearer images [32, 33].

Table A.1 – Absorption coefficients and penetration depth of diverse materials by the range of frequency.

Material	**Frequency Range**	**Absorption coefficient (α_0) [cm^{-1}]**	**Penetration depth ($d = 1/\alpha_0$) [cm]**	**Reference**
Copper	Radio Frequency (RF)	$10^4 - 10^5$	$10^{-4} - 10^{-5}$	[25]
Silicon	Infrared (IR)	$10 - 100$	$0.1 - 0.01$	[26]
Water	Microwave (2.45 GHz)	$0.5 - 1.0$	$1.0 - 2.0$	[27]
Glass	Visible light	$10^{-4} - 10^{-5}$	$10^4 - 10^5$	[28]

(e.g. SiO_2)				
Aluminum	Radio Frequency (RF)	$10^4 - 10^5$	$10^{-4} - 10^{-5}$	[29]
Germanium	Infrared (IR)	10^3	10^{-3}	[30]
Seawater	Very Low Frequency (VLF: 300Hz – 30kHz)	0.01	100	[27]
Plexiglas (acrylic)	Radio Frequency (RF)	10^{-4}	10^4	[20]

Source: The author (2024).

Moreover, effective absorber materials are vital for the development of scientific devices like photodetectors. The principle behind photodetectors relies on the absorption of photons to generate an electrical response. To create fast photodetectors, materials such as germanium and silicon are tailored for specific wavelengths (e.g., visible light and infrared) to achieve a higher absorptive response [34, 35]. Additionally, good linear absorber materials also are useful in areas such as laser protection, environmental sensing, display technologies, and photothermal therapy [35 – 38].

Certain materials display a variation in its refractive index based on light's wavelength (or frequency); in literature, this property is referred as dispersion. Dispersion is a phenomenon that describes how the phase velocity of waves changes with frequency. It occurs due to the interaction between the waves and the medium through which they travel, causing different frequency components to travel at different speeds. The mechanism behind dispersion involves EM waves exciting oscillations in the charged particles of the medium, resulting in propagation characteristics that vary with frequency.

To represent mathematically the phenomenon of dispersion, we must consider that the materials' complex refractive index varies with the frequency:

$$n(\omega) = n_R(\omega) + i n_I(\omega), \tag{A.29}$$

where, as in the equation (A.24), $n_R(\omega)$ and $n_I(\omega)$, are the real and imaginary parts of the refractive index, respectively; however, this now depends on the wave frequency ω. The dependence of the materials' absorption coefficient with n_I (equation (A.27)) must also depends on ω as:

$$\alpha_0(\omega) = \frac{2 n_I(\omega)\omega}{c}. \tag{A.30}$$

Then, we consider the interaction between a light wave and an atom by means of the ***Lorentz oscillator model***. This model describes how the material's complex dielectric function ($\epsilon_d(\omega)$), and hence the refractive index, varies with frequency due to resonances in the material. The modeling considers the displacement of the atomic dipoles as damped harmonic oscillators – the inclusion of damping results from the fact that the oscillating dipoles can lose their energy by collisional processes. In solids, this would typically occur through an interaction with a phonon that has been thermally excited in the crystal [29].

Thus, an electron bound to an atom experiences a restoring force, leading to the equation of motion [7]:

$$\frac{d^2x}{dt^2} + \gamma \frac{dx}{dt} + \omega_0^2 x = \frac{e}{m} E_0 e^{-i\omega t}, \tag{A.31}$$

where $x = x(t)$ is the electron displacement, γ is the damping coefficient, ω_0 is the oscillator resonant frequency, m is the electron's mass, e is the fundamental electron charge, and E_0 is the amplitude of the electric field. Notice that equation (A.31) it is not considering the motion of the nucleus because the nucleus' mass is much greater than the electron's mass m. Furthermore, in the steady state, the system oscillates at the EM wave's frequency ω, and then we look for solutions of the form: $x(t) = x_0 e^{-i\omega t}$, where x_0 is the electron's equilibrium position. Therefore, from equation (A.31), this implies the follow result [7, 8, and 29]:

$$x_0(\omega) = \frac{eE_0}{m(\omega_0^2 - \omega^2 - i\gamma\omega)}. \tag{A.32}$$

The displacement of the electrons from their equilibrium position produces a time varying dipole moment, $p(t)$. Figure A.4, illustrates the appearance of the time-dependent dipole moment oscillating at the natural frequency ω_0. $x(t)$ is the time-dependent displacement of the negative charge from its equilibrium position caused by the electric force. The natural vibrations of the dipole around the equilibrium length at frequency ω_0 generate a time-dependent dipole moment $p(t)$ as indicated in the figure. $p(t)$ gives a resonant contribution to the macroscopic polarization (dipole moment per unit volume) of the medium [24, 29].

Figure A.4 – Oscillations of a classical dipole composed of a heavy positive charge and a light negative charge connected by a spring. The horizontal dotted line represents the electron equilibrium positon x_0.

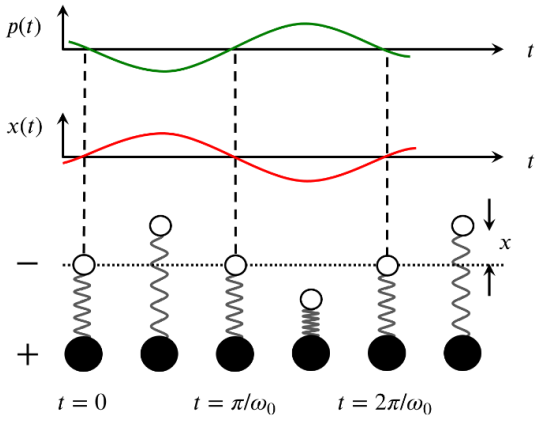

Source: The author (2024).

Considering N as the number of atoms per unit volume, we can write the resonant polarization magnitude as:

$$\begin{aligned} \boldsymbol{P}_{resonant} &= N\boldsymbol{p} \\ &= N\boldsymbol{e}\boldsymbol{x} \\ &= \frac{Ne^2}{m}\frac{1}{(\omega_0^2 - \omega^2 - i\gamma\omega)}E_0. \end{aligned} \tag{A.33}$$

Notice that the magnitude of $\boldsymbol{P}_{resonant}$ in is small unless the frequency ω is close to ω_0. This a typical characteristic of a damping oscillator, i.e., the maximum amplitude occurs when the system oscillates near the fundamental frequency.

Moreover, from equation (A.33), is it possible to obtain the complex dielectric constant $\epsilon_d(\omega)$. Using the MEs' constitutive relations (equations (A.3)), one can write the electric displacement vector $\boldsymbol{D}$ in terms of the medium's polarization $\boldsymbol{P}$ as follow:

$$\boldsymbol{D} = \epsilon_0 \boldsymbol{E_0} + \boldsymbol{P}. \tag{A.34}$$

However, our focus is on optical responses at frequencies close to ω_0, and so is necessary to split the polarization $\boldsymbol{P}$ into two terms to account for a non-resonant background and the resonance arising from the driven response of the oscillator. Therefore, one can write:

$$\begin{aligned} \boldsymbol{D} &= \epsilon_0 \boldsymbol{E_0} + \boldsymbol{P}_{background} + \boldsymbol{P}_{resonant} \\ &= \epsilon_0 \boldsymbol{E_0} + \epsilon_0 \chi^{(1)} \boldsymbol{E_0} + \boldsymbol{P}_{resonant}. \end{aligned} \tag{A.35}$$

To simplify the mathematics, we can consider an isotropic medium. In this case, we can define the complex dielectric constant $\epsilon_d(\omega)$ through the relationship (see equations (A.3) in Section A.1.2):

$$\boldsymbol{D} = \epsilon_0 \epsilon_d \boldsymbol{E_0}. \tag{A.36}$$

Combining equations (A.33) and (A.35), and then comparing with equation (A.36), we can obtain:

$$\epsilon_d(\omega) = 1 + \chi^{(1)} + \frac{Ne^2}{\epsilon_0 m}\frac{\omega_0^2 - \omega^2}{\left(\omega_0^2 - \omega^2\right)^2 + (\gamma\omega)^2} + i\frac{Ne^2}{\epsilon_0 m}\frac{\gamma\omega}{\left(\omega_0^2 - \omega^2\right)^2 + (\gamma\omega)^2}. \tag{A.37}$$

As for the refractive index (equation (A.29)), we can split the complex dielectric constant as real and imaginary parts as: $\epsilon_d(\omega) \equiv \epsilon_R(\omega) + i\epsilon_I(\omega)$. Then, from equation (A.37), we can explicit write $\epsilon_R(\omega)$ and $\epsilon_I(\omega)$ as:

$$\epsilon_R(\omega) = \mathrm{Re}\{\epsilon_d(\omega)\} = 1 + \chi^{(1)} + \frac{Ne^2}{\epsilon_0 m}\frac{\omega_0^2 - \omega^2}{\left(\omega_0^2 - \omega^2\right)^2 + (\gamma\omega)^2},$$

and (A.38)

$$\epsilon_I(\omega) = \mathrm{Im}\{\epsilon_d(\omega)\} = \frac{Ne^2}{\epsilon_0 m}\frac{\gamma\omega}{\left(\omega_0^2 - \omega^2\right)^2 + (\gamma\omega)^2}.$$

Equations (A.38) describes the real and imaginary parts of the dielectric function, $\epsilon(\omega)$, deduced form the Lorentz oscillator model for one single resonance frequency. Some textbooks defines the constant $\omega_p \equiv \left(Ne^2/\epsilon_0 m\right)^{1/2}$ as the *plasma frequency*, and $\epsilon_\infty \equiv 1 + \chi^{(1)}$ as the high-frequency dielectric constant – ϵ_∞ takes into account contributions from non-resonant electrons [8]. In this way, we can rewrite equations (A.38), as follow:

$$\epsilon_R(\omega) = \epsilon_\infty + \frac{\omega_p^2(\omega_0^2 - \omega^2)}{\left(\omega_0^2 - \omega^2\right)^2 + (\gamma\omega)^2},$$

and (A.39)

$$\epsilon_I(\omega) = \frac{\omega_p^2\gamma\omega}{\left(\omega_0^2 - \omega^2\right)^2 + (\gamma\omega)^2}.$$

From equation (A.29), we can relates equations (A.39) directly to the medium's refraction indexes, $n_R(\omega)$ and $n_I(\omega)$. It is very common in the literature define the imaginary part of the refractive index ($n_I(\omega)$) as the ***extinction coefficient***: $\kappa \equiv n_I(\omega)$. Moreover, is also common to refer to the real part of the refractive index ($n_R(\omega)$)) as the ***medium's refraction index***: $n \equiv n_R(\omega)$. These constants, n and κ, are related with ϵ_R and ϵ_I by the follow expressions [24, 29]:

$$n^2 - \kappa^2 = \epsilon_R,$$

and (A.40)

$$2n\kappa = \epsilon_I.$$

Thus, we can explicitly solve equations (A.40) for n and κ in terms of the dielectric constants as:

$$n = \left(\frac{\epsilon_R + \sqrt{\epsilon_R^2 + \epsilon_I^2}}{2} \right)^{1/2},$$

and (A.41)

$$\kappa = \left(\frac{-\epsilon_R + \sqrt{\epsilon_R^2 + \epsilon_I^2}}{2} \right)^{1/2}.$$

These relations highlight how the phenomena of dispersion (ϵ_R) and absorption (ϵ_I) contribute to the material's optical properties. n describes the phase velocity of light in the material, while κ describes the attenuation of the wave as it propagates through the material.

It is important to evaluate the behavior of the dielectric constants, and consequently, n and κ, in some frequency domains; that is, for the low frequency regime ($\omega \ll \omega_0$), resonant regime ($\omega \approx \omega_0$), and for the high-frequency regime ($\omega \gg \omega_0$). Thus, equations (A.39) and (A.41) allowing us to evaluate the frequency dependence of these constants.

Table A.2, summarizes the expressions for each frequency domain, which helps understand their physical implications. From the expressions in Table A.2, it is evident that in the low frequency regime ($\omega \ll \omega_0$), the material behaves like a static dielectric, with negligible absorption (ϵ_I and κ goes to ≈ 0). Near resonance ($\omega \sim \omega_0$), both ϵ_R and ϵ_I are significant, thus dispersion and absorption effects are dominant. In this regime, is expected a peak in the $\kappa(\omega)$ curve due to the resonant absorption. For the high-frequency regime ($\omega \gg \omega_0$), the material has a reduced dielectric constant due to negligible interaction of the wave bound charges, and absorptive effects are negligible. Figure A.5, shows the frequency dependence of the dielectric functions and the refraction/extinction coefficients near resonance calculated from equations (A.39) and (A.41).

Observing Figure A.5 (b), it is clear that function $\epsilon_I(\omega)$ exhibits a strongly peaked behavior, reaching its maximum value at ω_0 and having a full width at half-maximum equal to γ. In contrast, the frequency dependence of ϵ_R is more intricate (see Figure A.5 (a)). As ω approaches ω_0 from below, ϵ_R gradually increases from its low frequency value, peaking at $\omega_0 - \frac{\gamma}{2}$. It then sharply decreases, reaching a minimum at $\omega_0 + \frac{\gamma}{2}$, before rising again toward its high-frequency limit (see Table A.2). The frequency range over which these variations occur is governed by γ and for both ϵ_R and ϵ_I. This behavior illustrates how oscillator damping causes line broadening. The frequency dependence of ϵ_R and ϵ_I, depicted in Figure A.5 , is known as

Lorentzian, named after the originator of the dipole model [7, 29]. It is important to note that we experimentally measured the refractive index n and the absorption coefficient α_0, which is related to the extinction coefficient κ by equation (A.30).

Table A.2 – Reduced expressions for the dielectric constants. Low, Resonance, and High-Frequency Regimes*.

Frequency Regime	$\epsilon_R(\omega)$	$\epsilon_I(\omega)$	$n(\omega)$	$\kappa(\omega)$
Low Frequency ($\omega \ll \omega_0$)	$\epsilon_\infty + \omega_p^2/\omega_0^2$	≈ 0	$\sqrt{\epsilon_\infty + \omega_p^2/\omega_0^2}$	≈ 0
Near Resonance ($\omega \sim \omega_0$)	$\epsilon_\infty + \frac{\omega_p^2(\omega_0^2-\omega^2)}{(\omega_0^2-\omega^2)^2+(\gamma\omega)^2}$	$\frac{\omega_p^2\gamma\omega}{(\omega_0^2-\omega^2)^2+(\gamma\omega)^2}$	$\sqrt{\frac{\epsilon_R+\sqrt{\epsilon_R^2+\epsilon_I^2}}{2}}$	$\sqrt{\frac{-\epsilon_R+\sqrt{\epsilon_R^2+\epsilon_I^2}}{2}}$
High Frequency ($\omega \gg \omega_0$)	$\epsilon_\infty - \omega_p^2/\omega_0^2$	≈ 0	$\sqrt{\epsilon_\infty - \omega_p^2/\omega_0^2}$	≈ 0

**For simplicity, we assume a weak damping oscillator model* ($\omega_0 \gg \gamma$).

Source: The author (2025).

The Lorentzian oscillator model provides a classical approach for understanding dispersion by considering the response of a single resonance to an EM wave. While this model effectively captures the essential features of frequency-dependent dielectric functions near resonance, it is limited to a single oscillatory mode and does not account for more complex material behaviors. Modern approaches, such as the Drude model for free-electron systems or quantum mechanical models like the Kramers-Kronig relations, offer more comprehensive insights into dispersion and absorption phenomena [8, 24, 29]. These models extend the understanding of optical properties by incorporating multiple resonances and quantum effects, thereby providing a more complete description of real materials.

In the next section, we will explore linear scattering, a fundamental phenomenon in light-matter interactions where electromagnetic waves are redirected without frequency alteration. This process is crucial in various applications, from explaining the sky's color through Rayleigh scattering to developing advanced optical materials and technologies. By examining the mechanisms and implications of linear scattering, we will reveal its importance in both natural phenomena and technological advancements.

Figure A.5 - Frequency dependence of the real and imaginary parts of the complex dielectric function of a dipole oscillator at frequencies close to resonance. The curves are calculated for an oscillator with $\omega_p = 1.5$, $\epsilon_\infty = 2.0$ and $\gamma = 0.1$ (weak damping).

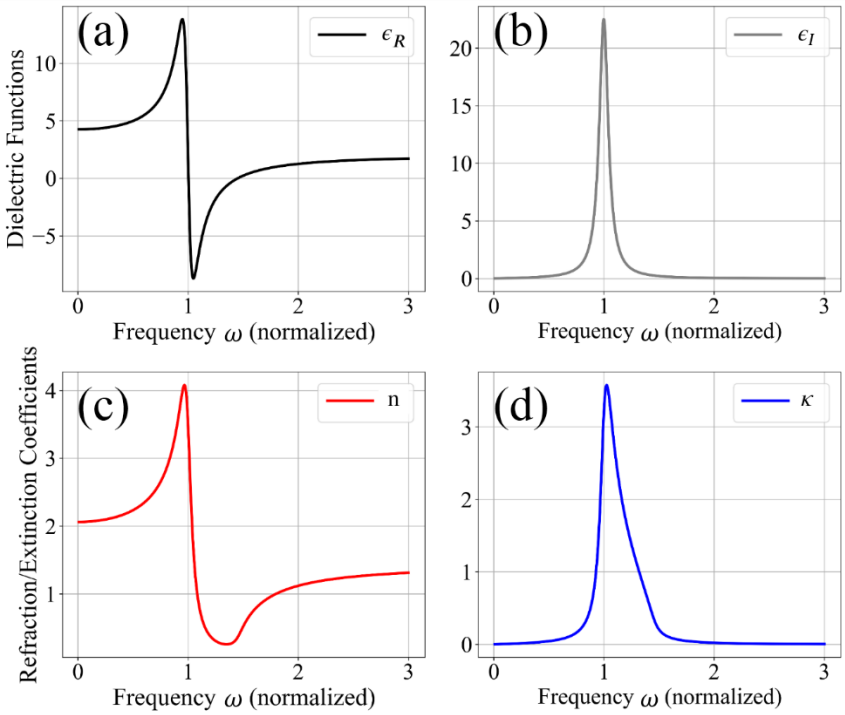

Source: The author (2025).

A.1.4 Linear Scattering

Linear scattering is a fundamental optical phenomenon that occurs when an EM wave interacts with matter and is redirected without any change in its frequency. This process is influenced by the size, shape, and refractive properties of the scattering particles in relation to the wavelength of the incoming wave. Linear scattering is essential for explaining a wide range of natural and technological phenomena, including the blue color of the sky, the appearance of fog and clouds, and the performance of optical fibers and photonic devices [20, 39].

In this section, we will explore the basic principles of linear scattering, including Rayleigh, Mie, and Tyndall scattering, along with their applications and implications in both scientific research and practical engineering.

Linear scattering occurs when the electric field of a wave interacts with charged particles within a medium. This interaction causes oscillations and the re-emission of light in various directions. The size of the scattering particles relative to the wavelength of the incoming wave is a crucial factor in this process. If the particles are much smaller than the wavelength,

stronger scattering occurs at shorter wavelengths. This phenomenon is commonly referred to in the literature as ***Rayleigh scattering***[4].

To have an insight of Rayleigh scattering phenomena, let us consider a plane monochromatic EM wave to be incident on a particle (scatterer) whose size r satisfies $r \ll \lambda$, where λ is the wavelength of the incident light. The electric field of the incident EM wave induces an oscillating dipole moment $\boldsymbol{p}$ in the particle as:

$$\boldsymbol{p} = \alpha \boldsymbol{E}. \tag{A.42}$$

α is defined as the polarizability of the particle, and it is determined by the material properties and size. As usual, $\boldsymbol{E}$ is the electric field of the incident wave. The scattered power, that is, the power radiated by the induced dipole $\boldsymbol{p}$ is given by the following formula [8]:

$$P_{scattered} \propto \frac{\omega^4 |\alpha|^2 |\boldsymbol{E}|^2}{c^3}. \tag{A.43}$$

$\omega = 2\pi c/\lambda$, is the angular frequency of the incident EM wave. From equation (A.43) is possible to conclude that the scattered intensity I is proportional to $1/\lambda^4$, which explains the strong dependence of scattering on wavelength:

$$I \propto \frac{1}{\lambda^4}. \tag{A.44}$$

This relationship is the reason due to shorter wavelengths (blue) scatter more than longer wavelengths (red). Additionally, the angular dependence of Rayleigh scattering is given by following expression [8, 24]:

$$I(\theta) \propto 1 + \cos^2(\theta), \tag{A.45}$$

where θ is the scattering angle. This expression indicates that the scattered light is symmetric about the incident direction, with the maximum intensity in the forward and backward directions. Moreover, the scattered light is partially polarized. Light scattered at 90º is completely polarized because the electric field oscillations are confined to a plane perpendicular to the scattering direction. At other angles, the degree of polarization depends on the scattering geometry and incident polarization [24].

As mentioned earlier, one of the applications of the Rayleigh scattering is to explain atmospheric phenomena, such as the blue sky and sunsets. Equation (A.44) indicates that shorter wavelengths (blue light) scatters more efficiently. Then, as sunlight crosses a region of

[4] The phenomenon is named after 19th-century British physicist Lord Rayleigh (John William Strutt), who, in 1871, analyzed scattered sunlight in terms of a molecular oscillator and concluded that the intensity of the scattered light is proportional to $1/\lambda^4$ [40].

widely spaced air molecules (scatterers), the light laterally scattered is mostly blue, and that is why the sky is seen to be blue. The unscattered light, which is rich in red, is viewed only when the Sun is low in the sky at sunrise and sunset. Solar rays reach about 18° beyond the daytime terminator because of atmospheric scattering; then, over this twilight band, the skylight fades to the complete darkness of night [20].

Rayleigh scattering is vital in other areas, such as in LiDAR (Light Detection and Ranging) and remote sensing to evaluate atmospheric composition and density [41, 42]. It also plays a crucial role in optical instrumentation, facilitating the design of anti-reflective coatings, optical filters, and photonic devices to manage unwanted scattering [43 – 45]. Rayleigh scattering is a classical model, and a deeply explanation of the scattering phenomena in the regime $r \ll \lambda$ can be given by quantum electrodynamics and extended to complex media through statistical models [39].

One fundamental concept in light-matter interactions appears when the scatterers possess sizes comparable to the wavelength of the incident light. This characterizes what is kwon as ***Mie scattering***. Unlike Rayleigh scattering, which applies to particles much smaller than the wavelength, Mie scattering provides a more comprehensive framework, accounting for a wide range of particle sizes and refractive indices. This theory, developed by Gustav Mie[5], plays a critical role in understanding natural phenomena such as the white appearance of clouds and the scattering of light in colloidal solutions. Moreover, it plays a crucial role in various technological applications, including atmospheric science, biomedical imaging, and optical communication, making it an indispensable tool in the study of light propagation in complex media [47 – 49].

The Mie scattering theory describes the scattering of light by a spherical particle with radius ρ and a refractive index n. The theory gives a series of equations that determine the scattering coefficients, angular distribution, and other characteristics of scattered light based on the properties of the particle and the incident wave. The key parameters of the Mie's scattering theory are the wavelength of the incidence EM wave λ, the particle radius ρ, the sphere's refractive index n, the surrounding medium refractive index n_0, and the size parameter defined as:

[5] Gustav Adolf Feodor Wilhelm Ludwig Mie (German: [mi:]; 29 September 1868 – 13 February 1957) was a German physicist. His work included Mie scattering, Mie potential, the Mie–Grüneisen equation of state and an early effort at classical unified field theories [46].

$$x \equiv \frac{2\pi\rho}{\lambda}, \tag{A.46}$$

which is related to the ratio of the particle's size to the wavelength. Mie scattering theory involves finding the expansion coefficients in a series of spherical harmonics. The total scattered field consists of both electric and magnetic components, and the solution involves spherical Bessel functions.

The scattered field is expressed in terms of spherical multipoles, utilizing the ***Mie coefficients*** a_n and b_n. The electric and magnetic field components of the scattered field are defined as follows [39]:

$$E_{scattered} = \sum_{n=1}^{\infty} \left(a_n \frac{H_n^{(1)}(kr)}{kr} + b_n \frac{H_n^{(2)}(kr)}{kr} \right) \cdot e^{in\theta}, \tag{A.47}$$

where $H_n^{(1)}$ and $H_n^{(2)}$ are the spherical Hankel functions of the first and second kinds, respectively. a_n and b_n are the Mie scattering coefficients for the electric and magnetic fields, $k = 2\pi/\lambda$ is the wave number, and r is the radial distance from the center of the particle. a_n and b_n are given in terms of the spherical Bessel functions as follow [39]:

$$a_n = \frac{m\psi_n(mx)\psi_n'(x) - \psi_n'(mx)\psi_n(x)}{m\psi_n(mx)\xi_n'(x) - \psi_n'(mx)\xi_n(x)},$$

and (A.48)

$$b_n = \frac{\psi_n(mx)\psi_n'(x) - m\psi_n'(mx)\psi_n(x)}{\psi_n(mx)\xi_n'(x) - m\psi_n'(mx)\xi_n(x)}.$$

In equation (A.48), x is the size parameter as defined in equation (A.46), $\psi_n(z) \equiv z j_n(z)$ and $\xi_n(z) \equiv z h_n^{(1)}(z)$, where $j_n(z)$ and $h_n^{(1)}(z)$ are the spherical Bessel and Hankel functions, respectively. $\psi_n'(x)$ and $\xi_n'(x)$ are the first derivatives with respect to its arguments. Moreover, the parameter $m \equiv n/n_0$ is the relative refraction index. From equations (A.47) and (A.48), the Mie's theory predicts the scattering and extinction cross-sections, $\sigma_{scattering}$ and $\sigma_{extinction}$, from those one can derive the material's absorption cross-section: $\sigma_{absorption} = \sigma_{extinction} - \sigma_{scattering}$. Furthermore, the Mie's theory is capable to predict accurately the normalized ***phase function***, $P(\theta)$, that describes the angular distribution of the scattered light as [39]:

$$P(\theta) = I(\theta) \Big/ \left(\int_0^{\pi} I(\theta)\sin(\theta) d\theta \right). \tag{A.49}$$

$I(\theta)$ is the intensity of the scattered light in a given direction, and is related to the angular functions $\tau_n(\cos\theta)$ and $\pi_n(\cos\theta)$, where the index n states for the multipole's expansion order. $I(\theta)$ can be decomposed into two orthogonal polarizations, $I_{\parallel}(\theta)$ and $I_{\perp}(\theta)$. The detailed

mathematical expressions for the cross-sections and the phase function $I(\theta)$ can be found in Refs. [39] and [50]. For simplicity, Figure A.6 shows the normalize phase function curve for a scattering system where $P(\theta) \propto |\cos(\theta)|^2$.

From the $P(\theta)$ curve exhibited in Figure A.6, we can infer some specific characteristics about the particle size and its interaction with the scattering system. $P(\theta)$ exhibits strong symmetry about 90°, which indicates dipole-like scattering. Then, we can conclude that the particle size is small compared to the wavelength of the incident light, since dipole scattering prevails for small particles. Therefore, the size parameter for this system can be expressed as: $x = 2\pi\rho/\lambda \ll 1$, indicating Rayleigh scattering.

Figure A.6 – Angular scattering intensity distribution of the Mie's theory phase function. The vertical dashed lines indicate some highlighted angles: red ($\theta = 0°$) forward scattering, blue ($\theta = 90°$) side scattering and orange ($\theta = 180°$) backscattering.

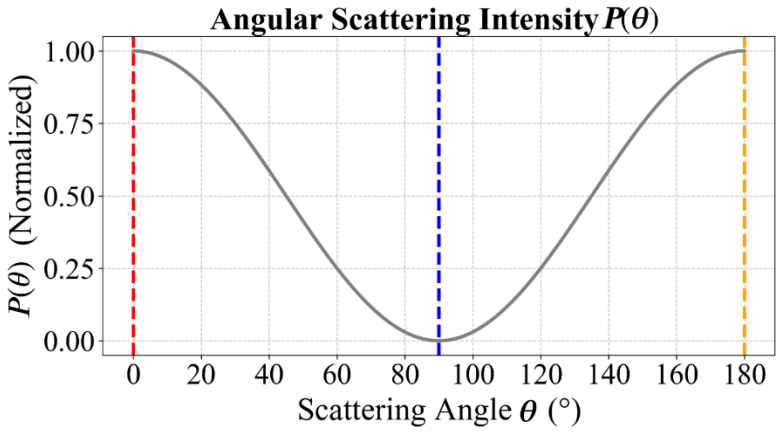

Source: The author (2025).

Observing Figure A.6, is noticeable that forward ($\theta = 0°$) and ($\theta = 180°$) backward scattering are stronger as compared with side scattering for $\theta = 90°$, characteristics present in Rayleigh-like scattering systems. The cosine pattern of $P(\theta)$ also give us information regarding the polarization of the incident light: the light is likely polarized. For unpolarized light, $P(\theta)$ is usually more isotropic and would not exhibit a pure $|\cos(\theta)|^2$ dependence, as exhibited in Figure A.6. Thus, from the scattering angular intensity distribution curve, we can gather crucial aspects about the scattering system. The case illustrated in Figure A.6, emulates a Rayleigh-like scattering system possessing scatters likely spherical or nearly isotropic in shape, with the medium likely uniform without significant contributions from multiple scattering [39].

In addition to Rayleigh and Mie scattering, ***Tyndall scattering***[6] plays a significant role in how light interacts with particles. This phenomenon, often observed in colloidal suspensions and fine emulsions, occurs when particles are large enough to scatter light but still small compared to the wavelength of the light resulting in a visible scattering effect [51, 52]. Tyndall scattering is responsible for the characteristic blue appearance of illuminated smoke or mist [24, 50]. It serves as a bridge between Rayleigh and Mie scattering, highlighting the continuum of light-matter interactions that depend on particle size and wavelength. Table A.3, summarizes the regimes, size parameters, and notable applications for Rayleigh, Mie, and Tyndall scattering phenomena.

Table A.3 – Regimes, size parameters, and applications of different linear scattering phenomena.

Scattering type	**Size parameter** $(x = 2\pi\rho/\lambda)$	**Particle size relative to wavelength**	**Notable applications**
Rayleigh	$x \ll 1$	Particle size much smaller than wavelength ($\rho \ll \lambda$)	Blue color of the sky, sunsets, and atmospheric optics.
Mie	$x \sim \rho$	Particle size comparable to wavelength ($\rho \sim \lambda$)	Cloud formation, fog, aerosol behavior, particle characterization.
Tyndall	$x < 1$ (but larger than Rayleigh)	Particle size slightly smaller but comparable to the wavelength ($\rho < \lambda$)	Visible beams in colloids, milk's blue hue, mist scattering.

Source: The author (2025).

The purpose of this section was to provide a brief and clear overview of fundamental linear light-matter interaction effects in low-intensity regimes, offering essential insights into these effects, based on current and standard literature. It is important to note that the understanding of linear effects remains an active area of scientific investigation and has applications in modern technology, such as BAM and LiDAR applications as discussed previously.

Linear optical effects such as refraction, reflection, absorption, dispersion, and scattering offer insights of light-matter interactions at low to moderate intensities. However,

[6] The phenomenon is named for the 19th-century British physicist John Tyndall, who first studied it extensively. Some textbooks refer to it as the Tyndall effect. The pioneering work made by J. Tyndall on the scattering of particles large enough to scatter light is cited as Ref. [51].

this understanding shift significantly at high-intensities (typically in the GW/m² range), where the material's response becomes nonlinear and numerous new effects emerge. The next section will cover the fundamentals of nonlinear optical effects.

A.2 Light-Matter Interaction: Nonlinear Regime

The light-matter interaction enters a fascinating regime under high-intensity illumination, where the induced polarization is no longer directly proportional to the electric field. This leads to nonlinear optical effects. In this regime, the material's response to the electromagnetic field becomes intensity-dependent, leading to phenomena such as harmonic generation, multi-photon absorption, self-phase modulation, and optical rectification. These effects not only highlight the complexity of light-matter interactions within a theoretical framework but also serve as the foundation of nonlinear optics. They enable powerful applications in modern photonics, including nonlinear spectroscopy, imaging, and laser technology, providing essential tools for probing and manipulating materials at both the molecular and atomic levels.

In the upcoming sections, the aim is to establish a foundation on the fundamental principles of nonlinear optics, providing the reader with insights into key phenomena, with a particular emphasis on third-order effects.

A.2.1 Nonlinear Polarization Tensor

Section A.1.1 introduced an expression for the polarization vector $\boldsymbol{P}$ of a material under a weak external electric field $\boldsymbol{E}$ applied. In this context, $\boldsymbol{P}$ is directly proportional to $\boldsymbol{E}$, with a proportional constant defined as the first-order linear susceptibility tensor of the material, denoted as $\chi^{(1)}$ (a scalar for isotropic media). However, the tensorial behavior of polarization is evident in nonlinear optics, particularly at high field intensities, because the response of a material to an electric field is not isotropic in general. The nonlinear polarization $\boldsymbol{P}$ depends on the electric field $\boldsymbol{E}$ in a way that reflects the symmetry and anisotropy of the material's molecular or crystal structure [53 – 55]. Thus, a more complete mathematical expression for $\boldsymbol{P}$ must be:

$$\boldsymbol{P} = \boldsymbol{P}^{(1)} + \boldsymbol{P}^{(2)} + \boldsymbol{P}^{(3)} + \cdots, \tag{A.50}$$

where, $\boldsymbol{P}^{(1)}$ is the first-order component (the linear polarization term), and $\boldsymbol{P}^{(2)}$, $\boldsymbol{P}^{(3)}$, etc., represent the second-order, third-order, and higher-order nonlinear polarization components, these components will be significant at high-intensity regimes. Notice that, in equation (A.50), we are not considering a medium with spontaneous polarization contribution, that means, the zero-order term must be: $\boldsymbol{P}^{(0)} = \boldsymbol{0}$.

Thus, the polarization vector $\boldsymbol{P}$ at each order of nonlinearity can be expressed as [53]:

$$P_i^{(n)} = \epsilon_0 \sum_{j_1, j_2, \cdots, j_n} \chi^{(n)}_{i j_1, j_2, \cdots, j_n} E_{j_1} E_{j_2} \cdots E_{j_n}, \tag{A.51}$$

where $\boldsymbol{P}^{(n)}$ is the n-th order polarization vector as defined in equation (A.51), $\chi^{(n)}$ is the n-th order susceptibility tensor, which is of rank $n+1$, and E_{j_k} are the Cartesian components of the electric field. The indices $i, j_1, j_2, \cdots, j_n$ denotes the Cartesian components of the tensors and vectors. From equation (A.51), we can explicitly derive the second- and third-order nonlinear components. Then, for $n = 2$, the second-order polarization component is:

$$P_i^{(2)} = \epsilon_0 \sum_{j_1, j_2} \chi^{(2)}_{i j_1 j_2} E_{j_1} E_{j_2}. \tag{A.52}$$

This means that the components $P_i^{(2)}$ depends on all combinations of the electric field $\boldsymbol{E}$ components, weighted by the susceptibility tensor $\chi^{(2)}$. For $n = 3$ in equation (A.51), one can write the third-order polarization component as:

$$P_i^{(3)} = \epsilon_0 \sum_{j_1, j_2, j_3} \chi^{(3)}_{i j_1 j_2 j_3} E_{j_1} E_{j_2} E_{j_3}. \tag{A.53}$$

Here, the third-order susceptibility tensor $\chi^{(3)}$ is a rank-4 tensor, and it accounts for effects like third-harmonic generation and self-focusing [54].

The second and third-order polarization components exhibited in equations (A.53) and (A.52) can be shortened by employing Einstein's summation convention. This mechanism is widely used to compactly represent sums over the components of tensors and vectors [53, 54]. Applying the Einstein's summation rules one can rewrite these expressions as follows:

$$\boldsymbol{P}^{(2)} = \epsilon_0 \chi^{(2)} : \boldsymbol{EE},$$

and (A.54)

$$\boldsymbol{P}^{(3)} = \epsilon_0 \chi^{(3)} \vdots \boldsymbol{EEE}.$$

The vertical dots means summation over repeated indexes in tensorial notation. Notice that in equation (A.52) the indices j_1 and j_2 are summed over all spatial dimensions (e.g., x, y, z or 1, 2, 3 in Cartesian coordinates). In this case, Einstein's notation replace the summation over the indexes for the two vertical dots to produce the total second-order polarization vector $\boldsymbol{P}^{(2)}$, as one can see in equation (A.54). The same strategy is applied for express $\boldsymbol{P}^{(3)}$ and any other nonlinear higher-order component of $\boldsymbol{P}$.

The following section will concentrate on the study and implications of applying the $\boldsymbol{P}^{(2)}$ as polarization's first correction term and discuss the myriad of nonlinear phenomena that appear, such as second harmonic generation.

A.2.2 Second-order Effects

Second-order nonlinear optical effects arise when the induced polarization in a material responds nonlinearly to the applied electric field according to equation (A.52). This indicates that $\boldsymbol{P}^{(2)}$ depends quadratically on the electric field components. The second-order effects occur predominantly in materials lacking inversion symmetry (non-centrosymmetric), such as certain crystals, because centrosymmetric materials have $\chi^{(2)} = 0$ [53, 54]. For example, lithium niobate ($LiNbO_3$) and potassium titanyl phosphate (KTP) are commonly used nonlinear crystals due to its absence of inversion symmetry [55, 56].

Moreover, to ensure efficient nonlinear interactions, the ***Phase Matching*** requirement is another important condition that must be achieved for generating second-order effects. This condition ensures that the interacting waves remain in phase as they propagate through the medium. Basically, the phase matching condition means that the interacting waves constructively interfere as they propagate through the nonlinear medium, maximizing energy transfer between the fundamental and generated waves [53, 54]. For a second-order nonlinear process, the phase matching condition can be expressed as:

$$\Delta k = k_3 - k_2 - k_1, \tag{A.55}$$

where k_3, k_2, k_1 are the wave vectors of the interacting waves (e.g., fundamental and second-harmonic waves), and Δk is the ***wave vector mismatch***. When $\Delta k = 0$, means that the process is perfectly phase-matched, leading to efficient energy transfer. However, if $\Delta k \neq 0$, then destructive interference process reduces the efficiency of the nonlinear interaction [53, 54]. Several experimental techniques exist to achieve phase matching conditions, including birefringent phase matching (BPM), quasi-phase matching (QPM), and temperature tuning [57 – 59].

Let us explore the mathematical fundamentals of second-order nonlinear effects and the key phenomena involved, including second harmonic generation (SHG), sum-frequency generation (SFG), difference-frequency generation (DFG), and optical rectification (OR).

The second-order nonlinear effects are governed by the nonlinear polarization $\boldsymbol{P}^{(2)}$ (equation (A.54)), which can be expressed as:

$$\boldsymbol{P}^{(2)}(t) = \epsilon_0 \chi^{(2)} : \boldsymbol{E}(t)\boldsymbol{E}(t), \tag{A.56}$$

where $\chi^{(2)}$ is a third-rank tensor possessing 27 elements, and $\boldsymbol{E}(t)$ is the electric field of the light wave. If the electric field $\boldsymbol{E}(t)$ contains multiple frequency components, the quadratic

dependence of $\boldsymbol{P}^{(2)}$ on $\boldsymbol{E}(t)$ generates new frequency as will be discussed in the following paragraphs.

Let us consider an electric field $\boldsymbol{E}(t)$ possessing two optical frequencies components as follows:

$$\boldsymbol{E}(t) = \boldsymbol{E_1} e^{-i\omega_1 t} + \boldsymbol{E_2} e^{-i\omega_2 t} + c.c., \tag{A.57}$$

where $\boldsymbol{E_1}$ and $\boldsymbol{E_2}$ are the complex amplitudes of the respective frequency components, ω_1 and ω_2. The term $c.c.$ stands for the complex conjugate term to ensure $\boldsymbol{E}(t)$ as a real quantity. The product term $\boldsymbol{E}(t)\boldsymbol{E}(t)$ in equation (A.56) produces new frequencies through the second-order nonlinear interaction [53, 54, and 60]:

$$\boldsymbol{E}(t)\boldsymbol{E}(t) = \boldsymbol{E_1}\boldsymbol{E_2} e^{-i(\omega_1+\omega_2)t} + \boldsymbol{E_1}\boldsymbol{E_2^*} e^{-i(\omega_1-\omega_2)t} + \boldsymbol{E_1^2} e^{-i(2\omega_1)t} + c.c.. \tag{A.58}$$

Thus, from equation (A.58), it is clear that the second-order polarization gives rise to terms oscillating at the double, the sum and difference of the fundamentals frequencies.

The first phenomenon that will be discussed is caused by the double frequency oscillation term in equation (A.58) and oscillates by a factor of $e^{-i2\omega t}$. This effect is kwon as ***second-harmonic generation (SHG)***, and means that two photons of the same frequency ω interacts to generate a photon of frequency 2ω. The polarization component of the SHG effect one can be expressed as:

$$P_i^{(2\omega)} = \epsilon_0 \chi_{ijk}^{(2)} E_j(\omega) E_k(\omega). \tag{A.59}$$

The nonlinear polarization term $P_i^{(2\omega)}$ acts as a source term for the second-harmonic field, and the wave equation for this field amplitude is [53 – 61]:

$$\nabla^2 E(2\omega) - \frac{1}{c^2}\frac{\partial^2 E(2\omega)}{\partial t^2} = \mu_0 \frac{\partial^2 P_i^{(2\omega)}}{\partial t^2}. \tag{A.60}$$

From equation (A.60), it is possible to deduce the phase matching condition for the SGH [53 – 61]:

$$k(2\omega) = 2k(\omega), \tag{A.61}$$

where $k(\omega)$ is the wave vector of the fundamental frequency ω. Figure A.7 (a) gives a geometrical idea of the SHG effect. SHG phenomenon is widely used in various scientific and technological fields, such as microscopy [62], frequency doubling lasers [53], optical communications [63], material characterization [54], quantum optics and photonics, and diagnostic and sensing [64, 65].

Figure A.7 – Second-order nonlinear process. (a) SHG, (b) SFG, (c) DFG, and (d) OR. The insets illustrates the energy level diagrams, where the continuous and dashed horizontal lines represents the ground states and the virtual states involved in the process, respectively. The sign of $\chi^{(2)}$ depends on the relative orientations of the interacting waves and the material's optical axes.

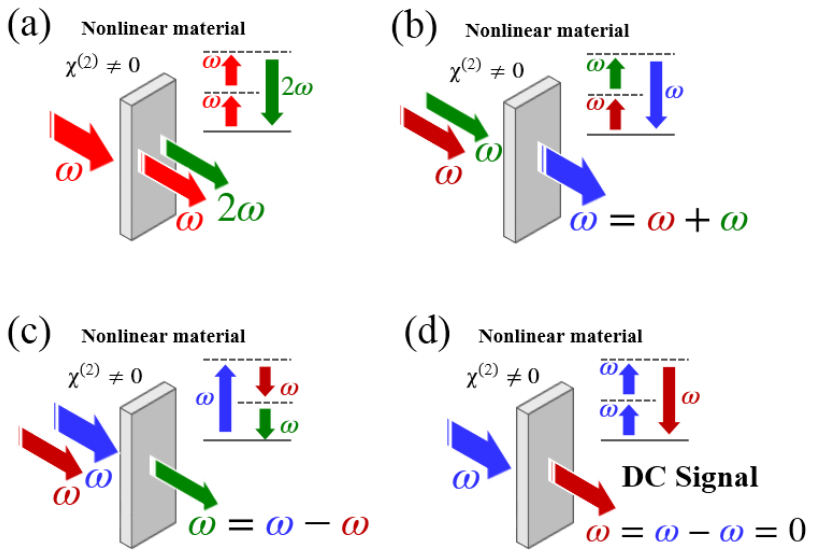

Source: The author (2025).

The next second-order nonlinear effect to be discussed is the ***sum-frequency generation (SFG)***. In SFG process, two photons of frequencies ω_1 and ω_2 are combined to generate a photon of frequency $\omega_3 = \omega_1 + \omega_2$, as illustrated in Figure A.7 (b). The bases of SFG is the term $P_i^{(\omega_3)}$ that appears in the nonlinear polarization due to the first term in equation (A.58) oscillating at the frequency $\omega_1 + \omega_2$. $P_i^{(\omega_3)}$ is given by:

$$P_i^{(\omega_3)} = \epsilon_0 \chi_{ijk}^{(2)} E_j(\omega_1) E_k(\omega_2). \tag{A.62}$$

Following similar procedure as for SHG, it is possible to deduce the phase matching condition for the SFG as [53 – 61]:

$$k(\omega_3) = k(\omega_1) + k(\omega_2). \tag{A.63}$$

SFG is a very interesting phenomenon and widely used in scientific and technological approaches. One can cite applications such as in surface and interface studies [66], biological imaging and spectroscopy [67], nonlinear optical microscopy [68], and frequency conversion for new laser sources [69].

The follow second-order effect originates from the second term in equation (A.58), where the wave generated oscillates in a component frequency that is the difference between the fundamental frequencies, that is, $\omega_3 = \omega_1 - \omega_2$. This effect is called ***difference-frequency***

generation (DFG). DFG has a myriad of technological applications such as terahertz (THz) wave generation [70], mid-infrared (Mid-IR) laser sources [71], quantum optics and photon generation [72], and coherent tunable laser sources in the far-IR and UV [73].

The basic geometrical configuration of DFG is showed in Figure A.7 (c). The second-order polarization component followed by the phase matching condition for DFG are [53 – 61]:

$$P_i^{(\omega_3)} = \epsilon_0 \chi_{ijk}^{(2)} E_j(\omega_1) E_k^*(\omega_2), \quad \text{and} \quad k(\omega_3) = k(\omega_1) - k(\omega_2). \tag{A.64}$$

An interesting second-order nonlinear polarization effect arises if we consider the component frequency $\omega_2 = -\omega_1$ in equation (A.58). Then, the expansion of the electric field product will be:

$$\boldsymbol{E}(t)\boldsymbol{E}(t) = 2\boldsymbol{E_1}\boldsymbol{E_2} + other\ oscillating\ terms. \tag{A.65}$$

The term $2\boldsymbol{E_1}\boldsymbol{E_2}$ mean that there is a field component oscillating a frequency $\omega = 0$. This term originates from the SFG term in equation (A.58) that ensures $\omega = \omega_1 + \omega_2 = 0$. The DFG term in equation (A.58) guarantees high-frequency components oscillating at the frequency $2\omega_1$ [53, 61]. This phenomenon is called ***optical rectification (OR)***, and creates a nonlinear static polarization (DC field) from the nonlinear mixing of frequencies ω_1 and $-\omega_1$. OR is essential in generating **terahertz radiation** in nonlinear crystals, as the DC field modulates at low frequencies [53]. Figure A.7 (d) exhibits the geometrical scheme to generates OR in a second-order nonlinear material.

An interesting aspect of the OR phenomenon is that the phase matching requirement is less stringent compared to other second-order nonlinear processes like SHG. The reason is that the DC field generated from OR is static (or very low frequency), reducing the sensitivity to small wave vector mismatches [53, 60]. However, achieving good phase matching improves the efficiency of THz radiation generation, which is often a goal in OR applications. Good phase matching is important to guarantee that the electric field constructively interfere with itself as it propagates through the coherent length of the nonlinear material [60]. The phase match condition for the OR generation is [53]:

$$k_{DC} = k(\omega) - k(-\omega) = 0. \tag{A.66}$$

This section definitively introduces the fundamental concepts of second-order nonlinear effects that arise in non-centrosymmetric materials. These effects play a crucial role in numerous scientific and technological applications, such as the implementation of second SHG

for innovative laser sources and the generation of terahertz (THz) radiation via OR. Table A.4 explicitly summarizes the second-order nonlinear effects covered in this section, clearly outlining their phase matching requirements and key optical applications.

Table A.4 – Second-order nonlinear effects, polarization expressions, and respective phase match requirements.

Second-order Effect	**Polarization Expression**	**Phase Matching Condition**	**Applications**
SHG	$P_i^{(2\omega)} = \epsilon_0 \chi_{ijk}^{(2)} E_j^{(\omega)} E_k^{(\omega)}$	$k(2\omega) = 2k(\omega)$	Laser frequency doubling
SFG	$P_i^{(\omega_3)} = \epsilon_0 \chi_{ijk}^{(2)} E_j^{(\omega_1)} E_k^{(\omega_2)}$	$k(\omega_3) = k(\omega_1) + k(\omega_2)$	Nonlinear microscopy, signal upconversion
DFG	$P_i^{(\omega_3)} = \epsilon_0 \chi_{ijk}^{(2)} E_j^{(\omega_1)} \quad E_k^{(\omega_2)\ *}$	$k(\omega_3) = k(\omega_1) - k(\omega_2)$	Tunable Mir-IR sources
OR	$P_i^{(0)} = \epsilon_0 \chi_{ijk}^{(2)} E_j^{(\omega)} \quad E_k^{(-\omega)\ *}$	$k_{DC} = k(\omega) - k(-\omega) = 0$	Terahertz radiation generation

Source: The author (2025).

It is worth mentioning that all the second-order effects discussed in this section are ***parametric process***. In optics, a nonlinear optical light-matter interaction in which energy and momentum conservation (phase matching) govern the energy exchange between light waves without a net transfer of energy to or from the medium is considered parametric [63]. The term "parametric" implies that the process is governed by the intrinsic parameters of the medium, such as the nonlinear susceptibility $\chi^{(2)}$ [54]. Parametric process does not involve the absorption of photons by the medium nor changes in the internal energy states of the medium. In parametric processes, the medium remains "transparent" in the sense that no material transitions occur, and the photon energies are redistributed among interacting waves according to the nonlinear interaction [53 – 70].

In summary, second-order nonlinear optical effects such as SHG, SFG, DFG, and optical rectification (OR) demonstrate the profound ability of non-centrosymmetric materials to generate new frequencies and manipulate light. These effects, enabled by the inherent asymmetry of the material's second-order susceptibility tensor, have opened doors to numerous scientific and technological advances, from frequency conversion to terahertz generation. However, when a material possess the centrosymmetry property, the second-order nonlinear susceptibility vanishes, and third-order nonlinear effects become dominant.

The following section will focus on the third-order nonlinearities, highlighting key phenomena such as self-focusing, self-phase modulation, and third-harmonic generation. These effects manifest in both centrosymmetric and non-centrosymmetric materials, and they unequivocally demand higher light intensities for their occurrence because of modulus-squared dependence of the electric field, as will be shown.

A.2.3 Third-order Effects and Centrosymmetric Mediums

The third-order nonlinear polarization, $\boldsymbol{P}^{(3)}$, arises due to intense optical fields and is fundamental to numerous nonlinear optical effects. These effects are critical in advanced optical technologies, particularly in high-intensity laser systems and ultrafast optics. This section will establish the development of the fundamental theoretical treatment to these new phenomena based on standard and contemporary literature, besides bringing to the reader scientific and technological applications regarding third-order effects.

The mathematical formulation of third-order effects relies on the nonlinear polarization term given by equation (A.53), that we can explicitly rewrite as:

$$P_i^{(3)}(t) = \epsilon_0 \sum_{jkl} \chi_{ijkl}^{(3)} E_j(t) E_k(t) E_l(t), \tag{A.67}$$

where $\chi_{ijkl}^{(3)}$ is the third-order susceptibility tensor and $E_j(t)$ are the electric field components. $\chi_{ijkl}^{(3)}$ is a rank-four tensor and has 81 possible nonzero elements; however, symmetry often reduces this number significantly, especially for centrosymmetric materials [53].

In isotropic media (e.g., glasses), $\chi_{ijkl}^{(3)}$ reduces significantly due to permutation symmetry among the indices i,j,k. This symmetry guarantees that $\chi_{ijkl}^{(3)} = \chi_{ikjl}^{(3)} = \chi_{iljk}^{(3)}$, reducing the number of independent elements to 30, and then the polarization becomes [53 – 63]:

$$P^{(3)}(t) \propto \chi^{(3)} |E(t)|^2 E(t). \tag{A.68}$$

The $|E(t)|^2$ term indicates that the nonlinear interaction depends on the intensity of the field, leading to intensity-dependent effects [70].

Third-order nonlinear optics deals with some key phenomenon, such as the ***optical Kerr effect***. In a Kerr medium, an intensity-dependent refractive index causes a light beam to focus due to higher refractive index in the beam's center. This effect appears due to a third-order nonlinear correction in the material's refractive index as [53 – 70]:

$$n = n_0 + n_2 I, \tag{A.69}$$

where n_0 is the linear refractive index (as defined in section A.1), $I \propto |E(t)|^2$ is the electric field intensity, and n_2 is the third-order nonlinear refraction index. The subscript 2 indicates a quadratic dependence on the amplitude of the field $E(t)$, which implies a linear dependence on I. In this notation, the refractive nonlinearity of order N is represented by a n_{N-1} coefficient. Notice that the term $n_2 I$ accounts for the intensity-dependent refractive index effect. If $n_2 > 0$, then the medium exhibits a ***self-focusing*** effect, while $n_2 < 0$ leads to a ***self-defocusing*** effect [70]. For a self-focusing medium, when a high-intensity beam propagates through it, the intensity is highest at the center of the beam and decreases radially outward. As a result, the total refractive index is higher at the center than at the edges, creating a lens-like effect known as a positive nonlinear lens. This causes the light to bend toward the region of higher refractive index, effectively focusing the beam [53 – 70].

The mathematical description of the self-focusing phenomenon is described by the spatial nonlinear Schrödinger equation, which governs the propagation of light in a nonlinear medium [53 – 70]:

$$\frac{\partial A}{\partial z} + \frac{i}{2k}\nabla_{\perp}^2 A + i\frac{n_2 k}{n_0}|A|^2 A = 0, \tag{A.70}$$

where, A is the complex electric field amplitude, z is the propagation distance, $\nabla_{\perp}^2$ is the transverse Laplacian component, and k is the wave vector ($k = 2\pi n_0/\lambda$). The term $\frac{n_2 k}{n_0}|A|^2$ represents the nonlinear phase shift induced by the intensity-dependent refractive index [54]. In equation (A.70), is consider the **slowly varying envelop approximation** (SVEA). SVEA considers that A changes slowly over distances comparable to the wavelength λ and time scales of the optical period ($T = 2\pi/\omega$), then higher-order z-derivatives are neglected [53]. Additionally, the **paraxial approximation** is also taking into account, as a result, is assumed that the beam divergence is small, meaning that the propagation is predominantly along the z-axis, with only gradual spreading in the transverse x- and y-directions. Consequently, the parallel Laplacian component in equation (A.70) is consider as $\nabla_{\parallel}^2 \approx 0$ [53, 61].

However, the self-focusing effect it is only achieved if the beam's power exceeds a critical threshold known as the **critical power for self-focusing** (P_C). From equation (A.70), it is possible to deduce this power threshold as [71]:

$$P_C = \xi\frac{\lambda_0^2}{8\pi n_0 n_2}, \tag{A.71}$$

where λ_0 is the wavelength of light and ξ is a dimensionless constant that depends on the beam profile (e.g., Gaussian, flat-top, etc.), and may vary slightly depending on the specific intensity profile of the beam or the boundary conditions. For a Gaussian-like beam profile $\xi = 3.77$ [71]. Physically, the critical power, P_C, is the threshold above which self-focusing dominates beam propagation in a nonlinear medium. Below P_C, diffraction tends to dominate and prevents catastrophic collapse [71]. In this scenario P_C describes the beam propagation in a nonlinear medium, where self-focusing occurs due to the intensity-dependent refractive index. Consequently, the beam width w as a function of the propagation distance z is [71]:

$$w(z) = w_0 \left(1 - \frac{P}{P_C} + \left(\frac{z}{z_R}\right)^2\right)^{1/2}, \tag{A.72}$$

where w_0 is the beam waist at the focal point (minimum width), P is the actual power of the beam, and the term $1 - \frac{P}{P_C}$ accounts for the self-focusing effect. $z_R = \pi w_0^2/\lambda_0$ is the Rayleigh range, and term $(z/z_R)^2$accounts for the beam diffraction as usual.

The Figure A.8 illustrates the self-focusing effect in a third-order nonlinear medium by showing the intensity profile of a Gaussian-like beam as it propagates, the refractive index as a function of radial distance from the beam center, and the evolution of beam width at various powers relative to the critical power P_C. Figure A.8 (a), is the 3-dimensional representation of how the intensity distribution evolves as the beam propagates through the nonlinear medium following the intensity relation: $I(z) = I_0 \exp\left[-2r^2/\left(w(z)\right)^2\right]$, where $r = \sqrt{x^2 + y^2}$ is the radial distance, and $w(z)$ is computed for the case $P < P_C$. Figure A.8 (b), shows how the total refractive index (equation (A.69)) changes radially due to the intensity-dependent effect. Figure A.8 (c) depicts the variation in beam width for different powers relative to the critical power (equation (A.72)). Notice that, when $P < P_C$ the beam behaves similarly to the linear case but diverges more slowly. When $P = P_C$, $w(z)$ goes linearly with z and the beam remains collimated because self-focusing perfectly balances diffraction (orange curve in Figure A.8 (c)). However, when $P > P_C$, the term $1 - \frac{P}{P_C}$ becomes negative, as a result $w(z)$ to decrease sharply, leading to beam collapse (self-focusing). Then, equation (A.72) becomes invalid for z values near collapse due to the square root of a negative number (see the green curve in Figure A.8 (c)).

Figure A.8 – Self-focusing effect in a third-order nonlinear material. (a) Beam propagation in a nonlinear medium, (b) refractive index profile, and (c) beam width dependence with the propagation distance. The parameters used for the beam and the medium were: $\lambda_0 = 800$ nm, $n_0 = 1.5$, $n_2 = 3 \times 10^{-20}\text{m}^2/\text{W}$, $I_0 = 1 \times 10^{13}\text{W/m}^2$, and $w_0 = 1 \times 10^{-3}\text{m}$.

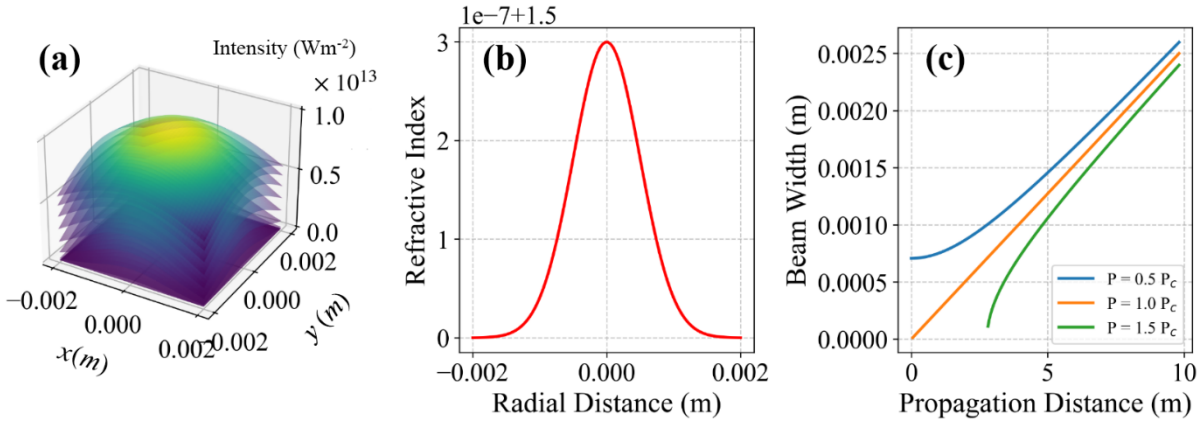

Source: The author (2025).

Self-focusing is an important phenomenon with various physical implications. As discussed, when the power of a beam significantly exceeds a certain threshold, it can experience catastrophic collapse, resulting in a drastic increase in intensity at the focal point. Another consequence of self-focusing is self-phase modulation. This effect causes a self-induced phase change due to the intensity-dependent refractive index, which leads to the spectral broadening of the beam [61]. In real-world scenarios, other physical mechanisms, such as plasma generation and higher-order nonlinearities, can counteract beam collapse, resulting in the formation of stable light filaments [71]. Moreover, the self-focusing phenomenon is used in various fields, including high-intensity laser applications for damage control [54], nonlinear microscopy to enhance resolution and contrast in imaging techniques [72], and filamentation, which allows for the long-range propagation of laser beams through the atmosphere for applications such as LIDAR and remote sensing [73].

Another interesting phenomenon related to the optical Kerr effect is **self-phase modulation (SPM)**. Similar to the self-focusing effect, SPM occurs due to the intensity-dependent refractive index of a medium. When light travels through this medium, the high-intensity areas of the beam cause a local change in the refractive index. This result in a phase shift that varies over time as the light propagates [53, 54]:

$$\Delta\phi \propto n_2 I(z,t), \tag{A.73}$$

where as usual z is the propagation distance. For SPM, the temporal aspect is relevant and equation (A.73) results in a frequency modulation across the pulse's temporal profile, leading

to spectral broadening [53]. Unlike processes that involve transferring energy to different frequencies, SPM redistributes existing energy across a broader spectrum [70]. This phenomenon is crucial in ultrafast optics, particularly in generating supercontinuum light and shaping ultrashort pulses [74, 75]. For instance, in optical fibers, SPM is often used to create broadband sources for applications in spectroscopy and microscopy [63, 76]. Figure A.9 (a), illustrate the appearance of new optical frequencies due to the SPM effect in a Kerr medium.

SPM deals with the temporal domain of the nonlinear phase shift cause by a Kerr medium. However, notice from equation (A.73), that should exist a spatial counterpart of this effect, that is, a **spatial self-phase modulation (SSPM)**. Indeed, SSPM is the spatial counterpart to temporal SPM, where the intensity profile of a laser beam induces spatially varying phase shifts in a nonlinear Kerr medium. Unlike SPM, which results in spectral broadening over time, SSPM manifests as spatially distinct patterns, such as concentric rings, due to the Kerr effect [53, 63] (see Figure A.9 (b)). These patterns are often observed when a beam passes through materials like liquid crystals or photorefractive media and are viewed through crossed polarizers to enhance visibility [77]. SSPM has practical applications in various fields. For example, it is used in nonlinear optics to measure the nonlinear refractive index (n_2) of materials, aiding in characterizing optical media [78]. In laser beam diagnostics, SSPM provides insights into beam intensity profiles and nonlinear effects [79]. Additionally, SSPM plays a role in beam shaping and optical switching technologies, where spatial modulation of light is crucial for developing advanced all-optical devices [63, 79, and 80]. This phenomenon complements SPM by offering a spatial perspective on the third-order nonlinear interactions of light with matter.

Optical Kerr media, when subjected to high-intensity excitation, can generate another crucial phenomenon: **third-harmonic generation (THG)**. THG is a coherent frequency-conversion process in which three photons at the fundamental frequency (ω) combine to generate a single photon at three times the frequency (3ω). THG is a third-order nonlinear process and is mediated by the material's third-order susceptibility, $\chi^{(3)}$, and its efficiency is highly dependent on phase-matching conditions [53, 54]. THG often occurs at interfaces or boundaries where symmetry is broken, as bulk centrosymmetric materials, typically suppress even-order nonlinearities [53, 54, and 81]. In practical applications, THG is widely used in nonlinear microscopy to image interfaces and boundaries within biological samples without the need for external labeling [82]. Its sensitivity to material structure also makes it a powerful tool

for studying nonlinear properties of materials. Figure A.9 (c), shows schematically how the THG process could be generated in a nonlinear material with $\chi^{(3)} \neq 0$.

Figure A.9 – Representation of third-order nonlinear effects. (a) Self-phase modulation (SPM), (b) Spatial self-phase modulation (SSPM), and (c) third-harmonic generation (THG). The inset in (c) represents the energy level diagram of the THG.

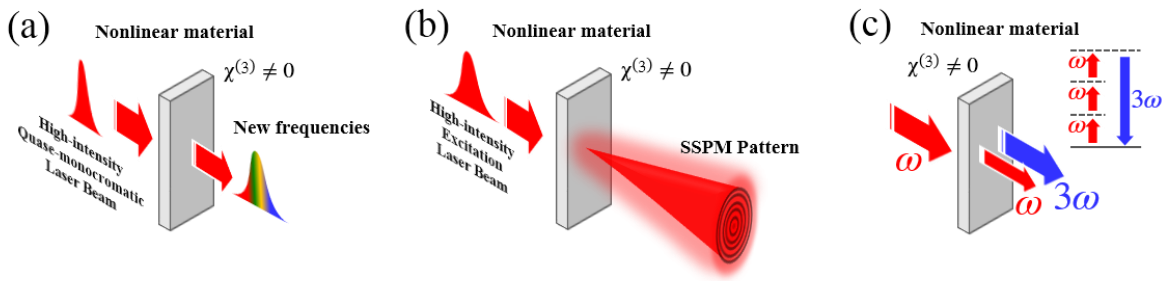

Source: The author (2025).

It is important to highlight the differences in energy dynamics among the third-order processes discussed so far. Self-focusing concentrates energy by narrowing the beam waist, whereas SPM redistributes energy within the existing spectrum. In contrast, SSPM redistributes energy spatially across the beam profile. For THG, energy is transferred to the 3ω component. These distinct effects enable unique applications: SPM drives advancements in ultrafast optics, such as supercontinuum generation and pulse compression; SSPM is crucial for beam shaping and nonlinear material diagnostics; self-focusing supports processes like laser filamentation and high-intensity beam control; and THG facilitates frequency conversion and high-resolution microscopy.

These third-order nonlinear processes commonly occur in materials with centrosymmetric properties, meaning that the material's structure remains unchanged under inversion through a central point. In simpler terms, for every point (x, y, z) in the material, there is a corresponding point $(-x, -y, -z)$ with identical properties [53, 54]. This inversion symmetry imposes strict limitations on the material's nonlinear optical behavior. Specifically, in centrosymmetric media, the second-order nonlinear susceptibility $\chi^{(2)}$ vanishes because second-order nonlinear processes, such as second-harmonic generation (SHG), require a break in inversion symmetry, which these materials lack [63]. Consequently, only odd-order nonlinearities, such as those governed by the third-order susceptibility, $\chi^{(3)}$, can manifest. Therefore, in centrosymmetric materials, the first nonlinear contribution to the polarization

tensor is the third-order term, which enables effects like self-phase modulation and third-harmonic generation as discussed in this section.

In summary, SPM, SSPM, self-focusing, and THG are fundamental third-order nonlinear optical effects with distinct mechanisms and technological relevance. Together, they illustrate the diversity of nonlinear optics, emphasizing the importance of third-order nonlinearities in advancing both fundamental research and practical applications across fields such as ultrafast optics, imaging, and beam manipulation.

In the next subsection, we will examine two fundamental phenomena in Kerr media: third-order nonlinear absorption and third-order nonlinear refraction.

A.2.3.1 Third-order nonlinear absorption and refraction

Third-order nonlinear optical effects play a crucial role in understanding the interaction of intense light with matter, particularly in materials exhibiting the Kerr effect. Among these effects, third-order nonlinear absorption and refraction are two key phenomena that arise due to the material's third-order susceptibility, $\chi^{(3)}$ [53]. Nonlinear absorption, such as two-photon absorption (2PA) or saturable absorption (SA), involves the simultaneous absorption of multiple photons, enabling applications in optical limiting and ultrafast laser dynamics [63]. Nonlinear refraction, on the other hand, manifests as an intensity-dependent change in the refractive index, giving rise to effects like self-focusing, self-phase modulation, and optical soliton formation [83]. Together, these third-order nonlinear processes are essential for advancing technologies in ultrafast optics, laser-material interactions, and photonic device engineering.

In this section, we will focus on developing the theory to extract analytical expressions for the third-order nonlinear coefficients related to two-photon absorption (2PA) and the refractive phenomenon, highlighting some fundamental scientific and technological applications.

Third-order nonlinear absorption describes how the intensity-dependent absorption coefficient alters light propagation, primarily through **two-photon absorption (TPA)** and higher-order multiphoton absorption. In a medium with nonlinear absorption, the intensity inside the material $I(z)$ evolves according to the Beer-Lambert law modified to include nonlinear terms [83]:

$$\frac{dI}{dz} = -\alpha_0 I - \alpha_2 I^2 - \alpha_4 I^3 - \alpha_6 I^4 - \cdots . \tag{A.74}$$

In equation (A.74) only odd-terms of the polarization tensor are considered. Consequently, the absorption coefficients indexes are denoted as α_{N-1}, with N representing the nonlinear odd-order of the term. Thus, for a third-order absorptive effect, the relevant coefficient becomes α_2, predominantly resulting in a 2PA effect if the material is excited off-resonance with at least twice of the energy necessary to promote its electrons to an upper state.

Considering the third-order nonlinear term as the first correction for the polarization tensor (see equation (A.54)), the total polarization of a material can be written as:

$$\begin{aligned} \boldsymbol{P} &= \boldsymbol{P}^{(1)} + \boldsymbol{P}^{(3)} \\ &= \epsilon_0 \chi^{(1)} \boldsymbol{E} + \epsilon_0 \chi^{(3)} \vdots \boldsymbol{EEE}. \end{aligned} \tag{A.75}$$

For simplicity, we assume a monochromatic plane wave propagating along the z-direction with the field pointing in the x-direction in an isotropic medium. Consequently, a tensor contraction averaging over all the polarization states is performed and the third-order polarization can be written as: $\boldsymbol{P}^{(3)} = \frac{3}{4}\chi^{(3)}|\boldsymbol{E}|^2\boldsymbol{E}$, where $\chi^{(3)} = \chi^{(3)}_{1111}$ now is a scalar quantity [83]. Thus, the total polarization for a third-order correction can be rewrite as:

$$\boldsymbol{P} = \epsilon_0 \chi^{(1)} \boldsymbol{E} + \frac{3}{4}\epsilon_0 \chi^{(3)} |\boldsymbol{E}|^2 \boldsymbol{E}. \tag{A.76}$$

We can apply the spatial nonlinear Schrödinger equation (see equation (A.70)) to describe how the electric field $\boldsymbol{E}$ evolves inside the nonlinear material:

$$2i\frac{dE}{dz}e^{ikz} = -\omega^2 \mu_0 \boldsymbol{P}. \tag{A.77}$$

Moreover, we applied the SVEA and paraxial approximations, neglecting diffraction effects, which implies that the term $\nabla_\perp^2 E \approx 0$ in equation (A.70). Notice that equation (A.77) is scalar because the fields are oriented along the x-direction. We can assume that for the excitation frequency ω the medium has no linear absorption contribution, consequently, the losses will be only due to the 2PA process. This means that we can neglect the first-order term in equation (A.76). Thus, one can rewrite the wave equation (A.77) as follows:

$$2i\frac{dE}{dz}e^{ikz} = -\frac{3}{4}\epsilon_0 \mu_0 \omega^2 \chi^{(3)} |E|^2 E. \tag{A.78}$$

The complex amplitude of the electric field spatially evolves inside the material as: $E(z) = u(z)e^{i\phi(z)}$, where $u(z)$ the field amplitude and $\phi(z)$ is the total phase-shift due to the propagation inside the medium [83, 84]. In addition, we can explicitly separate the third-order susceptibility $\chi^{(3)}$ into its real and imaginary parts as: $\chi^{(3)} = \mathrm{Re}\left(\chi^{(3)}\right) + i\mathrm{Im}\left(\chi^{(3)}\right)$.

Consequently, equation (A.78) is separated into two uncoupled differential equations for the amplitude and phase evolutions inside the medium as [83]:

$$\frac{du}{dz} = -\frac{3\omega}{8n_0c}\mathrm{Im}\left(\chi^{(3)}\right)u^3, \tag{A.79}$$

and

$$\frac{d\phi}{dz} = \frac{3\omega}{8n_0c}\mathrm{Re}\left(\chi^{(3)}\right)u^2. \tag{A.80}$$

n_0 is the linear refractive index for a nonmagnetic material as defined in section A.1.2 . The average intensity in one optical cycle varies in terms of the electric field amplitude as: $I = \frac{1}{2}n_0c\epsilon_0|u|^2$. Thus, it is possible to rewrite equation (A.79) in terms of the optical intensity as follows:

$$\frac{dI}{dz} = -\frac{3\omega}{2\epsilon_0 n_0^2 c^2}\mathrm{Im}\left(\chi^{(3)}\right)\cdot I^2 . \tag{A.81}$$

By comparing equation (A.81) with equation (A.74) for a pure third-order correction, one can determine the 2PA coefficient as:

$$\alpha_2 = \frac{3\omega}{2n_0^2c^2\epsilon_0}\mathrm{Im}\left(\chi^{(3)}\right). \tag{0.1}$$

Measuring the 2PA coefficient α_2, and consequently, the imaginary part of $\chi^{(3)}$, is crucial for materials' characterization aiming applications in optical limiting, biomedical imaging, photodynamic therapy, and ultrafast photonics. Materials with strong 2PA enable optical limiters for sensor protection, multiphoton microscopy for deep tissue imaging, and nonlinear optical devices for high-speed photonics [85, 86]. Several experimental techniques exist to determine α_2, with the **Z-scan method** being one of the most widely used due to its simplicity and sensitivity. In this technique, a sample is moved along the focus of a Gaussian laser beam, and the transmitted intensity is analyzed; a dip in open-aperture z-scan measurements indicates nonlinear absorption [53, 85]. Other techniques include pump-probe spectroscopy, which provides ultrafast carrier dynamics [87], and two-photon excited fluorescence (TPEF), which is valuable for biological imaging and molecular studies [88]. Advancing 2PA measurements contributes to the development of high-performance nonlinear materials for photonic and biomedical technologies.

By solving equation (A.80), we can determine the nonlinear perturbative phase shift $\Delta\phi$ caused due to the third-order polarization contribution in a distance Δz as:

$$\Delta\phi = \frac{3\omega}{8n_0c}\mathrm{Re}\left(\chi^{(3)}\right)u^2\Delta z. \tag{A.83}$$

In a linear medium, the phase shift $\phi^{(L)}$ caused by a wave that travel a distance Δz is [83]:

$$\phi^{(L)} = \frac{\omega}{c} n_0 \Delta z. \tag{A.84}$$

Then, the total phase shift can be expressed as follows:

$$\phi = \phi^{(L)} + \Delta\phi = \frac{\omega}{c}\left(n_0 + \frac{3\omega}{8n_0 c}\mathrm{Re}\left(\chi^{(3)}\right)u^2\right)\Delta z. \tag{A.85}$$

Notice that the third-order refractive contribution is expressed as a perturbation in the linear response. By rewriting equation (A.85) in terms of the optical intensity $\left(I = \frac{1}{2} n_0 c \epsilon_0 |u|^2\right)$ and comparing with equation (A.69), one can determine an expression for the third-order nonlinear refractive index coefficient as:

$$n_2 = \frac{3\omega}{4n_0^2 c\epsilon_0}\mathrm{Re}\left(\chi^{(3)}\right). \tag{A.86}$$

In conclusion, third-order nonlinear refraction, characterized by the nonlinear refractive index n_2, plays a important role in advancing modern photonic technologies. Its applications span across optical limiting, all-optical switching, and ultrafast signal processing, enabling the development of next-generation communication and computing systems [53]. There are diverse experimental techniques to measure the n_2 correction of nonlinear mediums, such as four-wave mixing and interferometric methods [53, 85]. However, the z-scan technique is the widely adopted method for measuring n_2 due to its high sensitivity and simplicity, while other advanced techniques [85]. Research continues to refine these measurement approaches, and the potential for harnessing third-order nonlinearities in emerging technologies, including integrated photonics and quantum optics, becomes increasingly promising [89].

In the following section, we will briefly discuss absorptive and refractive higher-order effects in nonlinear materials, along with presenting some new evidence regarding these phenomena.

A.2.4 Higher-order Effects

The study of higher-order nonlinear terms in the polarization expansion provides profound insights into complex light-matter interactions that extend beyond the well-known second- and third-order effects. These higher-order terms, represented by $\chi^{(n)}$ for $n \geq 4$, become significant at extremely high intensities or in materials with engineered nonlinearities, enabling phenomena such as fifth-harmonic generation, multiphoton absorption, and cascaded nonlinear processes [53]. While these effects are often weaker compared to lower-order

contributions, they play a critical role in advanced applications, including high-resolution imaging, ultrafast laser systems, and the generation of extreme ultraviolet (EUV) and X-ray frequencies [90]. Techniques such as high-harmonic generation (HHG) and nonlinear spectroscopy have been instrumental in probing these higher-order effects, revealing their potential for manipulating light at unprecedented scales [91]. Understanding and harnessing these higher-order nonlinearities not only deepens our knowledge of fundamental physics but also paves the way for breakthroughs in quantum optics, attosecond science, and nonlinear metamaterials [92].

This section aims to provide a brief overview of the unique characteristics, measurement challenges, and emerging applications of higher-order nonlinear processes, such as cascading processes and HHG. We emphasize the increasing significance of these processes in advanced photonic technologies. Additionally, we will present relevant and up-to-date literature on these phenomena for the reader's reference.

Let us starting discussing the fundamentals of cascade nonlinear process. A **cascade nonlinear process** occurs when multiple nonlinear optical interactions take place sequentially, leading to a chain of frequency conversions [53, 54, 63]. This happens when an initial nonlinear interaction generates a new frequency component, which then acts as a source for another nonlinear process. An excellent example of a material that can generate second-harmonic generation (SHG) and subsequently sum-frequency generation (SFG) through a cascade process is beta-barium borate (β-BBO). β-BBO is a widely used nonlinear optical crystal due to its large nonlinear coefficients, broad transparency range, and high damage threshold, making it ideal for frequency conversion processes [93].

In a typical cascade process, β-BBO first generates SHG when an intense fundamental beam at frequency ω interacts with the crystal, producing light at the second harmonic frequency 2ω. This occurs due to the $\chi^{(2)}$ nonlinearity of the crystal, which couples two photons of the fundamental frequency to create one photon at the second harmonic, as discussed in section A.2.2. Subsequently, the generated second harmonic (2ω) can interact with the remaining fundamental beam (ω) in the same crystal or a second β-BBO crystal, leading to SFG. This process results in the generation of light at the sum frequency 3ω, demonstrating the cascaded nature of the nonlinear interactions [94].].

(a), shows the energy level scheme of the cascade process that can happen in a β-BBO crystal. Such cascade processes are essential in applications like ultrafast pulse generation, wavelength

tuning, and coherent light sources for spectroscopy [94]. These processes are well-documented in standard literature, such as Nonlinear Optics by Robert W. Boyd, which provides a foundational understanding of cascaded second-order effects and their role in frequency conversion [53]. Additionally, Photonics: Optical Electronics in Modern Communications by Yariv and Yeh offers insights into the practical applications of cascaded processes in optical communication systems, including wavelength division multiplexing and all-optical signal processing [95].

Figure 10 – Higher-order nonlinear process energy diagrams. (a) Cascade second-order process and (b) fifth-order generation (FHG).

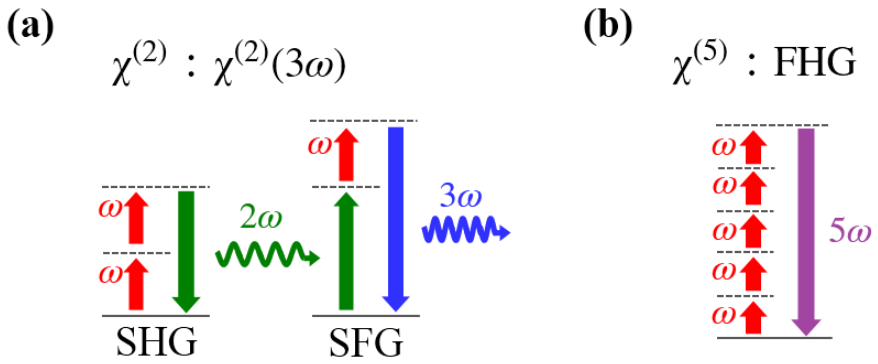

Source: The author (2025).

Recent advancements have expanded the scope of cascaded nonlinearities, particularly in the development of compact and efficient frequency converters. For instance, the use of periodically poled lithium niobate (PPLN) waveguides has enabled highly efficient cascaded SHG and SFG processes, paving the way for integrated photonic devices [96]. Furthermore, emerging research explores cascaded processes in nonlinear metasurfaces and 2D materials, such as graphene and transition metal dichalcogenides, which exhibit strong higher-order nonlinearities and enable novel applications in ultrafast optics and quantum light sources [97]. These developments highlight the transformative potential of cascaded nonlinear processes in advancing technologies ranging from telecommunications to quantum computing.

In a **higher-harmonic generation** (HHG) process, a nonlinear optical interaction occurs where intense laser light interacts with a medium, generating harmonics at integer multiples of the incident frequency (e.g., $2\omega, 3\omega, 4\omega, 5\omega, \ldots$). This phenomenon arises from the nonlinear polarization induced in the material, typically described by higher-order terms in the susceptibility tensor $\chi^{(n)}$ (see, for example, equation (A.51)). At high intensities, the electric field of the laser drives electrons in the medium to oscillate nonlinearly, leading to the emission

of coherent radiation at harmonic frequencies [53]. This effect is most commonly observed in gases, where ionization and recombination of electrons generate attosecond pulses, but it also occurs in solids and plasmas under specific conditions [90]. The physical mechanism can be understood through the three-step model: ionization, acceleration, and recombination, which explains the generation of high-energy photons [91]. For instance, in the theoretical work of N. Nishizawa, was derive wave equations for fifth-harmonic generation (FHG) in cubic centrosymmetric crystals in direct and indirect processes when an incident electric field propagates along a cubic axis [98]. Figure 10 (b), illustrates the energy diagram scheme for a direct FHG process in cubic centrosymmetric crystal.

HHG process has revolutionized fields such as attosecond science, enabling the study of ultrafast electron dynamics in atoms, molecules, and solids [99]. Additionally, HHG serves as a critical tool for producing coherent EUV and soft X-ray sources, which are essential for advanced imaging, lithography, and spectroscopy applications [100]. Recent advancements in HHG from solid-state materials and nanostructures further expand its potential for compact, tabletop light sources in quantum optics and photonic integrated circuits [101].

The objective of this section was briefly discuss nonlinear higher-order processes in nonlinear materials, with a focus on the cascade process and high-order harmonic generation (HHG), particularly emphasizing the fifth-order direct process, both of which are crucial for technological development. Additionally, we aim to provide the reader with some standard and up-to-date literature on this subject. For completeness, in the next section we will discuss nonlinear scattering, a fundamental nonlinear process that enables frequency generation through scattering.

A.2.5 Nonlinear Scattering

Nonlinear scattering encompasses a variety of optical phenomena where the interaction of light with a medium results in the generation of new frequencies or altered propagation directions due to nonlinear effects. Among these, hyper-Rayleigh scattering (HRS) stands out as a second-order nonlinear process that generates scattered light at the second harmonic frequency (2ω) of the incident beam [101]. Unlike SHG, which requires a non-centrosymmetric medium (see section A.2.2), HRS can occur in isotropic materials, including liquids and nanoparticles, making it a versatile tool for probing molecular and nanoscale structures [102]. The physical basis of HRS lies in the nonlinear polarization induced by the incident electric field, which drives dipole oscillations at the second harmonic frequency, leading to coherent

scattering [53]. This effect has found significant applications in characterizing the nonlinear optical properties of materials, such as molecular hyperpolarizabilities and the symmetry properties of nanoparticles [103]. Additionally, HRS is employed in biological imaging and sensing, where its sensitivity to local symmetry and environment provides unique insights into complex systems [104, 105].

This section focuses on the mathematical principles, measurement techniques, and technological applications of HRS, highlighting its role in advancing nonlinear optics and material science.

The HRS phenomenon is a second-order nonlinear optical process mathematically described through the nonlinear polarization tensor $\boldsymbol{P}^{(2)}$ as previously defined in equation (A.54). In the HRS process, the incident electric field $\boldsymbol{E}(\omega)$ induces a dipole moment oscillating at the second harmonic frequency 2ω, which radiates scattered light. The intensity of the scattered second harmonic light $I_{2\omega}$ is proportional to the square of the induced nonlinear polarization:

$$I_{2\omega} \propto \left|\boldsymbol{P}^{(2)}\right|^2. \tag{A.87}$$

For an isotropic medium or a suspension of nanoparticles, the second-order susceptibility $\chi^{(2)}$ is averaged over all orientations, leading to a dependence on the **molecular hyperpolarizability** β, which describes the second-order nonlinear response of individual molecules or particles [53]. Then, the scattered intensity can be expressed as:

$$I_{2\omega} \propto N \ \beta^2 \ I_{\omega}^2, \tag{A.88}$$

where N is the number density of scatterers, $\langle\beta^2\rangle$ is the orientationally averaged square of the hyperpolarizability, and I_{ω} is the intensity of the incident light at frequency ω [102]. The angular distribution of the scattered light depends on the scattering geometry and the symmetry of the scatterers, with HRS typically being observed in a direction perpendicular to the incident beam to minimize background signals [101].

The measurement of HRS involves detecting the scattered second harmonic light and analyzing its intensity and polarization properties. This allows for the determination of the hyperpolarizability β, which provides insights into the molecular structure and symmetry of the scatterers [106]. HRS is particularly useful for studying systems where traditional SHG is not feasible, such as isotropic liquids or randomly oriented nanoparticles, making it a powerful tool for characterizing nonlinear optical materials and biological systems [107, 108].

In the work by C. N. Prasad and D. J. Williams titled “Introduction to Nonlinear Optical Effects in Molecules and Polymers”, readers can find comprehensive theoretical foundations and general principles of HRS. This book provides a strong background on nonlinear optics and molecular hyperpolarizabilities and is cited as a reference [108]. For detailed examples of optical setups and experimental techniques used to measure HRS signals, refer to the seminal paper by K. Clays and A. Persoons, reference [103]. This work clearly describes the experimental setup for measuring HRS signals, which includes using a focused laser beam, detecting at 90 degrees to the incident beam to minimize background noise, and calibrating the system with reference materials. The paper also discusses applications of HRS in characterizing molecular hyperpolarizabilities and the nonlinear optical properties of materials [103]. Additionally, for further details on experimental setups, references [105], [109], and [110] offer examples of optical configurations used in practice.

This section concludes the discussion on light-matter interaction in the nonlinear regime. The aim was to explore the fundamental aspects of phenomena that occur when higher-order terms of the polarization tensor become significant, with a focus on second- and third-order nonlinearities. The goal was to present the essential mathematical concepts related to these phenomena, highlight their technological applications, and provide up-to-date literature for further study.

References

[1] NSRDB. **Nrel.gov**, 2024. Disponível em: <https://nsrdb.nrel.gov/>. Acesso em: 30 dez. 2024.

[2] Solar Irradiance | Sun Climate. **Nasa.gov**, 26 jul. 2018. Disponível em: <https://sunclimate.gsfc.nasa.gov/article/solar-irradiance>. Acesso em: 30 dez. 2024.

[3] TOMIĆ, S.; DRESSEL, M. Ferroelectricity in molecular solids: a review of electrodynamic properties. **Reports on Progress in Physics**, 27 jul. 2015. v. 78, n. 9, p. 096501–096501.

[4] QIAN, W.; WU, H.; YANG, Y. Ferroelectric $BaTiO_3$ Based Multi-Effects Coupled Materials and Devices. **Advanced Electronic Materials**, 23 jun. 2022. v. 8, n. 10.

[5] KINGON, A. I.; SRINIVASAN, S. Lead zirconate titanate thin films directly on copper electrodes for ferroelectric, dielectric and piezoelectric applications. **Nature Materials**, 20 fev. 2005. v. 4, n. 3, p. 233–237.

[6] TRESSLER, J. F.; ALKOY, S.; NEWNHAM, R. E. Piezoelectric Sensors and Sensor Materials. **Journal of Electroceramics**, 1 dez. 1998. v. 2, n. 4, p. 257–272.

[7] GRIFFITS, David J. Introduction to Electrodynamics. In: **Electromagnetic waves in matter**. Prentice-Hall, 3rd edition, 1999.

[8] JACKSON, John D. Classical Electrodynamics. **John & Widely Sons**, 3dr edition, 1998.

[9] Brewster, Sir David (1781–1868), natural philosopher and academic administrator. **Oxford Dictionary of National Biography**, 2024. Disponível em: <https://www.oxforddnb.com/display/10.1093/ref:odnb/9780198614128.001.0001/odnb-9780198614128-e-3371>. Acesso em: 30 dez. 2024.

[10] BREWSTER, D. IX. On the laws which regulate the polarisation of light by reflexion from transparent bodies. By David Brewster, LL. D. F. R. S. Edin. and F. S. A. Edin. In a letter addressed to Right Hon. Sir Joseph Banks, Bart. K. B. P. R. S. **Philosophical Transactions of the Royal Society of London**, 31 dez. 1815. v. 105, p. 125–159. Disponível em: <https://royalsocietypublishing.org/doi/epdf/10.1098/rstl.1815.0010>. Acesso em: 30 dez. 2024.

[11] TO, C. angle of incidence for which all reflected light will be polarized. **Wikipedia.org**, 25 fev.2002.Disponívelem:<https://en.wikipedia.org/w/index.php?title=Brewster%27s_angle&oldid=1263116260>. Acesso em: 30 dez. 2024.

[12] DR. RÜDIGER PASCHOTTA. Brewster's angle. **Rp-photonics.com**, 4 out. 2024. Disponível em: <https://www.rp-photonics.com/brewster_s_angle.html>. Acesso em: 30 dez. 2024.

[13] KANDAMMATHE VALIYAVEEDU SREEKANTH *et al.* Generalized Brewster Angle Effect in Thin-Film Optical Absorbers and Its Application for Graphene Hydrogen Sensing. **ACS Photonics**, 18 jun. 2019. v. 6, n. 7, p. 1610–1617.

[14] DAEAR, W.; MAHADEO, M.; PRENNER, E. J. Applications of Brewster angle microscopy from biological materials to biological systems. **Biochimica et Biophysica Acta (BBA) - Biomembranes**, out. 2017. v. 1859, n. 10, p. 1749–1766.

[15] SALAMA, R.; ALTRJMAN, C.; ALTURJMAN, S. A Review on Long-Distance Optical Fiber Communication. **NEU Journal for Artificial Intelligence and Internet of Things**, 12 nov. 2024. v. 4, n. 2.

[16] DODSON, J. S. The Brilliance, Sparkliness and Fire of Several Diamond Simulants. **Optica Acta: International Journal of Optics**, ago. 1978. v. 25, n. 8, p. 701–705.

[17] EDUCATION, N. Basic Optics and Optical Instruments: Revised Edition. **Courier Corporation**, 2013.

[18] MCCARTHY, T. C. Introduction and History of Endoscopy. Em: MCCARTHY, T. C. (Org.). **Veterinary Endoscopy for the Small Animal Practitioner**. 1. ed. Wiley, 2021, p. 1–7.

[19] TO, C. equations of light transmission and reflection. **Wikipedia.org**, 9 out. 2001. Disponívelem:<https://en.wikipedia.org/w/index.php?title=Fresnel_equations&oldid=1264507826>. Acesso em: 30 dez. 2024.

[20] HECHT, Eugene. Optics. **Addison Wesley** 4th edition, 2002.

[21] QIN, M.; ZHANG, L.; WU, H. Dielectric Loss Mechanism in Electromagnetic Wave Absorbing Materials. **Advanced Science**, 2022. v. 9, n. 10, p. 2105553.

[22] DHALIA, T.; JUNEJA, R.; DAS, A. Enhanced near-complete absorption of electromagnetic waves by dual resonance in a magnetized plasma. **arXiv.org**, 2024. Disponível em: <https://arxiv.org/abs/2403.04462>. Acesso em: 30 dez. 2024.

[23] DU, Y. *et al*. Research progress and future perspectives on electromagnetic wave absorption of fibrous materials. **iScience**, 11 set. 2023. v. 26, n. 10, p. 107873.

[24] BORN, M.; WOLF E. Principles of optics: Electromagnetic theory of propagation, interference, and diffraction of light. **Cambridge university press**. 7th edition, 1999.

[25] WANGSNESS, Roald K. Electromagnetic fields. Vol. 2. **New York: Wiley**, 1979.

[26] PALIK, Edward D., ed. Handbook of optical constants of solids. Vol. 3. **Academic press**, 1998.

[27] LIDE, David R., ed. CRC handbook of chemistry and physics. Vol. 85. **CRC press**, 2004.

[28] JORDAN, Edward Conrad. Electromagnetic waves and radiating systems. **Prentice-Hall**, 1958.

[29] FOX, Mark. Optical properties of solids. Vol. 3. **Oxford university press**, 2001.

[30] BUBE, Richard H. Photovoltaic materials. Vol. 1. **World Scientific**, 1998.

[31] LUQUE, Antonio; STEVEN, Hegedus. Handbook of photovoltaic science and engineering. **John Wiley & Sons**, 2011.

[32] FLOWER, Maggie A., ed. Webb's physics of medical imaging. **CRC press**, 2012.

[33] ENDERLE, John; BRONZINO, Joseph eds. Introduction to biomedical engineering. **Academic press**, 2012.

[34] BHATTACHARYA, Pallab. Semiconductor optoelectronic devices. **Prentice-Hall, Inc.**, 1997.

[35] LAUD, B. B. Lasers and Non-Linear Optics. **New age International (p) Limited Publishers**, 2004.

[36] Application of Spectroscopic Methods to Environmental Problems. **Taylor & Francis**, 2024. Disponível em: <https://www.tandfonline.com/doi/full/10.1081/SL-200062302>. Acesso em: 30 dez. 2024.

[37] KELLY, Stephen M. Flat panel displays: advanced organic materials. **Royal Society of Chemistry**, 2007.

[38] AMIJI, Mansoor M., ed. Nanotechnology for cancer therapy. **CRC press**, 2006.

[39] BOHREN, Craig F.; HUFFMAN, Donald R. Absorption and scattering of light by small particles**. John Wiley & Sons**, 2008.

[40] XV. On the light from the sky, its polarization and colour. **The London, Edinburgh, and Dublin Philosophical Magazine and Journal of Science**, 2025. Disponível em: <https://www.tandfonline.com/doi/abs/10.1080/14786447108640452>. Acesso em: 4 jan. 2025.

[41] WEHR, A.; LOHR, U. Airborne laser scanning—an introduction and overview. **ISPRS Journal of Photogrammetry and Remote Sensing**, 1 jul. 1999. v. 54, n. 2-3, p. 68–82.

[42] SHAN, J.; TOTH, C. K. Topographic laser ranging and scanning: principles and processing. **CRC press**, 2018.

[43] PALMIERI, L. *et al.* Rayleigh-Based Distributed Optical Fiber Sensing. **Sensors**, 8 set. 2022. v. 22, n. 18, p. 6811–6811.

[44] ÖRSEL, O. E.; NOH, J.; BAHL, G. Electrically-controlled suppression of Rayleigh backscattering in an integrated photonic circuit. **Nanophotonics**, 2 jan. 2024. v. 13, n. 2, p. 173–181.

[45] SVELA, A. Ø. *et al.* Coherent suppression of backscattering in optical microresonators. **Light Science & Applications**, 23 dez. 2020. v. 9, n. 1.

[46] TO, C. German physicist (1868-1957). **Wikipedia.org**, 24 ago. 2004. Disponível em: <https://en.wikipedia.org/wiki/Gustav_Mie#cite_ref-1>. Acesso em: 5 jan. 2025.

[47] BALDERAS-CABRERA, C.; CASTILLO, R. Mie scattering theory applied to light scattering of large nonhomogeneous colloidal spheres. **The Journal of Chemical Physics**, 22 ago. 2024. v. 161, n. 8.

[48] YANG, D. *et al.* Mie Scattering Nanointerferometry for the Reconstruction of Tightly Focused Vector Fields by Polarization Decomposition. **Photonics**, 26 abr. 2023. v. 10, n. 5, p. 496–496.

[49] DORODNYY, A.; SMAJIC, J.; LEUTHOLD, J. Mie Scattering for Photonic Devices. **Laser & Photonics Review**, 21 jul. 2023. v. 17, n. 9.

[50] HULST, H. C. van de. Light Scattering by Small Particles. **Dover Publications**, 1981.

[51] TYNDALL, J. IV. On the blue colour of the sky, the polarization of skylight, and on the polarization of light by cloudy matter generally. **Proceedings of the Royal Society of London**, 31 dez. 1869. v. 17, p. 223–233.

[52] KERKER, M. The scattering of light and other electromagnetic radiation: physical chemistry: a series of monographs. Vol. 16. **Academic press**, 2013.

[53] BOYD, R. W. Nonlinear Optics. **Academic Press**. 2020.

[54] SHEN, Y. R. The Principles of Nonlinear Optics. **Wiley-Interscience**. 2003.

[55] BIERLEIN, J. D.; VANHERZEELE, H. Potassium titanyl phosphate: properties and new applications. **Journal of the Optical Society of America B**, 1 abr. 1989. v. 6, n. 4, p. 622–622.

[56] VOLK, M. Optical ridge waveguides in lithium niobate and potassium titanyl phosphate. **Hsu-hh.de**, 2019.

[57] ZERNIKE, F.; MIDWINTER, J. E. Applied nonlinear optics. **Courier Corporation**, 2006.

[58] MYERS, L. E. *et al.* Quasi-phase-matched optical parametric oscillators in bulk periodically poled LiNbO_3. **Journal of the Optical Society of America B**, 1 nov. 1995. v. 12, n. 11, p. 2102–2102.

[59] FEJER, M. M. *et al.* Quasi-phase-matched second harmonic generation: tuning and tolerances. **IEEE Journal of Quantum Electronics**, 1992. v. 28, n. 11, p. 2631–2654.

[60] YARIV A.; YEH, P. Photonics: Optical Electronics in Modern Communications. **Oxford University Press**. 2006.

[61] SALEH, B. E. A.; TEICH, M. C. Fundamentals of Photonics. **Wiley**. 2007.

[62] CAMPAGNOLA, P. J.; LOEW, L. M. Second-harmonic imaging microscopy for visualizing biomolecular arrays in cells, tissues and organisms. **Nature Biotechnology**, 31 out. 2003. v. 21, n. 11, p. 1356–1360.

[63] AGRAWAL, G. P. Nonlinear Fiber Optics. **Academic Press**. 2019.

[64] KWIAT, P. G. *et al.* New High-Intensity Source of Polarization-Entangled Photon Pairs. **Physical Review Letters**, 11 dez. 1995. v. 75, n. 24, p. 4337–4341.

[65] SHEN, Y. R. Surface nonlinear optics: a historical perspective. **IEEE Journal of Selected Topics in Quantum Electronics**, nov. 2000. v. 6, n. 6, p. 1375–1379.

[66] SHEN, Y. R. Surface properties probed by second-harmonic and sum-frequency generation. **Nature**, fev. 1989. v. 337, n. 6207, p. 519–525.

[67] Quantitative spectral and orientational analysis in surface sum frequency generation vibrational spectroscopy (SFG-VS). **International Reviews in Physical Chemistry**, 2025.

[68] CHEN, Z.; SHEN, Y. R.; SOMORJAI, G. A. STUDIES OF POLYMER SURFACES BY SUM FREQUENCY GENERATION VIBRATIONAL SPECTROSCOPY. **Annual Review of Physical Chemistry**, 28 jul. 2002. v. 53, n. 1, p. 437–465.

[69] EBRAHIM-ZADEH, M.; SOROKINA, I. T. Mid-Infrared Coherent Sources and Applications. **Springer**. (Chapter on SFG applications). 2003.

[70] NEW, G. H. C. *Introduction to Nonlinear Optics*. **Cambridge University Press**. 2011.

[71] MARBURGER, J. H. Self-focusing: Theory. **Progress in Quantum Electronics**, 1 abr. 1975. v. 4, p. 35–110.

[72] ZIPFEL, W. R.; WILLIAMS, R. M.; WEBB, W. W. Nonlinear magic: multiphoton microscopy in the biosciences. **Nature Biotechnology**, 31 out. 2003. v. 21, n. 11, p. 1369–1377.

[73] A COUAIRON; A MYSYROWICZ. Femtosecond filamentation in transparent media. **Physics Reports**, 7 fev. 2007. v. 441, n. 2-4, p. 47–189.

[74] RANKA, J. K.; WINDELER, R. S.; STENTZ, A. J. Visible continuum generation in air–silica microstructure optical fibers with anomalous dispersion at 800 nm. **Optics Letters**, 1 jan. 2000. v. 25, n. 1, p. 25–25.

[75] TREACY, E. Optical pulse compression with diffraction gratings. **IEEE Journal of Quantum Electronics**, set. 1969. v. 5, n. 9, p. 454–458.

[76] ZHU, G. *et al.* Simultaneous spatial and temporal focusing of femtosecond pulses. **Optics Express**, 1 jan. 2005. v. 13, n. 6, p. 2153–2153.

[77] ZHAN, L.; TONG, Z.; GUO, H. Observation of spatial self-phase modulation in photorefractive crystals. **Optics Letters**, 2002. 27(8), 598–600.

[78] WU, L. *et al.* Recent Advances of Spatial Self-Phase Modulation in 2D Materials and Passive Photonic Device Applications. **Small**, 30 jul. 2020. v. 16, n. 35.

[79] ZHAN, L.; TONG, Z.; GUO, H. Observation of spatial self-phase modulation in photorefractive crystals. **Optics Letters**, 2018, 27(8), 598–600.

[80] KIVSHAR, Y. S.; AGRAWAL, G. P. Optical Solitons: From Fibers to Photonic Crystals. 2003.

[81] HEINZ, T. F. Nonlinear Optics of Thin Films and Surfaces in Nonlinear Surface Electromagnetic Phenomena. 1991.

[82] BARAD, Y. *et al.* Nonlinear scanning laser microscopy by third harmonic generation. **Applied Physics Letters**, 24 fev. 1997. v. 70, n. 8, p. 922–924.

[83] POWERS, P. E.; JOSEPH, W. H. Fundamentals of nonlinear optics. **CRC press**, 2017.

[84] BUTCHER, P. N.; COTTER, D. The Elements of Nonlinear Optics. **Cambridge, UK: Cambridge University Press**, 1990.

[85] M. SHEIK-BAHAE *et al.* Sensitive measurement of optical nonlinearities using a single beam. **IEEE Journal of Quantum Electronics**, 1 abr. 1990. v. 26, n. 4, p. 760–769.

[86] DENK, W.; STRICKLER, J. H.; WEBB, W. W. Two-Photon Laser Scanning Fluorescence Microscopy. **Science**, 6 abr. 1990. v. 248, n. 4951, p. 73–76.

[87] AGRAWAL, G. P. Nonlinear absorption and ultrafast carrier dynamics in semiconductors. ***J. Opt. Soc. Am. B***, 1985. vol. 2, no. 3, pp. 480-488.

[88] MAKAROV, N. S.; MIKHAIL DROBIZHEV; ALEKSANDER REBANE. Two-photon absorption standards in the 550-1600 nm excitation wavelength range. **Optics Express**, 11 mar. 2008. v. 16, n. 6, p. 4029–4029.

[89] ALESSIA PASQUAZI *et al.* Micro-combs: A novel generation of optical sources. **Physics Reports**, 12 out. 2017. v. 729, p. 1–81.

[90] CORKUM, P. B.; KRAUSZ, F. Attosecond science. **Nature Physics**, 1 jun. 2007. v. 3, n. 6, p. 381–387.

[91] L'HUILLIER, A.; PHILIPPE BALCOU. High-order harmonic generation in rare gases with a 1-ps 1053-nm laser. **Physical Review Letters**, 8 fev. 1993. v. 70, n. 6, p. 774–777.

[92] BLOEMBERGEN, N. Nonlinear Optics. **World Scientific**, 1996.

[93] D. EIMERL *et al.* Optical, mechanical, and thermal properties of barium borate. **Journal of Applied Physics**, 1 set. 1987. v. 62, n. 5, p. 1968–1983.

[94] CERULLO, G.; DE SILVESTRI, S. Ultrafast optical parametric amplifiers. **Review of Scientific Instruments**, 1 jan. 2003. v. 74, n. 1, p. 1–18.

[95] YARIV, A.; YEH, P. Photonics: Optical Electronics in Modern Communications, 6th ed. **Oxford University Press**, 2007.

[96] FEJER, M. M. *et al.* Quasi-phase-matched second harmonic generation: tuning and tolerances. **IEEE Journal of Quantum Electronics**, 1992. v. 28, n. 11, p. 2631–2654.

[97] MAK, K. F.; SHAN, J. Photonics and optoelectronics of 2D semiconductor transition metal dichalcogenides. **Nature Photonics**, 31 mar. 2016. v. 10, n. 4, p. 216–226.

[98] NISHIZAWA, H. Theory of fifth-harmonic generation in cubic centrosymmetric crystals. **Journal of the Optical Society of America B**, 1 jul. 2020. v. 37, n. 9, p. 2538–2538.

[99] KRAUSZ, F.; IVANOV, M. Attosecond physics. **Reviews of Modern Physics**, 2 fev. 2009. v. 81, n. 1, p. 163–234.

[100] TENIO POPMINTCHEV *et al.* Bright Coherent Ultrahigh Harmonics in the keV X-ray Regime from Mid-Infrared Femtosecond Lasers. **Science**, 7 jun. 2012. v. 336, n. 6086, p. 1287–1291.

[101] VAMPA, G. *et al.* Linking high harmonics from gases and solids. **Nature**, 24 jun. 2015. v. 522, n. 7557, p. 462–464.

[102] ZYSS, J.; LEDOUX, I. Nonlinear optics in multipolar media: theory and experiments. **Chemical Reviews**, jan. 1994. v. 94, n. 1, p. 77–105. Acesso em: 17 mar. 2021.

[103] CLAYS, K.; ANDRÉ PERSOONS. Hyper-Rayleigh scattering in solution. **Physical Review Letters**, 10 jun. 1991. v. 66, n. 23, p. 2980–2983.

[104] SIONCKE, S.; VERBIEST, T.; PERSOONS, A. Second-order nonlinear optical properties of chiral materials. **Materials Science and Engineering: R: Reports**, nov. 2003. v. 42, n. 5-6, p. 115–155.

[105] NIKOLAOS GOMOPOULOS *et al.* Label-free second harmonic and hyper Rayleigh scattering with high efficiency. **Optics Express**, 8 jan. 2013. v. 21, n. 1, p. 815–815.

[106] CÉCILE JOULAUD *et al.* Characterization of the nonlinear optical properties of nanocrystals by Hyper Rayleigh Scattering. **Journal of Nanobiotechnology**, 1 dez. 2013. v. 11, n. S1.

[107] SIONCKE, S.; THIERRY VERBIEST; ANDRÉ PERSOONS. Second-order nonlinear optical properties of chiral materials. **Materials Science and Engineering R Reports**, 27 out. 2003. v. 42, n. 5-6, p. 115–155.

[108] PRASAD, P.; WILLIAMS, D. Introduction to Nonlinear Optical Effects in Molecules and Polymers. **Wiley-Interscience**. 1991.

[109] CAMPO, J. *et al.* Highly sensitive setup for tunable wavelength hyper-Rayleigh scattering with parallel detection and calibration data for various solvents. **Optics Express**, 6 mar. 2009. v. 17, n. 6, p. 4587–4587.

[110] LUKAS OHNOUTEK *et al.* Single Nanoparticle Chiroptics in a Liquid: Optical Activity in Hyper-Rayleigh Scattering from Au Helicoids. **Nano Letters**, 24 jun. 2020. v. 20, n. 8, p. 5792–5798.

APPENDIX B: THERMAL EFFECTS IN Z-SCAN EXPERIMENTS

In Z-scan experiments, thermal effects arise when the absorption of laser light by a material leads to localized heating, causing variations in the refractive index – a phenomenon known as **thermal lensing** [1]. This effect can significantly influence the accuracy of measurements, particularly when distinguishing between electronic and thermal contributions to the nonlinear optical response. Materials with inherent linear absorption can convert incident laser energy into heat, leading to temperature gradients and refractive index changes. Laser sources with high repetition rate can cause cumulative heating, as the material may not have sufficient time to dissipate heat between pulses, enhancing thermal lensing effects [2].

To address thermal lensing effects, several strategies can be employed. One effective method is to reduce the laser repetition rate, which allows more time for heat dissipation between pulses and helps minimize cumulative thermal effects [3]. Additionally, using pulse pickers or mechanical choppers can be beneficial; these devices reduce the effective repetition rate and selectively transmit pulses, thereby decreasing the average power and associated heating [4]. Another viable approach is to utilize shorter pulse durations by implementing femtosecond laser pulses. This technique limits heat diffusion during the pulse duration, resulting in reduced thermal effects compared to longer pulses [5, 6].

Additionally, the use of time-resolved techniques, such as **time-resolved Z-scan** methods, can help distinguish between fast electronic responses and slower thermal effects by analyzing the temporal dynamics of the nonlinear response [7]. For example, studies have utilized femtosecond time-resolved Z-scan methods to investigate NLA and NLR in various materials, enabling the separation of electronic and thermal contributions to the nonlinear response [8]. The time-resolved Z-scan technique is an advanced modification of the standard Z-scan method, designed to investigate the temporal dynamics of nonlinear optical properties in materials. By incorporating a temporal dimension, this technique enables the differentiation between ultrafast electronic responses and slower processes such as thermal effects or molecular reorientations [9].

Typically in a time-resolved Z-scan method, a pump-probe setup is employed, where an ultrafast pump pulse excites the sample, and a time-delayed probe pulse measures the induced changes in transmittance as the sample is translated along the beam's propagation axis (z-axis) [10] – see for instance Figure B.1 By systematically varying the delay between the pump and probe pulses, one can construct a temporal profile of the material's nonlinear

response, providing insights into both the magnitude and relaxation dynamics of the observed nonlinearities [11]. This method has been crucial for investigating, nonlinear time-dependent effects, such as carrier relaxation in semiconductors and the dynamics of nonlinear refraction in various materials [11]. It enables a more accurate characterization of ultrafast optical phenomena.

Figure B.1 – Example of a two-color time-resolved Z-scan setup.

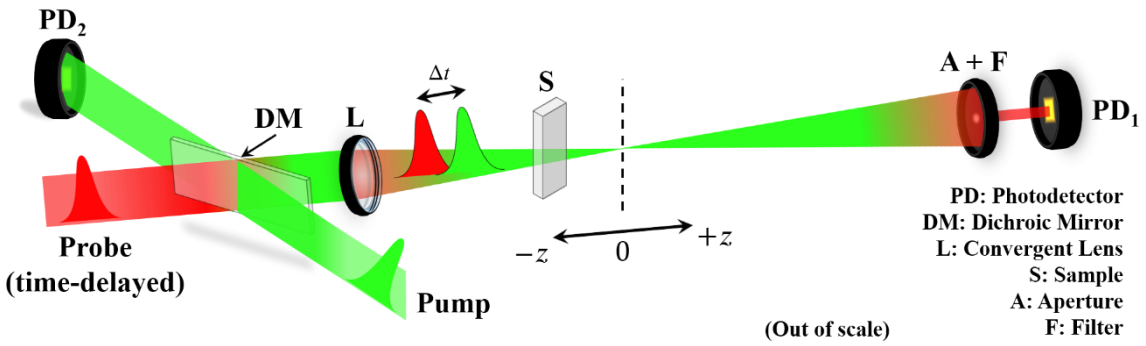

Source: The author (2025).

Figure B.1 illustrates a two-color time-resolved Z-scan method usually used to infer nondegenerate nonlinearities in diverse materials [12]. One can choose a strong pump beam to generate the nonlinearity resonant with the linear absorption of the material, while probing with a weak laser beam in a non-resonant material's absorption window. The NLR process can be achieve via a cross-phase modulation process (XPM) and measured through a CA Z-scan configuration [13]. In this scenario, thermal load arises from one-photon absorption of the pump beam, leading to heat accumulation, as we consider the material does not thermalize between successive pulses. Of course, other parameters, such as temporal pulse width and high-repetition-rate lasers, also influence this analysis. This heat loading makes thermal effects time-dependent. Figure B.2 illustrates the time evolution of the transmittance pattern using a time-resolved Z-scan approach, demonstrating a material that exhibits a thermal load effect. Figure B.2 exhibits CA transmittance patterns for different time-delays (Δt).

When, $\Delta t = 0$, no thermal load is present and the transmittance goes to zero (as shown by red curve in Figure B.2). As Δt increases, thermal accumulation begins, causing the variation of the peak-valley transmittances to rise until they reach a maximum value at $\Delta t = 5.0$ (illustrated by the purple continuous curve in Figure B.2). The material represented in this figure demonstrates a self-defocusing refractive nonlinearity, which is characteristic of the thermal-lensing effect. For comparison purposes, the purple dashed curve in Figure B.2, shows the instantaneous pure electronic response of a material for all Δt values clarifying that electronic

responses are not time-dependent and the peak-valley pattern are the same for all times. It is worthy to mention that in some materials, such as certain organic molecules or liquids, the bound electronic Kerr effect can be negative ($\Delta n < 0$) [14]. This leads to self-defocusing behavior, as illustrated in Figure B.2. The insert in Figure B.2, shows the OA Z-scan pattern for a pure electronic 2PA material, and in this case, the OA signal should remain constant across time delays.

Figure B.2 – CA transmittance curves for different time-delays (Δt) for a two-color time-resolved Z-scan. The continuous lines represent the medium nonlinear thermal responses, while the dashed lines are the instantaneous electronic responses. Insert: OA transmittance curves. The time-delays are in arbitrary units.

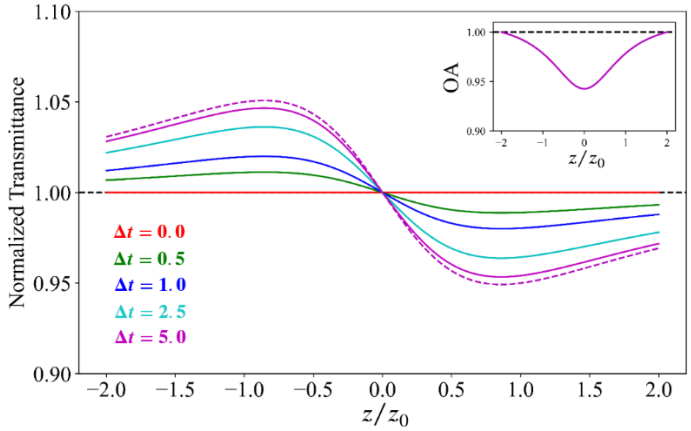

Source: The author (2025).

In summary, thermal effects in Z-scan measurements can significantly alter the interpretation of NLO properties, particularly in high-repetition-rate experiments or materials with slow thermal diffusion. These effects manifest as asymmetric CA traces, delayed nonlinear absorption, and long-lived refractive index changes. To mitigate thermal accumulation, several strategies can be employed, including reducing the laser repetition rate, using short pulse durations, implementing choppers or gated detection systems, and selecting materials with high thermal diffusivity. Alternatively, the time-resolved Z-scan separates instantaneous Kerr, free-carrier, and thermal contributions (see references [12] and [13] for more details).

References

[1] FALCONIERI, M. Thermo-optical effects in Z -scan measurements using high-repetition-rate lasers. **Journal of Optics A Pure and Applied Optics**, 24 set. 1999. v. 1, n. 6, p. 662–667.

[2] ANDRUS, L.; BEN-YAKAR, A. Thermal lensing effects and nonlinear refractive indices of fluoride crystals induced by high-power ultrafast lasers. **Applied Optics**, 2 set. 2020. v. 59, n. 28, p. 8806–8806.

[3] BURKINS, P. *et al.* Thermally managed Z-scan methods investigation of the size-dependent nonlinearity of graphene oxide in various solvents. **Journal of the Optical Society of America B**, 28 out. 2016. v. 33, n. 11, p. 2395.

[4] STUART, B. C. *et al.* Nanosecond-to-femtosecond laser-induced breakdown in dielectrics. **Physical review**, 15 jan. 1996. v. 53, n. 4, p. 1749–1761.

[5] LIU, X.; DU, D.; MOUROU, G. Laser ablation and micromachining with ultrashort laser pulses. **IEEE Journal of Quantum Electronics**, 1997. v. 33, n. 10, p. 1706–1716.

[7] CASSAGNE, C.; BA, O.; BOUDEBS, G. Time-Resolved CW Thermal Z-scan for Nanoparticles Scattering Evaluation in Liquid Suspension. **Materials**, 19 jul. 2022. v. 15, n. 14, p. 5008.

[8] TSENG, K. Y.; WONG, K. S.; WONG, L. Femtosecond time-resolved Z-scan investigations of optical nonlinearities in ZnSe. **Optics Letters**, 1 fev. 1996. v. 21, n. 3, p. 180–180.

[9] M. SHEIK-BAHAE; SAID, A. A.; STRYLAND, V. High-sensitivity, single-beam n_2 measurements. **Optics Letters**, 1 set. 1989. v. 14, n. 17, p. 955–955.

[10] R. L. SUTHERLAND. *Handbook of Nonlinear Optics*. **New York: CRC Press**, 2nd ed. 2003.

[11] WANG, J. *et al.* Time-resolved Z-scan measurements of optical nonlinearities. **Journal of the Optical Society of America B**, 1 jun. 1994. v. 11, n. 6, p. 1009–1009.

[12] SHEIK-BAHAE, M. *et al*. Measurement of nondegenerate nonlinearities using a two-color Z scan. **Optics Letters**, 15 fev. 1992. v. 17, n. 4, p. 258.

[13] MA, H.; GOMES, A. S. L.; ARAUJO, C. B. DE. Measurements of nondegenerate optical nonlinearity using a two-color single beam method. **Applied Physics Letters**, 18 nov. 1991. v. 59, n. 21, p. 2666–2668.

[14] CHEMLA, D. S. Nonlinear optical properties of organic molecules and crystals V1. Vol. 1. **Elsevier**. 2012.

APPENDIX C: ALTERNATIVE Z-SCAN METHODS

The standard Z-scan technique has become a fundamental tool for measuring the NLO properties of materials, particularly the third-order nonlinear refractive index (n_2) and nonlinear absorption coefficient (α_2). However, while the conventional Z-scan is highly sensitive and widely applicable, certain experimental conditions – such as strong nonlinear absorption, ultrafast optical responses, anisotropic nonlinearities, and high-repetition-rate laser sources – demand modifications to the original method. To address these challenges, various alternative Z-scan techniques have been developed over the years to enhance sensitivity, improve accuracy, and facilitate new types of nonlinear measurements. This subsection aims to introduce the different variations of the Z-scan technique, outlining when each method is most suitable.

One significant extension of the Z-scan technique is the **eclipse Z-scan**, which introduces an additional spatial filter to enhance the detection of small nonlinear phase shifts, increasing sensitivity for weak nonlinearities [1]. Instead of using a small aperture in the detection plane, this technique employs an **opaque disk** to partially block the transmitted beam, increasing the detection sensitivity to small phase distortions [2]. This approach is particularly effective for materials with low nonlinear refractive indices, where the conventional CA Z-scan may not provide sufficient contrast [3]. The eclipse Z-scan technique can increase the sensitivity by a factor of 10 to 100 times compared to the conventional Z-scan method, depending on the experimental conditions and the material being studied [4]. Studies have demonstrated that the eclipse Z-scan can significantly improve the measurement of nonlinear refraction in materials such as CS_2 and ZnSe, offering better signal-to-noise ratios and enhanced accuracy for weak nonlinearities [5].

The **two-color Z-scan** method extends the standard Z-scan by using separate pump and probe beams at different wavelengths, as shown previously in Figure B.1 This two-color configuration allows for the measurement of **nondegenerate nonlinearities**, such as cross-phase modulation (XPM) and nondegenerate two-photon absorption [3]. This technique is particularly valuable for characterizing materials in optical communication and ultrafast photonic applications. By introducing a controlled time delay between pump and probe pulses, a two-color **time-resolved Z-scan** can be established, as discussed in APPENDIX B. Time-resolved Z-scan techniques provides insight into the temporal evolution of nonlinear responses, allowing for the differentiation between instantaneous electronic nonlinearities from slow free-

carrier and thermal effects [6]. This capability is crucial for ultrafast optics and the nonlinear characterization of semiconductors.

For experiments using high-repetition-rate lasers, **thermal-managed Z-scan** techniques have been introduced to minimize cumulative heating effects that can distort nonlinear measurements. These approaches involve modulated excitation schemes, sample cooling systems, or alternative normalization procedures to account for residual heat buildup [3]. One clever alternative to deal with the thermal load effect is the **thermally managed eclipse Z-scan** technique, an advanced variation of the conventional Z-scan method, designed to improve sensitivity and enable the differentiation between thermal and non-thermal nonlinearities in optical materials. Figure C.1 shows a typical thermally managed eclipse Z-scan setup.

Figure C.1 – Thermally managed eclipse Z-scan setup. The transmittance signals measured by PD_1 are trigged with the chopper frequency and send to a digital oscilloscope for processing. PD_2 is a reference photodetector to correct pulse-to-pulse fluctuations. One can measure the OA Z-scan signal by removing the disk or add a new detection arm by adding a beam splitter before the disk.

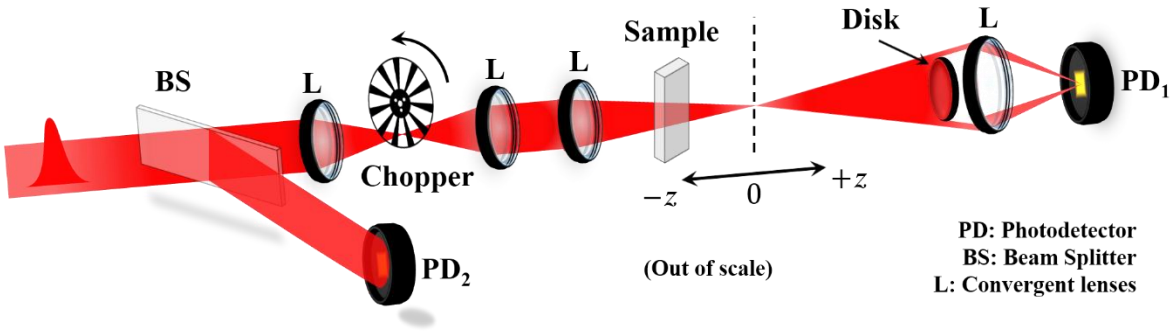

Source: The author (2025).

The thermally managed eclipse Z-scan method introduces two key modifications. First, instead of using a small aperture to detect beam distortions, it employs an eclipse configuration to enhance sensitivity. This improved sensitivity allows for the detection of weaker NLO effects, such as those in biomolecules or low-nonlinearity materials [7]. Second, the technique incorporates a thermal management strategy using a chopper, which modulates the incident laser beam and enables time-resolved measurements of the nonlinear signal at different positions relative to the focus [6, 7]. By analyzing the time evolution of the Z-scan signal, this approach differentiates between fast electronic nonlinearities and slower thermal nonlinearities, which accumulate over time [6 – 8]. In contrast, conventional Z-scan methods typically do not provide this temporal discrimination, making it difficult to separate electronic and thermal

contributions, especially when using high-repetition-rate laser sources. Figure C.2 illustrates the theoretical transmittance curves expected for CA thermally managed eclipse Z-scan experiment.

Figure C.2 – Theoretical CA Z-scan curves for a thermally managed eclipse Z-scan. The thermal evolution times are expressed as time factors (τ), which indicate various stages in the development of thermal nonlinearity. The time variable is normalized by the chopper period. Insert: Chopper voltage signal. The normalized chopper voltage signal features a 50% duty cycle and a rising time of 5% relative to the chopper period.

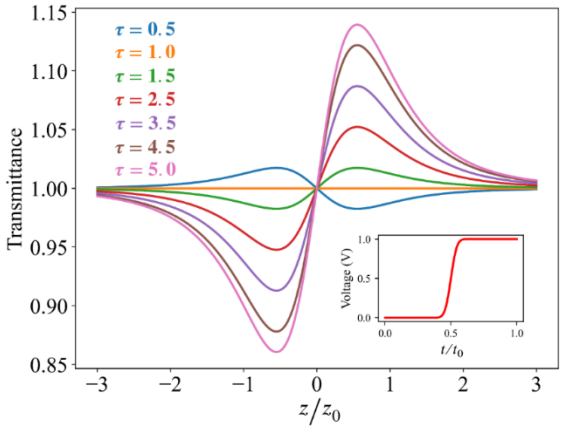

Source: The author (2025).

The blue curve in Figure C.2 exemplifies a fast electronic nonlinearity that occurs within a duration 10 times longer than the chopper's rising time. After this initial period, the phase shift caused by the thermal lensing effect becomes predominant. It is important to note that, in this Z-scan setup, the transmittance curves display peak-valley or valley-peak patterns contrary to the standard Z-scan method. For instance, the self-focusing electronic nonlinearity response appears as a "self-defocusing" effect in the transmittance pattern. Additionally, the electronic and thermal refractive nonlinearities exhibit opposite signals. For example, at $\tau = 1.0$ the total nonlinear phase reaches zero, resulting in the cancellation of the transmittance changes.

The **polarization-resolved Z-scan** (PRZS) technique is an advanced version of the conventional Z-scan method, designed to distinguish and quantify different types of nonlinear optical effects, such as electronic, orientational, and thermal nonlinearities, by exploiting their distinct responses to laser polarization [9, 10]. In the PRZS setup, a quarter-wave plate is added to control the polarization state of the laser beam, allowing measurements to be taken with both linear and circular polarizations [10]. The key difference lies in the fact that the PRZS technique explores the tensor nature of the third-order nonlinear susceptibility, where different nonlinear effects exhibit unique polarization dependencies. For instance, the ratio of the Z-scan signal (ΔT_{p-v}) between linear and circular polarizations varies for electronic (1.5), orientational (4),

and thermal (1) nonlinearities [9, 10]. This enables the discrimination and quantification of mixed nonlinear effects, which is not possible with the conventional Z-scan method that typically uses only linear polarization. Additionally, the PRZS technique can be combined with varying laser repetition rates to further isolate and measure cumulative thermal effects, providing a more comprehensive characterization of nonlinear optical materials [10, 11].

The PRZS setup is similar to the conventional Z-scan configuration but incorporates additional elements to control and analyze the polarization state of the laser beam. As described in [10], the setup includes a broadband quarter-wave plate ($\lambda/4$) placed before the sample to switch between linear and circular polarization states. The sample is scanned along the beam propagation direction (z-axis) through the focal region, and the normalized transmittance is measured using a photodetector with an adjustable aperture. The use of a mechanical chopper and a lock-in amplifier ensures low-noise measurements, independent of the laser repetition rate [10]. This setup allows for precise control over the polarization state and enables the detection of subtle differences in the nonlinear response of the material under study. Figure C.3 illustrates a typical PRZS apparatus.

Figure C.3 – Typical polarization-resolved Z-scan setup. The transmittance signal measured by PD is triggered with chopper frequency using a lock-in amplifier (not shown in the figure) and connected to a computer for signal processing.

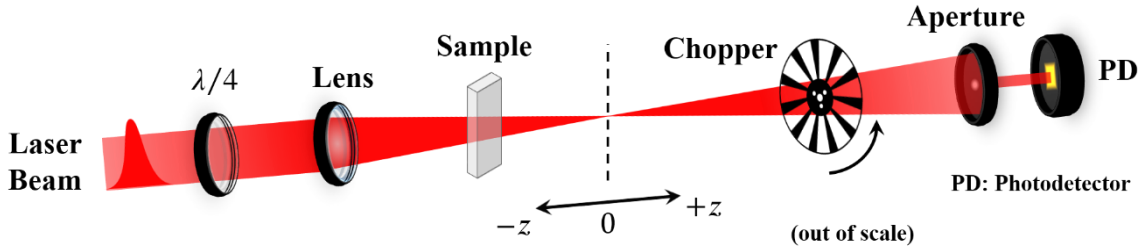

Source: The author (2025).

Another intriguing variation of the Z-scan technique is the photoacoustic Z-scan (PAZ-scan). This method adapts the conventional Z-scan approach to measure nonlinear optical properties by detecting photoacoustic signals instead of transmitted or reflected light intensity. In this technique, a modulated laser beam is focused onto a sample, which moves along the optical axis (z-direction), causing localized absorption and subsequent thermal expansion that generates acoustic waves [12]. A microphone or piezoelectric detector captures these signals, providing information about the sample's nonlinear absorption and thermal properties [12, 13]. Unlike conventional Z-scan, which relies on changes in light transmission through the sample to determine nonlinear absorption and refraction, the PAZ-scan is highly sensitive to non-

radiative relaxation processes and can be used in optically scattering or highly absorbing media where traditional methods struggle [12, 13]. This makes it particularly useful for biological samples and materials with strong optical absorption.

For instance, Maldonado et al. (2020) characterized the nonlinear optical and relaxation properties of layered transition metal dichalcogenides (LTMDs) using conventional Z-scan and PAZ-scan techniques. This study provides a comprehensive overview of the experimental setup for the PAZ-scan, as well as the theoretical methods used to extract information from the experimental data obtained through PAZ-scan [14].

Among the alternative techniques to the conventional Z-scan method previously discussed, the Hartmann-Shack (HS) wavefront sensing approach stands out as a powerful and versatile tool for characterizing third-order nonlinear optical (NLO) properties, particularly the nonlinear refractive index n_2. Unlike the standard Z-scan – which relies on monitoring far-field transmittance changes as a sample moves through the focal region of a laser beam – the HS technique directly measures wavefront distortions induced by nonlinear phase shifts in the material when exposed to intense light.

The HS sensor comprises a microlens array that decomposes the incoming wavefront into localized tilts, which are then reconstructed using Zernike polynomials. Among these, the defocus Zernike coefficient (typically labeled C_5 or Z_2^0) is most sensitive to changes in beam curvature resulting from nonlinear refraction. Two main configurations of the HS method have been reported: the collimated beam configuration, where a uniform beam probes the sample at varying intensities, and the HS Z-scan, which mimics the traditional Z-scan geometry but replaces the far-field aperture and detector with the HS sensor. One key advantage of the HS approach is its insensitivity to intensity fluctuations, sample misalignments, and imperfections – common issues that can degrade the accuracy of conventional Z-Scan measurements [15]. Moreover, the HS technique allows for simultaneous measurement of wavefront distortion and beam transmittance without moving parts in some configurations, which simplifies the experimental setup. In addition, because the HS method analyzes the entire beam profile, it can potentially detect subtle changes in wavefront curvature at lower intensities than the threshold required for conventional Z-Scan detection, particularly in cases where transmittance variations are below the detection limit due to laser noise.

Experimental validation of the technique has shown that the defocus Zernike coefficient linearly correlates with the laser intensity, allowing the extraction of n_2 values for materials

such as CS_2 and quartz. Notably, the HS method was sensitive enough to detect both the magnitude and the sign of n_2, including thermal nonlinearities induced at high repetition rates [16]. For example, in carbon disulfide, the HS method successfully distinguished electronic (positive n_2) and thermal (negative n_2) contributions depending on the laser repetition rate. Additionally, the HS technique has been applied to more complex nanomaterials. In particular, it was used to measure the effective nonlinear refractive index of electric-field-aligned gold nanorods suspended in an index-matching oil. This study demonstrated that the nonlinear response could be modulated by as much as 60% through controlled alignment, with the nonlinear refractive index linearly dependent on the orientational order parameter S [16]. This underscores the technique's utility not only in static characterization but also in dynamic and reconfigurable NLO systems.

Thus, the HS wavefront sensing technique offers several distinct advantages such as higher robustness to noise and fluctuations, the ability to simultaneously analyze transmittance and phase, and suitability for dynamic systems. These features make it a promising tool for studying both fundamental NLO properties and practical applications in emerging photonic materials.

In conclusion, alternative Z-Scan techniques offer distinct advantages that broaden the method's applicability beyond its traditional limitations. This appendix aimed to discuss the principles, experimental implementations, and specific benefits of these alternative Z-scan techniques, providing the reader with a comprehensive understanding of the variety available in literature.

References

[1] XIA, T. *et al.* Eclipsing Z-scan measurement of $\lambda/10^4$ wave-front distortion. **Optics Letters**, 1 mar. 1994. v. 19, n. 5, p. 317.

[2] ANDRADE, A. A.; GONÇALVES, A. Z.; de ARAÚJO, C. B. Eclipse Z-scan technique for measuring optical nonlinearities. **Applied Physics Letters**, vol. 89, no. 16, p. 161909, 2006.

[3] ARAÚJO, C. B. de; GOMES, A. S. L. Z-scan techniques for nonlinear optical characterization: A review. **Brazilian Journal of Physics**, vol. 39, no. 2, pp. 369–379, 2009.

[4] C. B. de ARAÚJO *et al*. Comparison of Z-scan and eclipse Z-scan techniques for nonlinear optical characterization of materials. **Optical Materials**, vol. 30, no. 6, pp. 990–995, 2008.

[5] ANDRADE, A. A.; ARAÚJO, C. B. de; GOMES, A. S. L. Eclipse Z-scan measurements of nonlinear refraction in CS_2 and ZnSe. **Optics Communications**, vol. 282, no. 13, pp. 2651–2655, 2009.

[6] GNOLI, A.; LUCA RAZZARI; MARCOFABIO RIGHINI. Z-scan measurements using high repetition rate lasers: how to manage thermal effects. **Optics Express**, 1 jan. 2005. v. 13, n. 20, p. 7976–7976.

[7] GOMES, L. *et al.* Thermally managed eclipse Z-scan. **Optics Express**, 19 fev. 2007. v. 15, n. 4, p. 1712–1712.

[8] GOMES, L. *et al.* Third-order nonlinear optical properties of bismuth-borate glasses measured by conventional and thermally managed eclipse Z scan. **Journal of Applied Physics**, 1 fev. 2007. v. 101, n. 3.

[9] MELHADO, M. S. *et al.* Discrimination between two distinct nonlinear effects by polarization-resolved Z-scan measurements. **Optics Express**, 24 jan. 2020. v. 28, n. 3, p. 3352.

[10] MOYSÉS, R. M.; BARBANO, E. C.; MISOGUTI, L. Discrimination of thermal, molecular orientation, and pure electronic refractive nonlinearities using the

polarization-resolved Z-scan technique. **Journal of the Optical Society of America B**, 10 mar. 2023. v. 40, n. 4, p. C60.

[11] FALCONIERI, M. Thermo-optical effects in Z -scan measurements using high-repetition-rate lasers. **Journal of optics**, 24 set. 1999. v. 1, n. 6, p. 662–667.

[12] YELLESWARAPU, C. S.; SRI-RAJASEKHAR KOTHAPALLI. Nonlinear photoacoustics for measuring the nonlinear optical absorption coefficient. **Optics Express**, 14 abr. 2010. v. 18, n. 9, p. 9020–9020.

[13] YELLESWARAPU, C. S.; SRI-RAJASEKHAR KOTHAPALLI; RAO, N. Photoacoustic Z-scan for the measurement of third-order nonlinear absorption coefficient. **Proceedings of SPIE, the International Society for Optical Engineering/Proceedings of SPIE**, 2 fev. 2011. v. 7917, p. 79171I79171I.

[14] MALDONADO, M. E. *et al.* Nonlinear Optical Interactions and Relaxation in 2D Layered Transition Metal Dichalcogenides Probed by Optical and Photoacoustic Z-Scan Methods. **ACS Photonics**, 9 nov. 2020. v. 7, n. 12, p. 3440–3447.

[15] D. RATIVA *et al.* Hartmann-Shack wavefront sensing for nonlinear materials characterization. **Optics Express**, 17 nov. 2009. v. 17, n. 24, p. 22047–22047.

[16] MALDONADO, M. *et al.* Nonlinear refractive index of electric field aligned gold nanorods suspended in index matching oil measured with a Hartmann-Shack wavefront aberrometer. **Optics Express**, 25 jul. 2018. v. 26, n. 16, p. 20298.

APPENDIX I

THE JOURNAL OF PHYSICAL CHEMISTRY C
A JOURNAL OF THE AMERICAN CHEMICAL SOCIETY

pubs.acs.org/JPCC Article

Nonlinear Optical Properties of 2D CdSe Nanoplatelets in a Nonresonant Regime

Igor M. Gonçalves,[‖] Anusri Medda, Alyson J. A. Carvalho,[‖] Cecília L. A. V. Campos,[‖] Soubhik Ghosh, Anderson S. L. Gomes,[*] and Amitava Patra[*]

Cite This: *J. Phys. Chem. C* 2023, 127, 16679−16686 Read Online

ACCESS | Metrics & More | Article Recommendations

ABSTRACT: The nonlinear optical response of CdSe and CdSe/CdS core/shell nanoplatelets (NPLs) in toluene suspension was determined by using Z-scan and optical Kerr gate (OKG) techniques at 800 nm in the femtosecond regime. First, an analysis of the nonlinearities based on the Z-scan resulted in $n_2 = 1.4 \times 10^{-16}$ cm^2/W and $n_2 = 1.3 \times 10^{-16}$ cm^2/W for CdSe and CdSe/CdS core/shell NPLs, respectively. Fifth-order nonlinear absorption behavior was predominant, resulting in $\alpha_4 = 4.0 \times 10^{-2}$ cm/GW for CdSe NPLs and $\alpha_4 = 9.0 \times 10^{-3}$ cm/GW for CdSe/CdS core/shell NPLs for an optical intensity of 60.97 and 122 GW/cm^2, respectively. The nonlinear refractive index obtained from Z-scan is in good agreement with those obtained from the OKG, and the response time obtained from OKG showed a decay of less than 1 ps for all studied materials, about 5 times slower than the pulse duration. For optical intensities in the range between 30.45 and 182.8 GW/cm^2, NLA was not observed for toluene but was observed for CdSe and CdSe/CdS core/shell NPLs, revealing that the presence of the NPLs decreases the threshold of the absorptive nonlinearity. The results are discussed and explained based on the well-known materials' electronic structure.

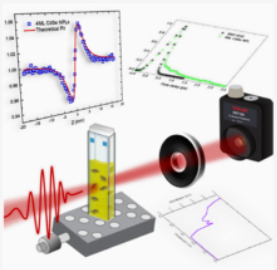

APPENDIX II

Applied Physics Letters ARTICLE pubs.aip.org/aip/apl

Saturable absorption and third-order nonlinear refraction of 2D CdSe nanoplatelets resonant with heavy-hole excitonic transitions

Cite as: Appl. Phys. Lett. **123**, 251108 (2023); doi: 10.1063/5.0178578
Submitted: 27 September 2023 · Accepted: 29 November 2023 ·
Published Online: 19 December 2023

View Online Export Citation CrossMark

Igor M. Gonçalves,[1] Anusri Medda,[2] Jessica E. Q. Bautista,[1] Cecília L. A. V. Campos,[1] Soubhik Ghosh,[2] Amitava Patra,[2,3] and Anderson S. L. Gomes[1,a)]

AFFILIATIONS

[1]Departamento de Física, Universidade Federal de Pernambuco, 50670-901 Recife-PE, Brazil
[2]School of Materials Sciences, Indian Association for the Cultivation of Science, Jadavpur, Kolkata 700032, India
[3]Institute of Nano Science and Technology, Knowledge City, Sector 81, Mohali 140306, India

[a)]Author to whom correspondence should be addressed: anderson.lgomes@ufpe.br

ABSTRACT

We report on the nonlinear optical response of CdSe nanoplatelets and CdSe/CdS core/shell nanoplatelets in the heavy-hole resonant excitonic transition spectral regions with femtosecond pulses. The nonlinear refraction and saturable absorption coefficients were obtained using the Z-scan technique, and the results were explained theoretically. The nonlinear optical response under nonresonant excitation has been previously examined; comparing with the results presented in this work, at least a one order of magnitude increase in the nonlinear refraction coefficient is evident.

APPENDIX III

photonics

MDPI

Article

Femtosecond Third-Order Nonlinear Electronic Responses of 2D Metallic $NbSe_2$

Cecília L. A. V. Campos [1,*], Igor Gonçalves [1], Jessica E. Q. Bautista [1], Alyson Carvalho [1], Ali M. Jawaid [2], Robert Busch [2], Richard Vaia [2] and Anderson S. L. Gomes [1,*]

[1] Departamento de Física, Universidade Federal de Pernambuco, Recife 50670-901, PE, Brazil; igor.mgoncalves@ufpe.br (I.G.); jessicaquib@gmail.com (J.E.Q.B.); alyson.carvalho@ufpe.br (A.C.)
[2] Materials and Manufacturing Directorate, Air Force Research Laboratories, Wright-Patterson AFB, Dayton, OH 45433, USA; ali.jawaid.ctr@us.af.mil (A.M.J.); robert.busch.6.ctr@us.af.mil (R.B.); richard.vaia@us.af.mil (R.V.)
* Correspondence: cecilia.campos@ufpe.br (C.L.A.V.C.); anderson.lgomes@ufpe.br (A.S.L.G.)

Abstract: This manuscript reports on the third-order nonlinear optical responses of two-dimensional metallic $NbSe_2$ suspended in acetonitrile (ACN). The standard Z-scan technique was employed with 190 fs optical pulses at 790 nm, a repetition rate of 750 Hz, and an intensity ranging from 30 to 300 GW/cm^2. A self-focusing nonlinear refractive index (NLR), $n_2 = +(1.8 \pm 0.1) \times 10^{-15}$ cm^2/W, and a nonlinear absorption (NLA) coefficient, $\alpha_2 = +(3.5 \pm 0.2) \times 10^{-2}$ cm/GW, were measured, with the NLA arising from a two-photon process. Aiming to further understand the material's electronic nonlinearities, we also employed the Optical Kerr Gate (OKG) to evaluate the material's time response and measure the NLR coefficient in an optical intensity range different from the one used in the Z-scan. For optical pulses of 170 fs at 800 nm and a repetition rate of 76 MHz, the modulus of the NLR coefficient was measured to be $n_2 = (4.2 \pm 0.5) \times 10^{-14}$ cm^2/W for intensities up to 650 MW/cm^2, with the material's time response limited by the pulse duration. The ultrafast time response and electronic optical nonlinearities are explained based on the material's 2D structure.